

**COMPARISON OF CPFEM AND SPECTRAL SOLUTION METHODS IN PREDICTION OF
STRAINS NEAR GRAIN BOUNDARIES IN A UNIAXIALLY LOADED
OLIGOCRYSTALLINE TENSILE SPECIMEN**

By

Siddharth Sankar Rath

A THESIS

Submitted
to Michigan State University
in partial fulfillment of the requirements
for the degree of

Materials Science and Engineering – Master of Science

2016

ABSTRACT

COMPARISON OF CPFEM AND SPECTRAL SOLUTION METHODS IN PREDICTION OF STRAINS NEAR GRAIN BOUNDARIES IN A UNIAXIALLY LOADED OLIGOCRYSTALLINE TENSILE SPECIMEN

By

Siddharth Sankar Rath

In this work, we have built upon the work done by Lim et al^[1] to determine whether the discrepancy in experimentally observed grain boundary strains and those calculated by Crystal Plasticity Finite Element Method (CPFEM) is a result of inherent shortcomings of F.E.M. We also determine if a spectral solution method would prove helpful and relatively more accurate at predicting strains near these grain boundaries. In the work done by Lim et al, a highly resolved CPFEM simulation of an oligocrystalline uniaxially loaded tantalum tension sample captured most of the experimentally observed features but markedly underestimated the grain boundary strain concentrations when the results of the simulation were compared with experimental results. Simulations were performed for the same oligocrystalline uniaxially loaded tension sample using Düsseldorf Advanced Materials Simulation Kit (DAMASK) and used the built in finite element and spectral solvers to calculate strains and grain rotations near the grain boundaries. Varying resolutions comparable to those used by Lim et al, were used. Investigation has been done on whether the inability of using finer resolutions with FEM and an inherent stiffness in the FE solution method, was the reason or the discrepancies observed as compared to experimental data. The spectral solvers use a *polarisation* solution method which converges rapidly and allows us to use even finer resolutions without being too computationally expensive. It also has much lower stiffness as regards the solution strategy. The distribution of equivalent strain as a function of grain boundary distance was plotted. Comparisons and equivalencies with the results from finite element solutions were done and established to ascertain whether or not the observed discrepancies in the case of finite element simulation were inherent in the method itself.

ACKNOWLEDGMENTS

I express my gratitude to my adviser Dr. Philip Eisenlohr who guided, helped, and instructed me throughout my research journey. I would like to use this opportunity to thank Dr. Carl J Boehlert and Dr. Thomas R Bieler for their insight, help, corrections, and instructions.

I would also like to extend my thanks to my fellow researchers and colleagues David Smiadak, Tias Maiti, Aritra Chakraborty, Zhuowen Zhao, and Chen Zhang for their assistance. A heartfelt thanks also goes to my friends inside and outside the department who kept me motivated and helped me up when I was down.

Finally, I would like to thank my parents for believing in me and supporting me financially as well as emotionally throughout my time at Michigan State University.

PREFACE

The chapters in this thesis are so designed that the reader can get valuable background information before getting to the point of analyzing the results. It begins with a list of figures which is helpful for easy maneuvering of the thesis.

The *first chapter* is an introduction about the work that we have done, the motivation for the same and touches upon some assumptions.

The *second chapter* deals with polycrystals, crystal structure, grains, grain boundaries, orientations and ways to depict them, and grain misorientations.

The *third chapter* is all about dislocations and relationships between dislocation concentrations and strain in uniaxially loaded tension samples. Grain boundaries and grain boundary-dislocation interactions are also discussed.

Stresses and strains in single and polycrystals have been explained briefly in the *fourth chapter*. Resolved shear stress, and critical resolved shear stress in single and polycrystals are also discussed.

The *fifth chapter* is a brief description of the constitutive model for crystal plasticity that has been used for the simulations. These are based on continuum mechanical models of crystal plasticity. The focus is on the Phenomenological power law description.

The *sixth chapter* discusses the polarisation Spectral Solution method.

After the background information, the *seventh chapter* deals with the present research question of interest and how a previous work by Lim et al^[1] at Sandia National Laboratories, was instrumental in raising this question, what is the objective of the research work and the plan of action as well as procedure that was followed to answer the research question of interest.

The *eighth* and final chapter deals with the results that were obtained during the research, and the conclusions that can be safely drawn from them.

The thesis concludes by listing the research papers that we consulted and used in our research.

TABLE OF CONTENTS

LIST OF FIGURES	vii
CHAPTER 1 INTRODUCTION	1
CHAPTER 2 CRYSTALS.....	3
2.1 Perfect Single Crystal.....	3
2.1.1 Lattices and unit cells.....	4
2.1.2 Crystallographic directions and Planes	5
2.1.3 Crystal Orientation	8
2.1.3.1 Quaternions	9
2.1.3.2 Euler Angles.....	9
2.1.3.3 Rotation Matrices.....	10
2.2 Polycrystals	11
2.2.1 Misorientations and grain boundaries	11
2.2.2 Texture and its representation	14
2.2.2.1 Pole-Figures.....	15
2.2.2.2 Inverse Pole-Figures	17
2.2.2.3 X-Ray Diffraction and Electron BackScatter Diffraction.....	19
CHAPTER 3 DISLOCATIONS	22
3.1 Edge and Screw Dislocations	22
3.1.1 Edge Dislocations.....	23
3.1.2 Screw Dislocations.....	24
3.2 Interaction of dislocations	26
3.2.1 Forces associated with dislocations.....	26
3.2.2 Some sources of Dislocations	30
3.2.2.1 Frank Read Source.....	31
3.2.2.2 Multiple Cross slip	32
3.2.3 Dislocations near Grain boundaries	33
CHAPTER 4 STRESSES AND STRAINS IN CRYSTALS.....	36
4.1 Engineering and Instantaneous stress and strain	36
4.2 Flow curve and Yielding criteria	38
4.2.1 The Flow Curve	38
4.2.2 Yielding criteria	39
4.3 stresses and strains in single-crystals and polycrystals	41
4.3.1 Plastic Deformation in Single Crystals.....	42
4.3.2 Plastic Deformation in Polycrystals	44
CHAPTER 5 CONSTITUTIVE LAWS	46
5.1 Phenomenological Power Law for FCC crystals	46

CHAPTER 6 THE SPECTRAL METHOD: POLARISATION.....	49
6.1 The kinematics	49
6.2 Static Equilibrium	50
6.3 Numerical Implementation	52
6.3.1 polarisation scheme of discretization	52
6.3.2 Numerical solution strategy	53
CHAPTER 7 PROCEDURE.....	55
7.1 Setting up the Geometry files in DAMASK environment.....	56
7.2 Setting up the Material configuration.....	60
7.3 Setting up the Numeric Configuration	61
7.4 Simulation.....	61
7.4.1 Simulation by the Spectral Method.....	61
7.4.2 Simulation by Finite element method.....	62
7.5 Analysis tools used to obtain and compare results.....	62
CHAPTER 8 RESULTS AND CONCLUSIONS	64
APPENDICES.....	84
APPENDIX A AUTOMATOR CODE.....	85
APPENDIX B MATERIAL CONFIGURATION FILE	91
APPENDIX C NUMERICS CONFIGURATION FILE.....	100
APPENDIX D ALTERATIONS TO NUMERICS CONNFIGURATION FILE	104
APPENDIX E LOADCASE FILE	105
APPENDIX F QUEUE SUBMISSION FILE.....	106
APPENDIX G POST PROCESSING	108
APPENDIX H EULER ANGLES FROM GEOMETRY FILE HEADER	110
BIBLIOGRAPHY	112

LIST OF FIGURES

Figure 2.1	Silar SC-9M silicon carbide whiskers. Each of these whiskers is a single crystal. Source: acm-usa.com/silar-sc-9m.....	4
Figure 2.2	The fourteen Bravais lattices in three dimensions. Source: D.V.Anghel, <i>Bravais lattice table</i> , 2003.....	6
Figure 2.3	Example planes and directions showing miller indices for each in cubic unit cells. Source: http://pms.iitk.ernet.in/wiki/index.php/	8
Figure 2.4	The shape of the fundamental zone in Rodrigues space. Source: Drawn by the author using Microsoft Paint program.....	13
Figure 2.5	Grain boundaries showing mismatch between grains. Source: www.engineeringarchives.com/	14
Figure 2.6	(100) pole figures for sheet material, illustrating (left) random orientation and (right) preferred orientation. RD (rolling direction) and TD (transverse direction) are reference directions in the plane of the sheet. Source: <i>Elements of X-Ray Diffraction</i> , B.D.Cullity, 1956.....	16
Figure 2.7	Stereographic projection sphere with the plane on the north pole. It also shows the projection of the south pole onto this plane. Source: Mark Howison at English Wikipedia; https://en.wikipedia.org/wiki/Stereographic_projection	16
Figure 2.8	Wulff net or stereonet. It is used for plotting stereographic projection of poles and/or points manually.....	17
Figure 2.9	Standard Inverse pole figure for a cubic crystal. The [100],[010] and [001] are parallel to the i,j , and k respectively. Source: <i>Applied Mechanics of Solids</i> by A. F. Bower, Chapter 3.....	18
Figure 2.10	EBSD micrographs of hot-rolled and annealed titanium samples, along with the IPF color coded triangle for hexagonal close packed metals. Scale bar= 200 μm . This is for representation purposes only; for details about the labels in the micrographs, please be referred to the source: " <i>The importance of crystallographic texture in the use of Titanium as an orthopedic biomaterial</i> ", by Bahl et al, J. RSC Advances, August 2014. the purpose of this figure is to demonstrate how an EBSD texture map may look like.....	20
Figure 3.1	Visualization of an edge dislocation as an extra half plane of atoms in the lattice. The burgers vector(shown in black color) is perpendicular to	

the dislocation line(shown in blue).....	23
Figure 3.2 Visualization of a screw dislocation.....	24
Figure 3.3 Visualization of a screw dislocation in a plane. The red atoms are already displaced, i.e, the dislocation has passed through; the blue ones are yet to be displaced while the green ones are in the process of moving and can be together called as the screw dislocation. Source: https://www.nde-ed.org/EducationResources/	25
Figure 3.4 Visualization of stress fields around an edge dislocation. The dislocation line itself is perpendicular to the plane of the paper. σ_{zz} which is just the sum of σ_{xx} and σ_{yy} has not been shown. '+' represents tension, and '-' represents compression. Source: G.E.Dieter, Mechanical Metallurgy, 3rd Edition.....	28
Figure 3.5 Visualization of stress contour (σ_{xz}) around a screw dislocation. the dislocation line is perpendicular to the plane of paper, x to the right and y to the top in the plane of the paper. the stress is always shear.....	29
Figure 3.6 Visualization of stress contour (σ_{yz}) around a screw dislocation. the dislocation line is perpendicular to the plane of paper, x to the right and y to the top in the plane of the paper. the stress is always shear.....	29
Figure 3.7 Visualization of stages of Dislocation multiplication by the Frank-Read mechanism under shear on a slip plane. A and B are the pinning points, and τ is the applied shear stress. Source: Jntf - Own work, CC BY-SA 3.0, https://commons.wikimedia.org/w/index.php?curid=7501825	32
Figure 3.8 Visualization of stages of multiple cross slip of the screw component of a mixed dislocation. The planes (111) are the family of slip planes.....	33
Figure 4.1 True stress vs true strain for a ductile solid. σ_0 is the yield stress, ' $\varepsilon_1 - \varepsilon_2$ ' is the <i>recoverable elastic</i> strain, and ' $\varepsilon_2 - \varepsilon_3$ ' is the <i>anelastic</i> behavior which is mostly neglected in mathematical theories of plasticity. Source: <i>Mechanical Metallurgy by George.E.Dieter, Chapter-3, Section 3-2</i>	38
Figure 4.2 Resolved shear stress in a single crystal. Source: <i>Mechanical Metallurgy by George.E.Dieter, Chapter-4, Section 4-7; E.Schimd, Z. Elektrochem., vol. 37,p. 447, 1931</i>	42
Figure 7.1 Comparison of their IPF color maps, with those produced by our software. The figures on the left are those produced at SNL, experimentally in the EBSD. The ones at the right are produced by the imageDataRGB command	

in DAMASK	56
Figure 7.2 The 2 dimensional geometry file (thickness in z direction = 1) which will be extruded. The x axis is towards the right and the y axis is upwards.....	57
Figure 7.3 The Oligocrystal, made by extruding the 2D structure in the z direction. The aspect ratios have been maintained. Resolution: 1084x294x168. Voxel aspect ratio x:y:z ::1:1:1.....	57
Figure 7.4 The Oligocrystal with the isotropic airlayer around it.....	58
Figure 7.5 The Oligocrystal with the rigid elastic baseplate added at both ends. This makes the baseplate continuous because of the periodic structure and renders the air layer discontinuous.....	59
Figure 7.6 The rigid baseplate is added first in this new assignment of boundary conditions.....	59
Figure 7.7 The isotropic plastic air layer is added around the baseplate and the Oligocrystal. This makes the baseplate periodically discontinuous, while the airlayer becomes continuous.....	60
Figure 8.1 The HRDIC versus CPFEM strain maps. The column of images on the left shows the strain map of the oligocrystal obtained by high resolution digital image correlation, while those on the left are obtained by CPFEM. In our work we have focused only on the strain in the x direction, i.e., ϵ_{xx} . The positive x direction is towards the right, and positive y is upwards.....	64
Figure 8.2 The strain map generated in three dimensions by DAMASK. The color scale has been modified so that anything above 0.3 is the same shade of red as 0.3, and anything below 0 is the same shade of blue as 0.....	65
Figure 8.3 The comparison of strain maps upon change of boundary conditions. Left side images show the results that had the older boundary conditions, while those on the right have the newer boundary conditions.....	66
Figure 8.4 The comparison of strain maps upon change of boundary conditions, shown as the cumulative probability of ratios of strains at each material point calculated with the two different periodic boundary conditions.....	67
Figure 8.5 The comparison of strain maps upon increasing resolution in the z-direction. Left side images show the results that had been obtained with a lower z resolution, while the right shows the results obtained after increasing the z resolution by a factor of 2. As is evident just by visual inspection, the change in increasing the z resolution does not effect any major change, but the gradients become smoother.....	68

Figure 8.6 The quantitative comparison of strain maps upon change of z resolution. cumulative probability of the ratio of strains calculated at each material point for resolution 271x74x21 to those at 271x74x10 has been shown.....	69
Figure 8.7 The comparison of grain rotations upon increasing resolution in the z direction. Left side images show the results that had been obtained with a higher z resolution. As is evident just by visual inspection, the change in increasing the z resolution does not effect any major change.....	70
Figure 8.8 The quantitative comparison of grain rotation maps upon change of z resolution. Cumulative probability of the ratios of grain rotations calculated at each material point for the resolution 271x74x21 to those calculated at 271x74x10.....	71
Figure 8.9 The grain rotation spatial map after simulating a rotated geometry. Mesh resolution 271x10x74, voxel aspect ratio 1:4:1. The top face and front face are interchanged from previous simulations because y and z directions are now interchanged due to the rotation. The band-like structure still exists in the thickness direction. The thickness direction was z in the previous ones, but y in the current one.....	72
Figure 8.10 The grain rotation spatial map after simulating an unrotated geometry with equiaxed voxels. Mesh resolution 271x74x42, voxel aspect ratio 1:1:1. Little to no banding can be seen in the thickness direction. Thus, an equiaxed voxel is desirable.....	72
Figure 8.11 The grain rotation spatial maps comparing the CPFEM and spectral solution estimations of grain rotations. Mesh resolution 271x74x10, voxel aspect ratio 1:1:4. Little to no banding can be seen in the CPFEM solution. Spectral solution estimates higher grain rotation than FEM near the grain boundaries, but most of the other places, they estimate similar values of grain rotation as seen in Figure8.12.....	73
Figure 8.12 The cumulative probability of ratios of grain rotations calculated by FEM to those calculated by spectral solution.....	74
Figure 8.13 The grain rotation spatial maps for different resolutions. the calculations are done by spectral method. There seems to be no effective change except smoothing upon increasing resolution.....	75
Figure 8.14 Quantitative comparisons of grain rotations at different resolutions. The range of the ratios is from 0.1 to 5.0 which indicates similarity between the spatial maps showing grain rotations.....	76
Figure 8.15 Spatial maps for strains calculated by CPFEM and spectral solution.They look similar except for the regions near the grain boundaries.....	77

Figure 8.16 Quantitative comparisons of strains calculated by FEM and spectral method. The range of the ratios of strains calculated by FEM to those by spectral method is from 0.1 to 5.0 which indicates similarity between the spatial maps showing the strains.....	77
Figure 8.17 Distance from closest grain boundary versus ratio of spectral solution method strains to fem strains.....	78
Figure 8.18 Spatial maps of spectrally calculated strains at various resolutions.....	78
Figure 8.19 Quantitative comparison of strains calculated at various resolutions by the spectral method.....	79
Figure 8.20 Distance from closest grain boundary versus normalized strains calculated spectrally for 271x74x10 resolution.....	80
Figure 8.21 Distance from closest grain boundary versus normalized strains calculated spectrally for 542x147x21 resolution.....	81
Figure 8.22 Distance from closest grain boundary versus normalized strains calculated spectrally for 1084x294x21 resolution.....	82
Figure 8.23 Distance from closest grain boundary versus normalized strains calculated by FEM at 271x74x10 resolution.....	83

CHAPTER 1

INTRODUCTION

Experimental methods of studying deformation behavior of polycrystals has always been challenging and more often than not destructive. Heterogeneous grain morphology, variation in the crystal orientation of each grain and many times within a grain, discontinuities at the grain boundaries, and neighboring effects due to presence of other grains only adds to the challenge of understanding what happens when polycrystals deform. A computational methodology has grown popular among scientists and researchers because it is non destructive, and CPFEM simulations have become mainstream in polycrystal deformation research. It thus becomes imperative to scrutinize this technique and to discover its limitations in order to overcome them, or to go for other computational strategies such as the Spectral Solution method. One of the main considerations while judging which computational method to employ, is computational cost which directly depends on the speed with which the algorithm processes data and computes the results, which in turn is a direct result of the grid size used: the finer the grid, the higher the resolution, the higher the computational cost. A desirable trait in a computational methodology would be an optimum between fast calculations and higher resolutions. Ideally, one would want faster and faster computation at higher and higher resolutions. The CPFEM suffers from a shortcoming that is inherent in the algorithm: the computational cost is prohibitively high at rather high resolutions. Spectral Solution method that works by employing fast Fourier transforms can handle high resolutions without a prohibitively high computational cost, and is also much less stiffer than the FEM. This has been explored later when the spectral solution method has been dealt with, in greater detail. Investigation has been done on whether this shortcoming of the FEM affects the calculation of Grain Boundary strains in our Oligocrystalline sample, and whether the underestimation of these strains can be attributed to this shortcoming. To this end, Spectral Solution method included in the DAMASK (Düsseldorf Advanced Materials Simulation Kit) to solve for the strains in the uniaxially loaded

Oligocrystalline metallic sample was employed.

An oligocrystalline sample is a multi-crystal sheet metal sample in which the grain morphology on both the top and bottom faces are almost identical, and the grains themselves are relatively coarse and columnar. They extend throughout the cross section of the sample. Such a system is relatively easy to simulate and analyze as compared to an even more generic polycrystal as they do away with subsurface microstructures. In this case, a face centered cubic crystal system has been assigned to the metal. We have assumed that there is no significant changes in orientation inside each grain, and we have used a 5 degrees tolerance angle; i.e, only orientations differing more than 5 degrees should be considered as a different grain. This was done to reduce complications in the calculations, and to remove redundancies. Also, the number of grains computed comes down to 19 or 20 (depending on mesh resolutions), which is the same as that calculated experimentally. If a tolerance angle less than that is used, then there is a risk of increasing the number of grains and grain boundaries. Since the earlier paper by Lim et al^[1] uses uniaxial tension in the x direction, this work has used the same as well. This was an obvious choice because an uniaxial tensile stress and its effects have been most widely studied, documented, and analyzed. Both in single crystals as well as polycrystals, deformation happens under uniaxial load after a critical stress has been exceeded. The stress-strain curves for oligocrystalline materials follow the usual shape for all polycrystals, i.e, linear, reversible elastic deformation at first, and then irreversible non linear plastic deformation. The sample was allowed to deform only in the y and z directions as it is pulled in the x direction. The YZ faces on both ends are attached to a rigid structure with very high elastic modulus and no plasticity, while an isotropic air layer, which allows dilatational changes, surrounds the XY and XZ faces of the sample. This provides us with a rather simple, and somewhat realistic set of boundary conditions to set up our model and do the simulations.

In the following chapters, we deal with more background information on crystals; grains, grain orientations and misorientations; stresses, strains and their effects; computational strategies; and our experimental procedures, results and conclusions, in greater depth and detail.

CHAPTER 2

CRYSTALS

Most of the materials that we deal with regularly in our daily life are crystalline in nature. A long range order in the spatial arrangement of atoms in a material is the root cause of crystallinity in that material. Amorphous materials have short range order. However, many crystalline materials in nature, exist as an aggregate of smaller crystals. such crystals are termed ‘polycrystals’. The individual single crystals that make up the aggregate are called ‘grains’ and the boundary between two such three-dimensional grains is a two dimensional surface termed as ‘grain boundaries’. The grains have point defects like vacancies and one dimensional defects like dislocations, and these react to applied stress. The interaction of these defects among themselves and with the grain boundaries, plus the effect of the changes in one grain on another, determine the stress response and strains in the polycrystal. We discuss these defects and their interactions in other chapters. In the following sections of this chapter, we consider single crystals without any defects, which form the bulk of the individual grains; unit-cells, lattices and crystallographic directions and planes; orientations, misorientations and textures in a polycrystal; ways of representing these in polycrystals, i.e, euler angles, quaternions, rodrigues vectors, etc; and some experimental techniques such as EBSD that can provide texture maps from physical samples.

2.1 Perfect Single Crystal

A perfect single crystal is a crystalline material with long range spatial arrangement of atoms or molecules without any defects and grain boundaries. It is exactly one crystal with an unbroken lattice, except for the surface where it is exposed to the surrounding material (generally the atmosphere). These crystals are rarely found in nature, because presence of defects implies more entropy, and minimization of overall free energy and hence defect formation is favored in nature.

However, in laboratories, under specially enforced conditions, single crystals can be grown. Some examples are nanorods and whiskers (shown in Figure 2.1).

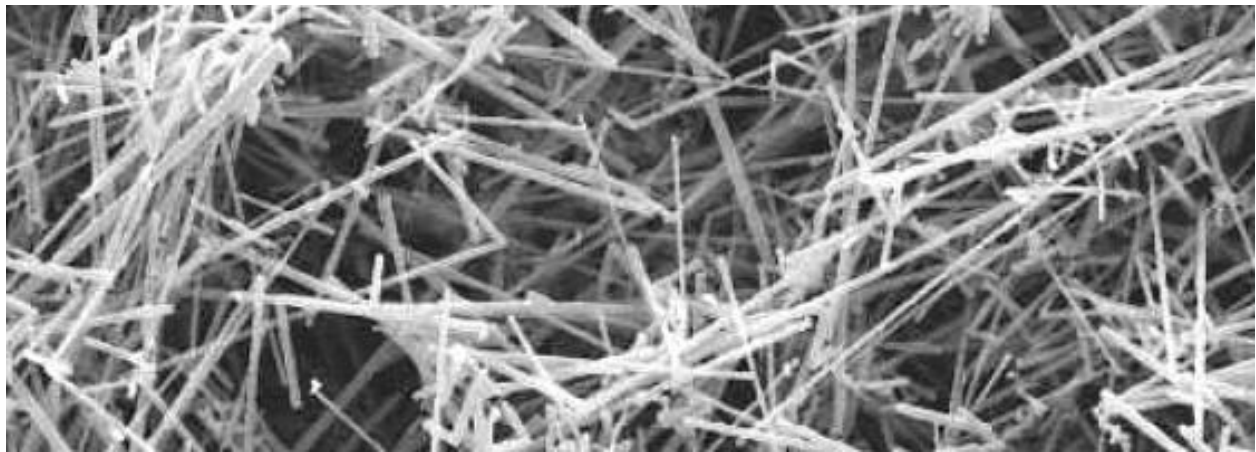


Figure 2.1: Silar SC-9M silicon carbide whiskers. Each of these whiskers is a single crystal.

Source: acm-usa.com/silar-sc-9m

These are grown either as reinforcements in special composite materials or as samples to find out the ideal material properties. the applications are mostly research based, however, and the tests done on single crystals provide us with the standardized constants such as shear strength, elastic and shear modulus, etc.

2.1.1 Lattices and unit cells

In mathematics, particularly in *group theory*, a *lattice* in an *n-dimensional* real vector-space R^n is a subgroup of R^n which is isomorphic to Z^n , and which spans R^n fully. Simply put, for any *basis* of R^n , the subset of all linear combinations with integral coefficients, forms a lattice in n dimensions. In crystallography, a **Bravais lattice**, or simply a lattice is an infinite array of discrete points repeating in three dimensions which is generated by *discrete translation* operations described by

$$R = n_1 a_1 + n_2 a_2 + n_3 a_3 \quad (2.1)$$

where n_i are integers and a_i are the primitive vectors which lie in arbitrary directions (but linearly independent) and span the entire lattice. One condition is that these discrete set of vectors must

form a closed triangle when vector addition or subtraction is operated on them. Also, for any choice of the position vector \mathbf{R} in the real vector space, the lattice looks identical.

This formal discussion about Lattices and Bravais lattices is important because this concept is used to define a *crystalline arrangement* and its limitations. one or more atoms of the crystalline substance forms the basis and the periodic repetition of this basis at each lattice point makes up the crystal structure. As a result, the crystal will look the same when viewed from any similar, or equivalent lattice point. Equivalent lattice points are those separated by one translation of the ***unit cell***.

A unit cell is the simplest arrangement of one or more atoms that when reproduced periodically, can generate the entire crystal; i.e, the unit cells stacked in three dimensions, will form the bulk arrangement of the atoms in the crystal. A unit cell can be completely described by the length of its edges a , b , and c and the angles between them. The angle between a and b is γ , that between b and c is α and between a and c is β . Together, these edges and angles are termed as *lattice parameters*.

In three dimensional space, there are 14 kinds of *Bravais lattices*, and these are grouped into seven lattice systems or crystal systems, namely Triclinic, Monoclinic, Orthorhombic, Tetragonal, Rhombohedral(trigonal), Hexagonal, and Cubic, as shown in Fig. 2.2 There are four types of unit cells, namely Primitive (or simple), volume or Body centered, Face centered, and Base or End centered. sometimes, the simple primitive rhombohedral (trigonal) unit cell is said to be a special kind of unit cell in tis own right. Not all combinations of lattice systems and unit cell types are needed to describe the possible crystal systems in nature because most of these are equivalent to each other and only one of those is enough. That is why, even though in theory we should have 42 possible Bravais lattices, we have just 14.

2.1.2 Crystallographic directions and Planes

In a 3-dimensional crystal lattice, crystallographic planes and directions are important to understand how symmetry, or the lack thereof plays an important role in the properties of a crystalline solid. Crystalline materials are generally non isotropic solids and particular lattice planes and

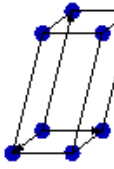
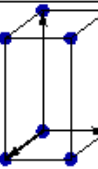
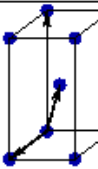
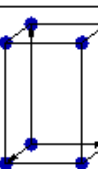
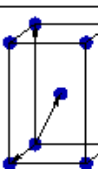
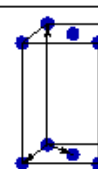
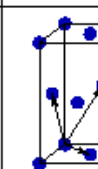
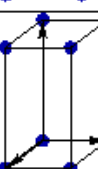
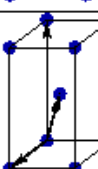
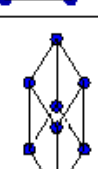
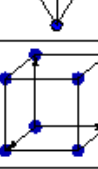
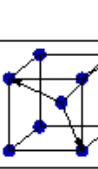
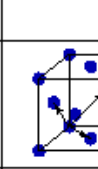
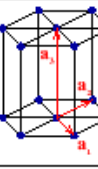
Bravais lattice	Parameters	Simple (P)	Volume centered (I)	Base centered (C)	Face centered (F)
Triclinic	$a_1 \neq a_2 \neq a_3$ $\alpha_{12} \neq \alpha_{23} \neq \alpha_{31}$				
Monoclinic	$a_1 \neq a_2 \neq a_3$ $\alpha_{23} = \alpha_{31} = 90^\circ$ $\alpha_{12} \neq 90^\circ$				
Orthorhombic	$a_1 \neq a_2 \neq a_3$ $\alpha_{12} = \alpha_{23} = \alpha_{31} = 90^\circ$				
Tetragonal	$a_1 = a_2 \neq a_3$ $\alpha_{12} = \alpha_{23} = \alpha_{31} = 90^\circ$				
Trigonal	$a_1 = a_2 = a_3$ $\alpha_{12} = \alpha_{23} = \alpha_{31} < 120^\circ$				
Cubic	$a_1 = a_2 = a_3$ $\alpha_{12} = \alpha_{23} = \alpha_{31} = 90^\circ$				
Hexagonal	$a_1 = a_2 \neq a_3$ $\alpha_{12} = 120^\circ$ $\alpha_{23} = \alpha_{31} = 90^\circ$				

Figure 2.2: The fourteen Bravais lattices in three dimensions. Source: D.V.Anghel, *Bravais lattice table*, 2003.

directions show enhanced properties than others. Crystallographic directions are straight lines linking atom positions, or nodes, while crystallographic planes are two dimensional planes linking the nodes. Certain planes and directions have higher density and better packing of atoms, and thus have a higher density of nodes. Optical properties such as refractive index are directly related to

periodic fluctuations in density; surface adsorption and reactivity are dependent on the density of nodes; higher density of nodes correspond to lower surface tension; microstructural defects such as pores usually have straight boundaries immediately after high density planes ; mechanical behavior such as fracture, cleavage, slip, etc occur preferentially along high density planes in a crystal, and so does dislocation glide and movement because the burgers vector is always along a close packed direction and plane. The planes and directions are generally represented in terms of Miller indices, or Miller-Bravais indices, and there exist families of equivalent planes and families of equivalent directions as we shall discuss below.

A family of planes or directions in a lattice or in an unit cell is determined by three integers h , k , and l for planes or u , v and w for directions. These are known as the Miller-indices for Planes and Directions respectively. For planes, they are written as $(h k l)$ and denote the family of planes that are orthogonal to $hb_1 + kb_2 + lb_3$, where b_i forms the basis for vectors in the reciprocal lattice. The reciprocal lattice vectors need not be mutually orthogonal and hence the plane is not necessarily orthogonal to a linear combination of direct lattice vectors. Conventionally, the negative integers in a set of miller indices for either planes or directions, is denoted with a bar over the integer, and all integers are written in lowest terms. Due to lattice symmetry, all planes equivalent to $(h k l)$ are grouped together as a family of planes: $\{h k l\}$. Alternatively, the Miller indices are proportional to the *inverse* of the intercepts of the plane, in the basis of the vectors in the lattice. Thus, if one of the indices has a value of 0, then the plane does not intersect that axis as the intercept, or the inverse of 0, is infinity. For example, if the plane intercepts the Lattice vectors a , b and c at 1, -0.5 and 0.5, then the *Miller indices* are $(2 \bar{1} 1)$. Usually, in cubic crystal systems, many families of planes exist, for example $\{100\}$, $\{110\}$, $\{111\}$, etc.

For directions, the indices are defined as magnitude of the intercepts of the direction with the orthogonal vectors a , b and c , in their lowest whole number forms. For example, if a crystal direction has intercepts 0.5, -1 and -0.5 on the a , b and c axes respectively, then the direction can be denoted as $[1 \bar{2} \bar{1}]$. Families of directions are denoted as $\langle u v w \rangle$. In *fcc* lattice, the $\{111\}$ family of planes are the slip planes. Along with the $\langle 110 \rangle$ family of directions, we have 12 slip-

systems. Miller indices for the directions and planes are thus extremely useful in crystallography for studying the planes, orientations, directions of slip, etc. Figure 2.3 shows the [0 1 0] direction with (0 0 1) plane, and the [1 1 0] direction with the (1 1 0) plane.

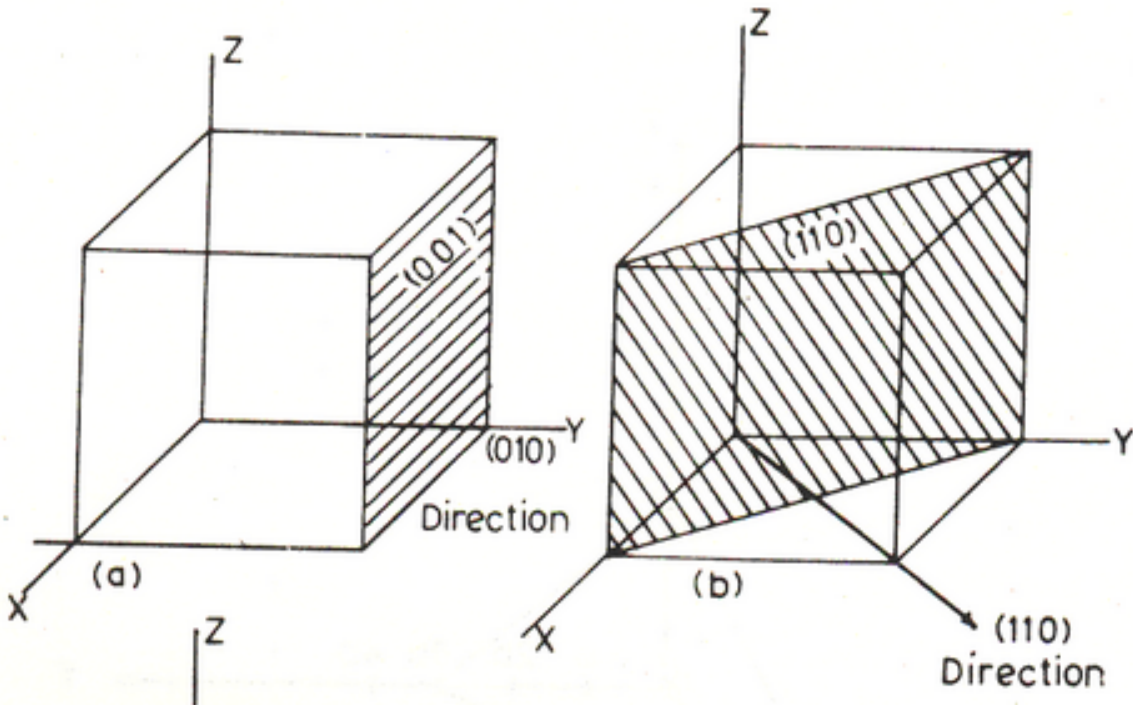


Figure 2.3: Example planes and directions showing miller indices for each in cubic unit cells.

Source: <http://pms.iitk.ernet.in/wiki/index.php/>

2.1.3 Crystal Orientation

Crystal orientation refers to the manner in which the crystal is oriented in three dimensional space. It is denoted generally in terms of Quaternions, Euler Angles, or as Rotation Matrices. These are angle-axis representations of crystal Orientations. All of these orientations are relative to a coordinate system outside of the crystal, known as the "*Laboratory Coordinates*". There is a coordinate system inside the crystal, known as *Crystal Coordinates*.

2.1.3.1 Quaternions

According to *Euler's Rotation Theorem*, any single rotation, or a sequence of rotations of a rigid body or a coordinate system around a point fixed in space, is equivalent to exactly one rotation by a given angle θ about an axis fixed in space that runs through the said fixed point. Thus any rotation in space can be denoted by a vector \vec{u} and a scalar θ . Quaternions provide an easy way of representing this angle and axis information in terms of four numbers. These set of four numbers can be used to apply any particular orientation to a position vector that represents a point relative to an origin in a real three dimensional space. In other words, a rotation through an angle θ around an axis defined by a unit vector $\vec{u} = (u_x, u_y, u_z) = u_x\hat{i} + u_y\hat{j} + u_z\hat{k}$ can be represented by a Quaternion:

$$\mathbf{q} = e^{\frac{\theta}{2}(u_x\hat{i} + u_y\hat{j} + u_z\hat{k})} = \cos\left(\frac{\theta}{2}\right) + i(u_x\hat{i} + u_y\hat{j} + u_z\hat{k}) \times \sin\left(\frac{\theta}{2}\right) \quad (2.2)$$

The real part of this quaternion is denoted as w . This rotation can be assigned to an ordinary position vector $\mathbf{p} = p_x\hat{i} + p_y\hat{j} + p_z\hat{k}$ to get the final orientation $\mathbf{p}' = q \cdot \mathbf{p} \cdot q^{-1}$. In a computer program, this is achieved by constructing a quaternion whose vector part is \mathbf{p} and real part (w) equals zero and then performing the quaternion multiplication. The vector part of the resulting quaternion is the desired vector \mathbf{p}' .

2.1.3.2 Euler Angles

In crystallography, the Bunge Euler angles are extensively used, and these can be defined as a sequence of rotations of the crystallographic axes with reference to the spatial axes. The first rotation is around the Z axis by an angle ϕ_1 , the second around the new X axis by an angle ϕ , and the third is around the new Z axis by an angle Φ_2 . ϕ_1 , ϕ , and Φ_2 are the Bunge Euler angles that are used to represent the crystal orientations, as each grain in a polycrystal will have a unique set of these angles. Computationally, while modeling, if two points have the same set of angles within a few degrees tolerance (0.5° to 3° usually) then they are said to be in the same grain. In a single crystal, the entire crystal has the same orientation(within allowed tolerance), despite presence of dislocations.

2.1.3.3 Rotation Matrices

Rotation matrices are the matrix version of Angle-Axis representations such as Euler angles or quaternions, and can be used to denote orientations equally skilfully. Although Euler Angles and quaternions are more widespread, concise and efficient, Rotation matrices are usually obtained as raw data (as in our case) and then converted into Euler Angles or quaternions as operations on those are computationally efficient and costs less as regards the time taken for computation.

The rotation matrix from quaternions can be written as:

$$R_q = \begin{bmatrix} 1 - 2q_j^2 - 2q_k^2 & 2(q_i q_j - q_k q_r) & 2(q_i q_k + q_j q_r) \\ 2(q_i q_j + q_k q_r) & 1 - 2q_i^2 - 2q_k^2 & 2(q_j q_k - q_i q_r) \\ 2(q_i q_k - q_j q_r) & 2(q_j q_k + q_i q_r) & 1 - 2q_i^2 - 2q_j^2 \end{bmatrix} \quad (2.3)$$

where $\mathbf{q}_r = w$ and \mathbf{q}_{ijk} are the imaginary components of the quaternion representation.

Similarly, a rotation matrix from an Angle-Axis representation, wherein rotation happens by an angle θ around an axis along the direction $\hat{\mathbf{u}}$ would look like:

$$R_{aa} = \begin{bmatrix} \cos \theta + u_x^2(1 - \cos \theta) & u_x u_y (1 - \cos \theta) - u_z \sin \theta & u_x u_z (1 - \cos \theta) + u_y \sin \theta \\ u_x u_y (1 - \cos \theta) + u_z \sin \theta & \cos \theta + u_y^2(1 - \cos \theta) & u_z u_y (1 - \cos \theta) - u_x \sin \theta \\ u_x u_z (1 - \cos \theta) - u_y \sin \theta & u_z u_y (1 - \cos \theta) + u_x \sin \theta & \cos \theta + u_z^2(1 - \cos \theta) \end{bmatrix} \quad (2.4)$$

In a simpler form, $R = \cos \theta \cdot I + \sin \theta [\mathbf{u}]_\times + (1 - \cos \theta) \mathbf{u} \otimes \mathbf{u}$ where $[\mathbf{u}]_\times$ is the *cross product matrix* of \mathbf{u} , \otimes is the tensor product and I is the identity matrix. This is the matrix form of the *Rodrigues' rotation formula*. According to the *Right hand rule*, rotations will be anticlockwise when \mathbf{u} points towards the observer, and shall be considered as positive rotations. If \mathbf{u} points away from the observer then the rotation will be clockwise and considered negative.

Bunge Euler Angles can also be represented as a rotation matrix as follows:

$$R_e = \begin{bmatrix} c_1 c_3 - c_2 s_1 s_3 & -c_1 s_3 - c_2 c_3 s_1 & s_1 s_2 \\ c_3 s_1 + c_1 c_2 s_3 & c_1 c_2 c_3 - s_1 s_3 & -c_1 s_2 \\ s_2 s_3 & c_3 s_2 & c_2 \end{bmatrix} \quad (2.5)$$

where $c_1 = \cos \phi_1, c_2 = \cos \phi, c_3 = \cos \phi_2$ and $s_1 = \sin \phi_1, s_2 = \sin \phi, s_3 = \sin \phi_2$, wherein ϕ_1, ϕ and ϕ_2 are the Bunge-Euler angles.

2.2 Polycrystals

Crystalline materials, do not exist as perfect single crystals in nature. More often than not, dislocations and other defects exist in crystals. Also, during solidification, many nuclei grow simultaneously. Not all of them have the same crystal orientation, and upon solidification, two crystals with different orientations (usually beyond a certain tolerance limit called *misorientation angle*) are termed as two grains in the same overall crystalline solid. Such a solid with many such grains, each grain generally having a different crystal orientation than its neighbors, is called as a polycrystals. Reasons for abundance of polycrystals is that dislocations, preferential growth of certain nuclei, and inherent randomness increase the entropy of the system as a whole and decrease the overall free energy.

The main characteristics of polycrystals that set them apart from single crystals are the presence of grain boundaries, and the misorientations among the grains that many times act as dislocation sources and make polycrystals easily deformable than single crystals, at least initially.

2.2.1 Misorientations and grain boundaries

Many unit cells constitute a crystal. There is generally a slight gradient of orientations of the unit cells in the lattice. This means, that orientations of unit cells, or between clusters of unit cells, are not always exactly the same. Within a grain, these variations are usually within a fraction of a degree to a couple degrees. This mismatch is called as Misorientation. The boundaries between these crystals that are within a fraction of a degree to a couple degrees of misorientation, are called *low angle boundaries*. When the misorientation exceeds the limit, then it can safely be assumed that we are in another grain. The boundaries between such crystals are called *High angle grain boundaries*. In modeling, we can assign the maximum allowed misorientation within a grain, and if that limit is exceeded, then we assign another grain identity to that orientation. This gives us control over our model and we can manipulate the number of grains in our virtual polycrystal, by using this parameter.

There is another way of describing orientations in space, known as the Rodrigues' rotation formula. It states that

$$\mathbf{v}_{\text{rot}} = \mathbf{v} \cos \theta + (\hat{\mathbf{k}} \times \mathbf{v}) \sin \theta + \hat{\mathbf{k}}(\hat{\mathbf{k}} \cdot \mathbf{v})(1 - \cos \theta) \quad (2.6)$$

where \mathbf{v} is a vector in R^3 (real space) and $\hat{\mathbf{k}}$ is a unit vector which represents the axis of rotation about which \mathbf{v} rotates through an angle θ in compliance with the *right hand rule*. When we represent orientations in the Rodrigues' space, we represent them as points. Each of those points has a position vector \mathbf{v}_{rot} . This is useful to show misorientation. Misorientation within a grain is of the order of a fraction of an angle to a couple angles, and all such orientations cluster together because they are very close to each other, in Rodrigues space. When we exceed those values, we move into another grain, which in Rodrigues space, is another cluster of points, which may or may not be close to the first cluster. Thus, if we plot all the orientations of a polycrystal in Rodrigues space, the number of point clusters gives us the number of grains. While modeling a polycrystal, we can manipulate the misorientation tolerance, and thus we have control over the number of grains that we want in our polycrystal, and also to simplify our model and thereby reducing computational cost. In our work, we used this concept to manipulate the tolerance while modeling, in order to match the number of grains in our model with that in the actual Oligocrystal that Lim et al^[1] used in their experiment.

However, due to inherent periodicity, and a need to represent orientations completely randomly, generally a fundamental zone in Rodrigues space is conceptualized. All the crystal orientations are visualized within this fundamental zone. This zone looks like a cube with all its corners cut off, as shown in Fig. 2.4

Points that lie outside the borders of this zone, appear on the other side of this zone owing to periodicity. It is thus imperative to be able to clearly distinguish such mirror images from actual orientations, or we might end up concluding that we have more number of grains than we had initially intended.

Grain boundaries, or rather, *High Angle Grain Boundaries* are two dimensional entities, or

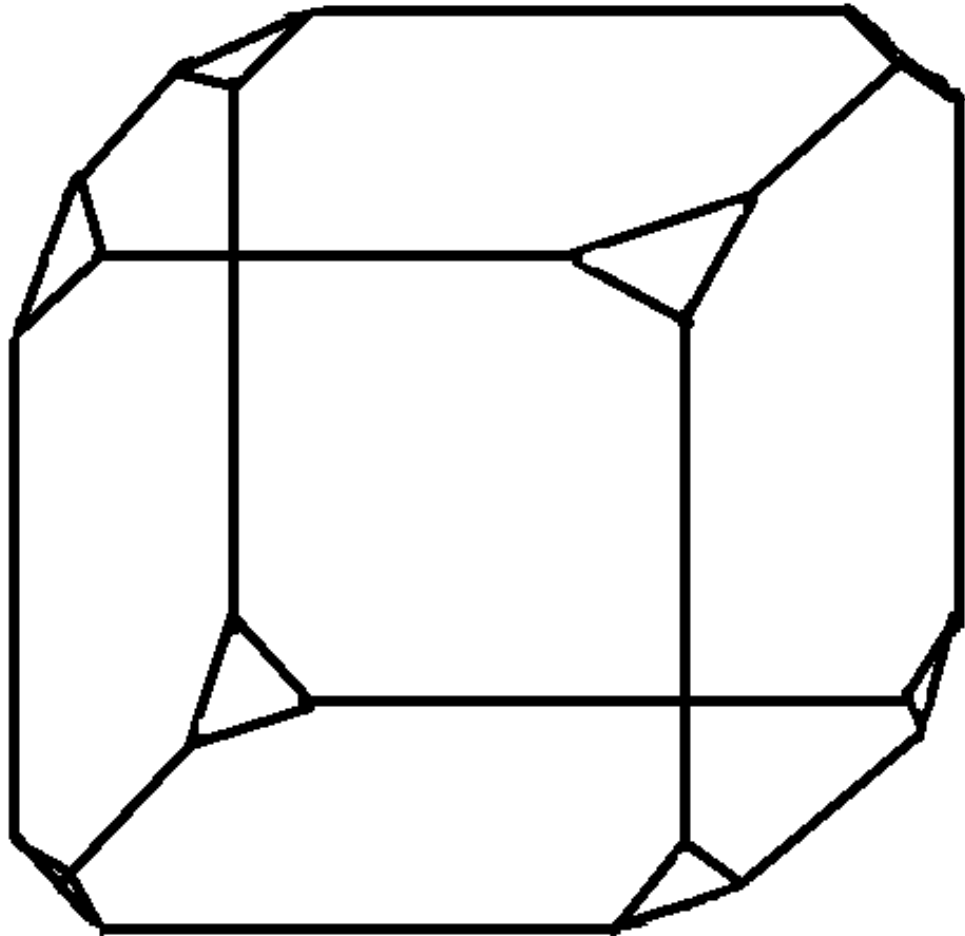


Figure 2.4: The shape of the fundamental zone in Rodrigues space. Source: Drawn by the author using Microsoft Paint program

surfaces, that mark the transition from one grain to another, i.e., when the misorientation exceeds the allowed tolerance within a grain. Physically, a grain boundary (shown in Fig. 2.5) is an array of dislocations, that traces the boundary between two grains. When the misorientation is greater than 15° then the dislocations become so close that their cores overlap and individual dislocations cannot be distinguished anymore. The energy of this boundary becomes independent of the misorientation angle, with the exception of a few special orientations. The Presence of a large number

of dislocations, make the grain boundaries undergo more strain, and act as barriers to slip. We shall delve deeper into this in the forthcoming chapters.

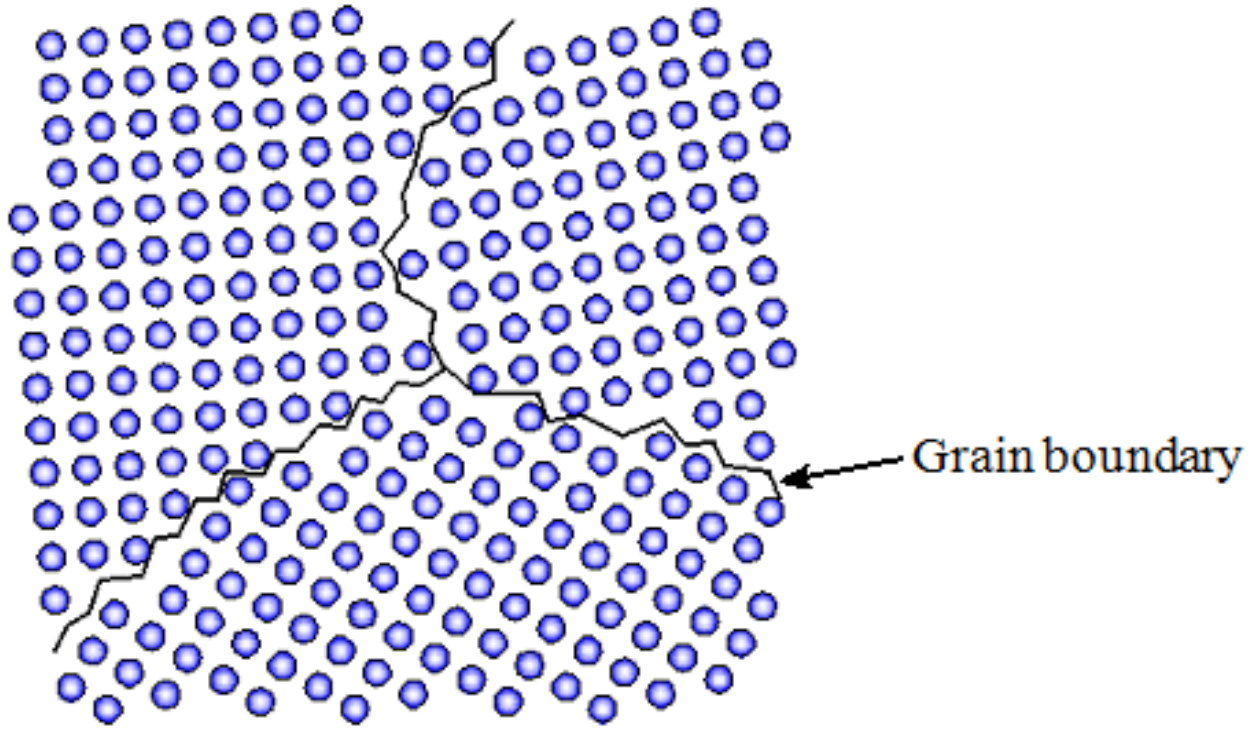


Figure 2.5: Grain boundaries showing mismatch between grains.

Source: www.engineeringarchives.com/

2.2.2 Texture and its representation

An obvious question that comes to mind after the discussion about orientations, is how do we represent them without making it too mathematically involved. A pictorial representation of texture data is very important as it can successfully and efficiently show the texture information without being too erudite. To this end, we have numerous techniques like color maps, Stereographic Projections, inverse pole figures, Electron Back Scatter Diffraction (EBSD) maps, etc, that help us in representing the texture of a polycrystal in a single image file. The color maps have legends associated with them that contain the orientation data of the grains. In many cases, along with just the colors representing the orientation, a rotated unit cell is also shown inside each grain that

corresponds to that particular orientation. The most popular, and yet, conventional methods of representing texture data, are however, pole figures and inverse pole figures. EBSD maps color code the data from the diffraction of back scattered electrons from an SEM, and can be used efficiently to represent texture data.

2.2.2.1 Pole-Figures

Crystallographic texture can be displayed by means of a **pole figure**, which is usually a stereographic projection of the crystal directions of each grain in the polycrystal. the crystal plane normals are known as *poles* and are plotted on the projection. An (hkl) pole figure displays the distribution of the $\{hkl\}$ poles in the polycrystalline sample. Individual orientation measurements, in case of Electron Back-Scatter Diffraction, are represented as points in the pole figure. These individual orientations (points), plotted together on the pole figure, give a glimpse into the texture of the polycrystal. If there are clusters of points in the pole figure, then it means that orientations are closer to those texture components that are represented by those clusters. The difference between pole figures of randomly oriented polycrystals, and polycrystals with preferred orientation is shown in Figure 2.6 for the (100) poles. In general, polycrystalline materials seldom have randomly oriented grains. More often than not, a preferred orientation exists that affects many properties of polycrystals, and introduces an anisotropy.

If we consider a plane in a crystal, then its orientation can be defined by its normal direction. If we draw a sphere, with its center on the plane, then the intersection of the normal direction and the sphere will be a point. This point is known as the pole. However, if we rotate the plane around its normal direction, then its normal doesn't change and hence the pole doesn't change. Therefore, two non-parallel planes are required to plot two poles on the sphere, and then if the object rotates, and one of the planes rotates with it, the change in relative positions of the poles will describe the new orientation completely.

A **stereographic projection**, is a technique in which we project the upper half of this sphere unto a plane that generally rests on the north pole, as shown in Fig. 2.7:

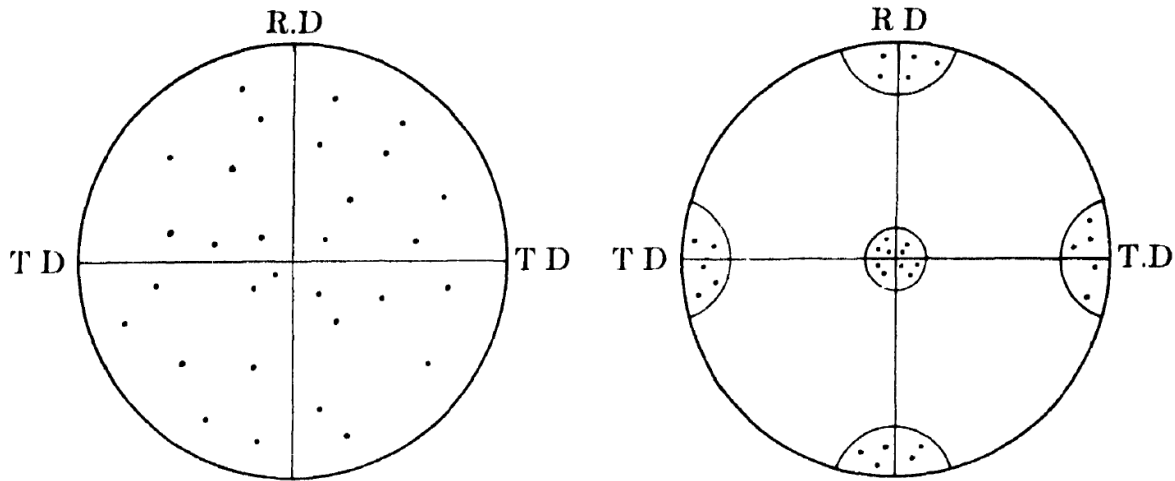


Figure 2.6: (100) pole figures for sheet material, illustrating (left) random orientation and (right) preferred orientation. RD (rolling direction) and TD (transverse direction) are reference directions in the plane of the sheet. Source: *Elements of X-Ray Diffraction*, B.D.Cullity, 1956

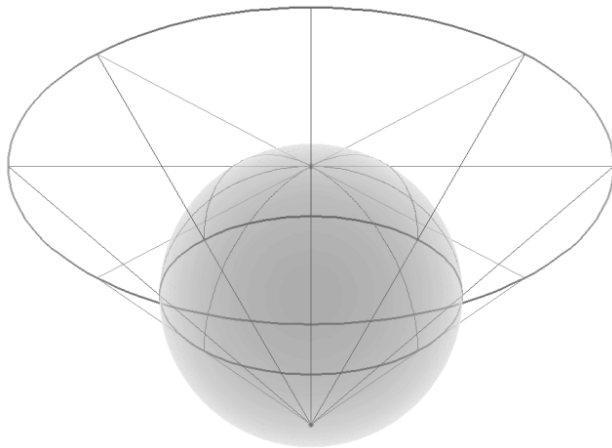


Figure 2.7: Stereographic projection sphere with the plane on the north pole. It also shows the projection of the south pole onto this plane. Source:Mark.Howison at English Wikipedia; https://en.wikipedia.org/wiki/Stereographic_projection

The poles, or points on this sphere also get projected unto this plane, and it results in a circle that represents the poles, and the plane traces. Plane traces are the intersections of the planes and the sphere. They appear as arcs. A Wulff net (Figure 2.8) is a circle with arcs corresponding to planes which share a common axis in the (x,y) plane. This plane is parallel to the equatorial plane of the sphere in Figure 2.7.

Wulff nets are vital in understanding and reading stereographic projections, even though nowa-

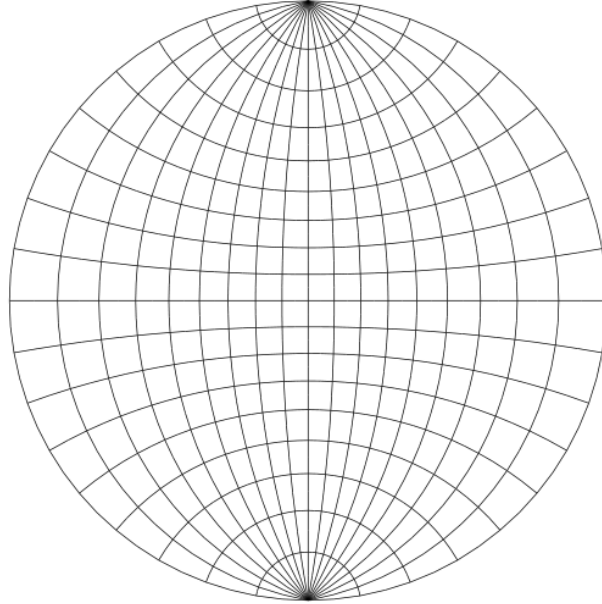


Figure 2.8: Wulff net or stereonet. It is used for plotting stereographic projection of poles and/or points manually

days we have computers and specialized softwares that can do it for us. We rotate the Wulff net so that the plane trace we want to study corresponds to an arc on the net. The pole or the point is situated on another arc, and the angular distance between these two arcs is then taken to be 90° .

To draw a pole figure, we choose a particular direction (usually the normal to one of the $\{100\}$ planes) and then plot that pole for all the crystals in a polycrystal, relative to a set of orthogonal directions, sometimes known as *rolling direction*, *transverse direction* and *rolling plane normal* (refer Figure 2.6).

If we are to plot these for a large number of crystals, then contour plots are preferred as opposed to individual points. To fully determine the texture in a polycrystal, the plot of two pole figures, each corresponding to a plane out of a pair of non parallel planes with different interplanar spacing.

2.2.2.2 Inverse Pole-Figures

Texture can also be represented by using an inverse pole figure. In this case, the axes of the sphere are aligned with any three crystal directions (generally $[100]$, $[010]$ and $[001]$) as opposed to the

global directions: normal, rolling and transverse, in the former case of Pole-figures. The points plotted in an inverse pole figure are crystal directions that are parallel to either the normal, or the transverse or the rolling direction in the sample. Thus, only certain types of textures can be visualized by an inverse pole-figure.

Due to symmetry considerations, however, a particular direction can be assigned any of the crystallographically symmetrical equivalent directions. This leads to the conceptualization of a fundamental or standard triangle as shown in the Fig. 2.9

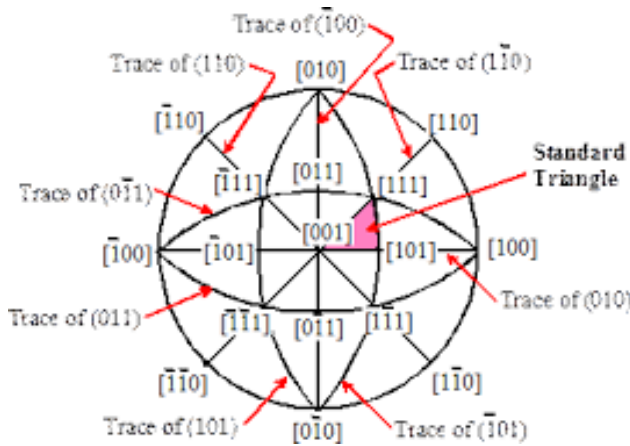


Figure 2.9: Standard Inverse pole figure for a cubic crystal. The $[100]$, $[010]$ and $[001]$ are parallel to the \mathbf{i} , \mathbf{j} , and \mathbf{k} respectively. Source: *Applied Mechanics of Solids* by A. F. Bower, Chapter 3

the three vertexes symbolize the $\langle 001 \rangle$, $\langle 110 \rangle$ and the $\langle 111 \rangle$ directions. The translation of this triangle along the crystal coordinates will give rise to the entire inverse pole figure. Thus, we can map all points into this fundamental triangle, and account for periodicity. Any texture component can thus be represented inside this triangle. For uniaxial tension tests of cubic crystals, tests should thus be run only for those cases where the loading direction is inside the standard triangle. In the case of a polycrystal with many grains, the distribution of points will give information about the orientation. If the distribution is uniform throughout, then we can infer that the crystals have a random uniform distribution of orientation. If clusters form, then the position of the clusters, especially their proximity to either vertexes, will relay information on the relative distribution of orientations, and also, the preferred orientation of the grains. A color coded fundamental triangle

can be used as a legend to accompany a color map of a polycrystal, and thus the texture can be effectively determined.

2.2.2.3 X-Ray Diffraction and Electron Back Scatter Diffraction

X-Ray Diffraction (XRD) is the preferred way of measuring orientations and textures in polycrystals on a macroscopic scale, while Electron Back Scatter Diffraction (EBSD) is the preferred way of obtaining the data at microscopic scales. XRD has large penetration depths of around $5\text{ }\mu\text{m}$ and a spatial resolution from a minimum of $25\text{ }\mu\text{m}$ to 1 mm . Tens of thousands of grains in a relatively larger area of about 10 mm^2 can be scanned by an XRD in one go, which makes it preferable for macroscopic samples. However, the spatial resolution is very poor and it is thereby unsuitable for microscopic samples. Also, Calculation of Orientation Distribution Function from pole figures can be really complex in case of XRD because of the large amount of grains scanned (which leads us to a pole figure with contours rather than points and clusters), and this can give rise to erroneous information. Plus, texture measurement by XRD needs about 30 to 60 minutes per pole figure, and about 3 to 4 pole figures are needed for a cubic symmetry (5 to 6 for lower symmetry crystals) if a distribution function is to be obtained.

On the other hand, EBSD has a rather small penetration depth (penetration depth is less because a beam of electrons can penetrate much less into a material than a beam of X-Ray photons) of around 20 nm which makes it surface sensitive. Moreover, if a Field Emission Scanning Electron Microscope is used to obtain EBSD data, then the spatial resolution is of the order of tens of nanometers which makes it superior to XRD for texture measurement of microscopic areas. Texture can be directly related to microstructure and measurement of grain sizes can be done too in case of an EBSD (an example of an EBSD map showing microstructure of a titanium sample, sourced from the work by Bahl et al^[2] is shown in Fig. 2.10) because all of these capabilities are built into an SEM and its accompanying software.

SEM also has depth resolution features which are extremely useful while analyzing surfaces. But EBSD may not work on heavily deformed materials or polymeric materials and needs greater

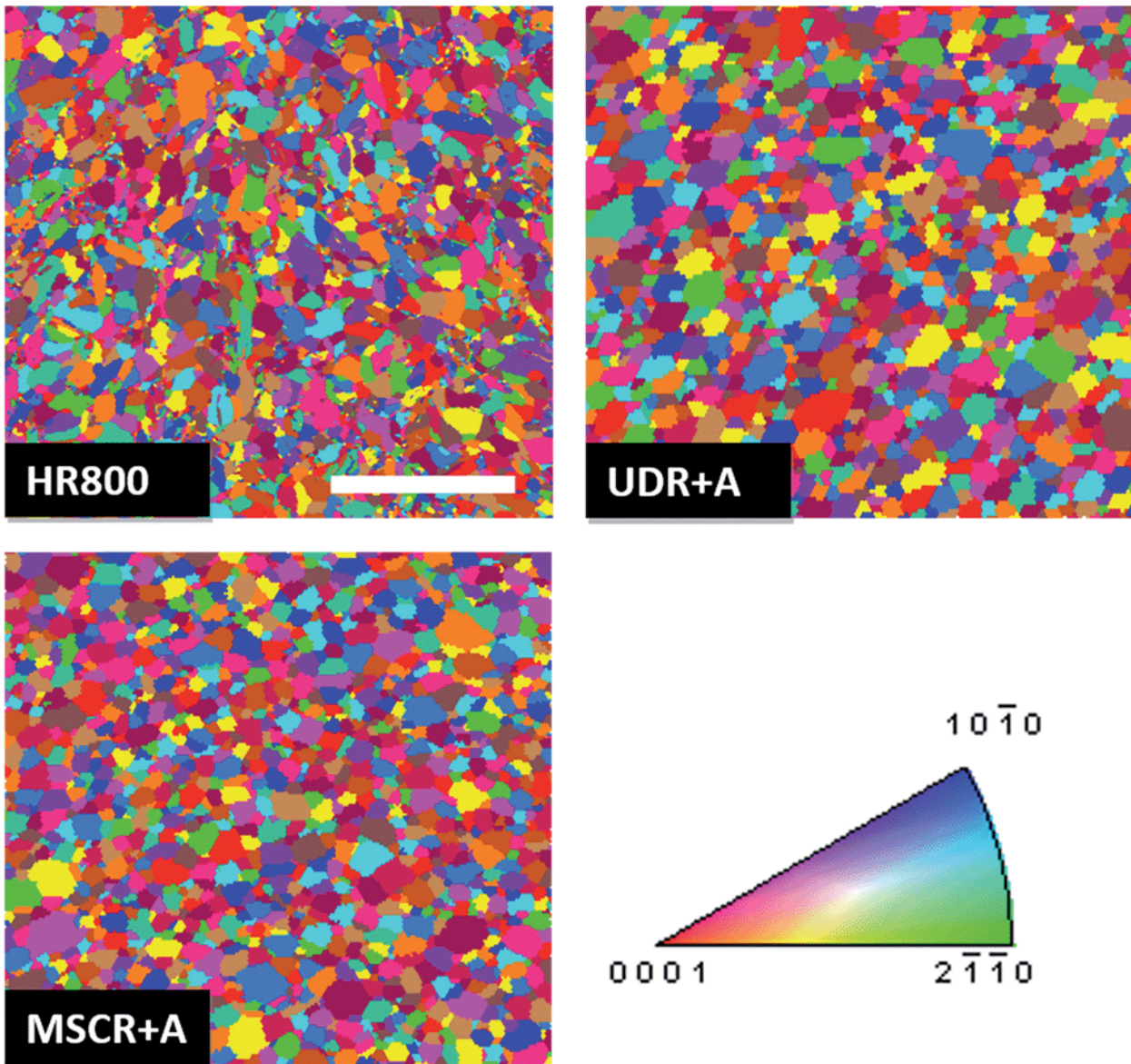


Figure 2.10: EBSD micrographs of hot-rolled and annealed titanium samples, along with the IPF color coded triangle for hexagonal close packed metals. Scale bar = 200 μm . This is for representation purposes only; for details about the labels in the micrographs, please be referred to the source: "The importance of crystallographic texture in the use of Titanium as an orthopedic biomaterial", by Bahl et al, J. RSC Advances, August 2014. the purpose of this figure is to demonstrate how an EBSD texture map may look like.

sample preparation times. In heavily deformed grains where a certain slip system is operating, an erroneous calculation might be made which may manifest as under-representation of a particular texture or plainly inaccurate calculations. However, acquisition time of data is pretty low because

crystal orientations can be measured at between 50 and 100 orientations per second. This gives us around 30 minutes to calculate data comparable to what an XRD measurement provides in 3 or 4 times that time. The dimensions of the oligocrystalline sample that was experimented upon at Sandia laboratories, as described in the paper by Lim et al is suitable for an EBSD measurement and thus they obtained EBSD data for texture for that sample In this work, their EBSD data has been used to virtually model and reproduce the actual oligocrystal in three dimensions by using certain functionalities provided by DAMASK such as conversion of tabulated data (Euler Angles or G matrix) from an ASCII format to a geometry file which can then be manipulated as regards mesh sizes and resolutions to make it comparable to the finite element simulations done at Sandia National Laboratories, Albuquerque, New Mexico.

CHAPTER 3

DISLOCATIONS

Crystals have long range order. Any irregularity in that order is known as a defect. Dislocations are one dimensional defects that are naturally present in a crystal as their formation is energetically favorable because they lower the free energy by increasing the entropy of the system. Dislocations can arise during crystallization from the liquid (or gaseous) state, when some atoms do not take their designated place in the lattice due to heterogeneous nucleation at preferred sites and directional solidification, as opposed to a homogeneous nucleation and planar solidification. Dislocations can arise if materials are strained or if a stress is applied, and there are inclusions, or point defects, or grain boundaries present. Many times grain boundaries themselves behave as the sources of dislocations. We will discuss more about other dislocation sources in section 3.2.2, and about what happens to the dislocations near the grain boundaries in section 3.2.3.

3.1 Edge and Screw Dislocations

Broadly, all dislocations or one dimensional irregularities in crystals can be categorized as having either edge character, screw character, or a mixture of both. The mixed type of dislocations form the majority of dislocations found in real crystals. To characterize a dislocation, a vector **b** is used, which is known as the **Burgers Vector** and it represents the magnitude and direction of the distortion in a lattice resulting from the presence of a dislocation in the lattice. The direction of the vector depends on the dislocation, and the crystallographic plane on which the dislocation exists. Generally, those planes have been observed to be the closest-packed planes. Although a **Burgers Loop** is generally drawn to determine the direction and magnitude of the burgers vector, mathematically, in a cubic crystal lattice, the magnitude can be given by:

$$||\mathbf{b}|| = \left(\frac{a}{2}\right) \times \sqrt{h^2 + k^2 + l^2} \quad (3.1)$$

where \mathbf{a} is the lattice parameter, $\|\mathbf{b}\|$ is the magnitude of the burgers vector \mathbf{b} and h,k,l are the components of \mathbf{b}

3.1.1 Edge Dislocations

These dislocations can be visualized as a one dimensional defect where there is an extra half-plane of atoms in the crystal, which distorts the nearby planes of atoms, as shown in the Figure 3.1 Such

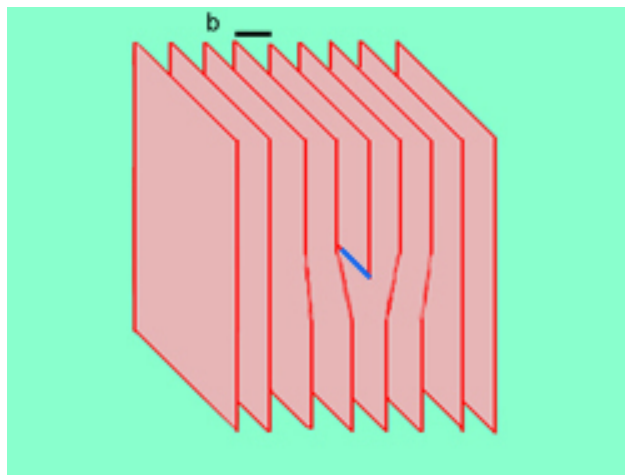


Figure 3.1: Visualization of an edge dislocation as an extra half plane of atoms in the lattice. The burgers vector(shown in black color) is perpendicular to the dislocation line(shown in blue)

a dislocation has a line direction that is shown in blue and the burgers vector which is perpendicular to the line direction that is shown in black in Figure 3.1. The burgers vector \mathbf{b} of an edge dislocation is always perpendicular to the edge dislocation line. Edge dislocations, upon application of external stress, can move, causing slip. The planes of slip are usually close packed planes, and the directions are the close packed directions too (parallel to \mathbf{b}). They cannot change slip planes and they move by continuous breaking and forming of bonds. They will continue moving if no obstructions exist until they emerge out on the surface, causing a slip line to be formed on the surface. The slip line height will be exactly equal to the magnitude of the burgers vector. If however, there exists another edge dislocation(s) of an opposite sign (imagine Fig. 3.1 upside down), then they cancel each other out. Without the presence of opposite dislocations, edge dislocations do not disappear from crystals. In this body of work, we have not expounded upon many more such properties of

edge dislocations, rather, we shall jump into the stresses experienced by dislocations, and stress fields associated with dislocations after a brief description of another type of dislocations, called screw dislocations.

3.1.2 Screw Dislocations

A screw dislocation is somewhat harder to imagine than an edge dislocation. If we cut a crystal along a plane, but only halfway through, and then apply a shear stress so that the two halves move in opposite direction, then the atoms arrange themselves in a helical fashion around the dislocation line, and we get a screw dislocation, as shown in Fig. 3.2.

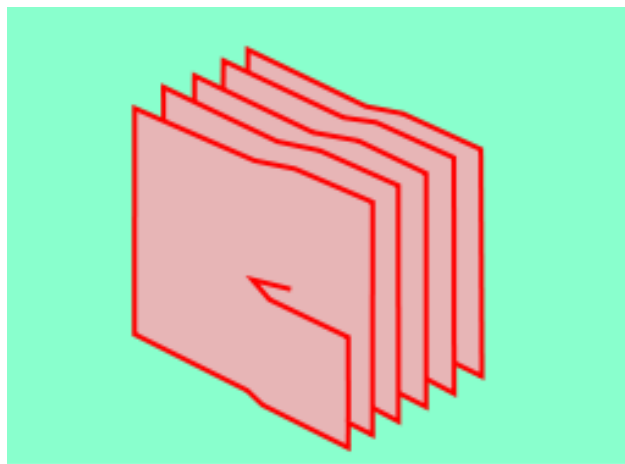


Figure 3.2: Visualization of a screw dislocation

Another simpler way of visualizing the screw dislocation has been shown in Figure 3.3. Atoms around a screw dislocation can trace a helical path around it, thus it is named as such. The pure screw dislocation line is always parallel to the Burgers vector, while the direction of dislocation motion during slip is perpendicular to the line direction. As usual, slip happens on close packed planes (usually the densest planes) along the closest packed directions because lower atomic spacing makes it easier for the dislocation to move at relatively lower stresses. Screw dislocations can however change slip planes, from one close packed plane to another (not necessarily parallel) by a phenomenon called cross-slip, owing to the fact that the Burgers vector is parallel to the dislocation

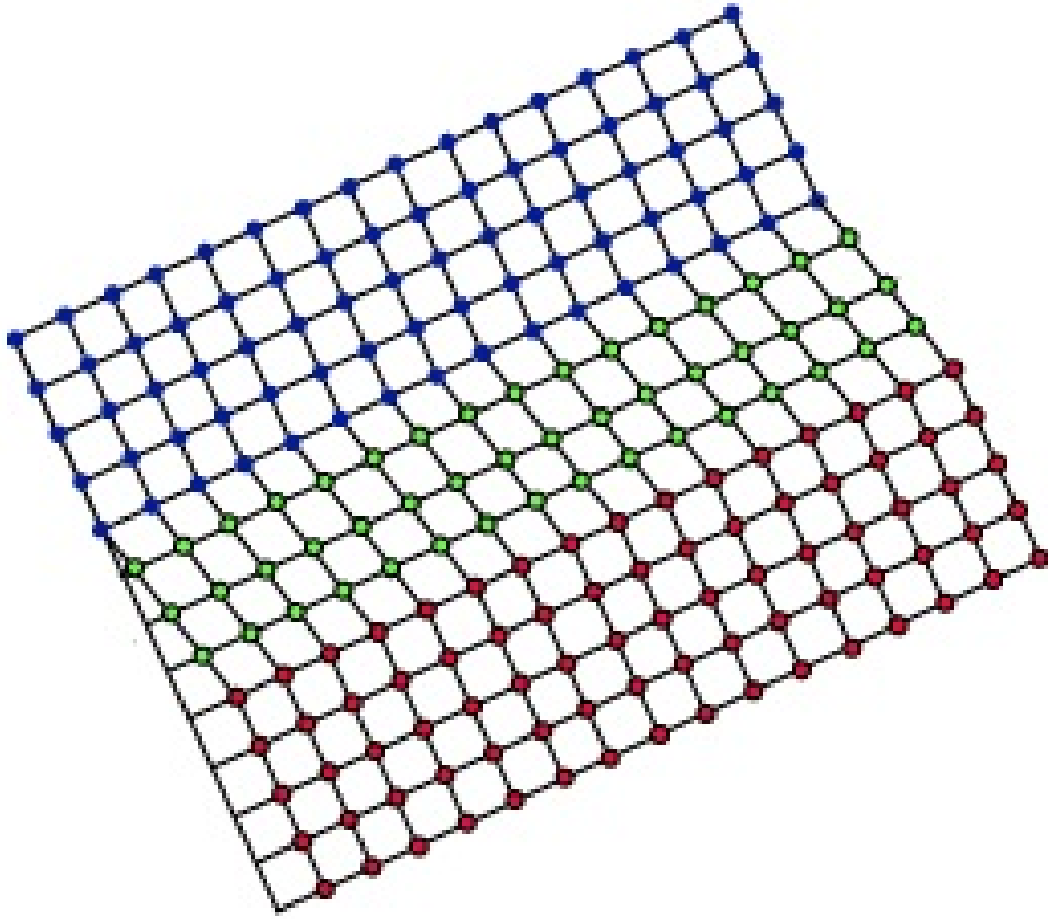


Figure 3.3: Visualization of a screw dislocation in a plane. The red atoms are already displaced, i.e, the dislocation has passed through; the blue ones are yet to be displaced while the green ones are in the process of moving and can be together called as the screw dislocation.

Source: <https://www.nde-ed.org/EducationResources/>

line. This has an effect on the interactions between dislocations of different characters, as we shall see in the next section.

At this point, it needs to be mentioned that many times, dislocations split into partial dislocations to circumvent obstacles, giving rise to stacking faults, and even more complicated interactions with other dislocations. An in-depth description of partial dislocation interactions and partial dislocation slip is out of the scope of this body of work. These partial dislocations may have either edge or screw character, or mixed, depending on their burgers vectors. Generally, when a dislocation with a burgers vector \mathbf{b} splits into two partials (named as **Shockley partials** if they are mobile

and cause stacking faults) with burgers vectors \mathbf{b}_1 and \mathbf{b}_2 , the split is favored energetically. if

$$|\mathbf{b}|^2 > |\mathbf{b}_1|^2 + |\mathbf{b}_2|^2 \quad (3.2)$$

Also, the components of the Shockley partials, must add up to the original vector that is being decomposed, i.e,

$$\mathbf{b} \rightarrow \mathbf{b}_1 + \mathbf{b}_2 \quad (3.3)$$

If the partial dislocations are sessile, they are termed as **Frank partials**. Shockley and Frank partials, upon interaction can form a stacking fault tetrahedron called as the **Thompson Tetrahedron**. Another type of partial dislocation interaction, when two Shockley partials combine to form a dislocation outside of the slip plane, is known as the **Lomer-Cottrell barrier**. As the name suggests, it is sessile and acts as a barrier to dislocation motion. Barriers to dislocation motion are one of the main causes for strain accumulation in grains and near grain boundaries and lead to strain hardening, as we shall see later.

3.2 Interaction of dislocations

Since at any given time in crystals, numerous dislocations are present, they are bound to interact. These interactions, under applied external stresses, lead to interesting consequences, such as deformation, strain hardening, formation of jogs, kinks, dislocation substructures, etc. Low angle grain boundaries are also a consequence of dislocation interactions, leading to local orientation changes.

3.2.1 Forces associated with dislocations

These aforementioned interesting consequences of dislocation interactions occur because all dislocations are associated with certain stress fields around them because the lattice in the vicinity of dislocations is strained. These stress fields interact with applied external stresses, and this causes either dislocation motion or shape changes depending on the magnitude, type, and direction of the applied forces. These stress fields also interact with the stresses associated with other dislocations

in the vicinity and either repel or attract the other dislocations. The stress tensor associated with an edge dislocation or the edge component of a mixed dislocation in isotropic materials with the dislocation line along the z direction, has the xx, yy, zz, xy and yx components, where xx, yy, and zz components are normal stresses whereas xy and yx are the shear stresses. the normal stresses are given by:

$$\sigma_{xx} = \frac{-Gby(3x^2 + y^2)}{2\pi(1-\nu)(x^2 + y^2)^2} \quad (3.4)$$

$$\sigma_{yy} = \frac{Gby(x^2 - y^2)}{2\pi(1-\nu)(x^2 + y^2)^2} \quad (3.5)$$

$$\sigma_{zz} = \nu(\sigma_{xx} + \sigma_{yy}) = \frac{-Gb\nu y}{\pi(1-\nu)(x^2 + y^2)^2} \quad (3.6)$$

$$\tau_{xy} = \tau_{yx} = \frac{Gbx(x^2 - y^2)}{2\pi(1-\nu)(x^2 + y^2)^2} \quad (3.7)$$

where G is the shear modulus, b is the magnitude of the Burger's vector, and ν is the poisson's ratio. Similarly, the elastic strain tensor for such an edge dislocation looks something like:

$$\boldsymbol{\varepsilon} = \begin{bmatrix} \varepsilon_{11} & \varepsilon_{12} & 0 \\ \varepsilon_{21} & \varepsilon_{22} & 0 \\ 0 & 0 & \varepsilon_{33} \end{bmatrix} \quad (3.8)$$

where ε_{xx} , ε_{yy} and ε_{zz} are normal strains while ε_{yx} and ε_{xy} are shear strains. These result in tension where the half plane is missing, and compression of the lattice where there is an extra half plane. When depicted pictorially, the stress contours look similar to those shown in Figure 3.4. It can thus be said that for two edge dislocations that if they are of opposite signs, they will attract each other to minimize overall strain and energy of the lattice, while if they are of the like sign, then they will repel each other.

Similarly, if we consider a screw dislocation with the dislocation line along the z direction, in an isotropic material, then by the inherent symmetry of the screw dislocation, the stresses will be only shear and exist only if there is a z component. Thus the stress equation in case of a screw dislocation are:

$$\sigma_{xz} = \sigma_{zx} = \frac{-Gby}{2\pi(x^2 + y^2)^2} \quad (3.9)$$

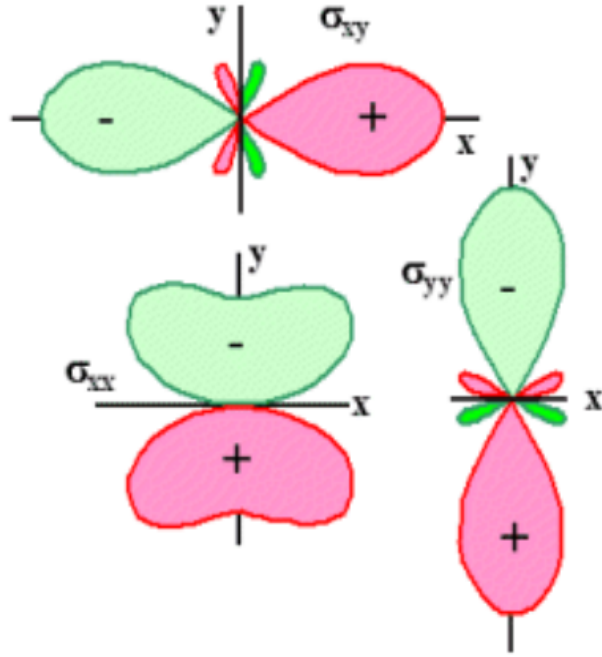


Figure 3.4: Visualization of stress fields around an edge dislocation. The dislocation line itself is perpendicular to the plane of the paper. σ_{zz} which is just the sum of σ_{xx} and σ_{yy} has not been shown. '+' represents tension, and '-' represents compression. Source: G.E.Dieter, Mechanical Metallurgy, 3rd Edition

$$\sigma_{yz} = \sigma_{zy} = \frac{-Gbx}{2\pi(x^2 + y^2)^2} \quad (3.10)$$

Thus there are no normal stresses, and shear exists only in the zx and zy planes. The strain tensor thus looks like:

$$\epsilon = \begin{bmatrix} 0 & 0 & \epsilon_{13} \\ 0 & 0 & \epsilon_{23} \\ \epsilon_{31} & \epsilon_{32} & 0 \end{bmatrix} \quad (3.11)$$

Figure 3.5 and 3.6 depict these stresses pictorially. MATLAB was used to generate the contours.

for calculating forces between two dislocations, 'dislocation 1' and 'dislocation 2', we use the

Peach-Koehler Equation:

$$\vec{F}_{(2)} = -\vec{\xi}_{(2)}x \left(\vec{b}_{(2)} \cdot \sigma_{ij}^{(1)} \right) \quad (3.12)$$

where $\vec{\xi}_{(2)}$ is the sense vector (or direction) of dislocation 2 at a particular point of interest on the dislocation line, $\vec{b}_{(2)}$ is the burger's vector of dislocation 2, and $\sigma_{ij}^{(1)}$ is the stress field of disloca-

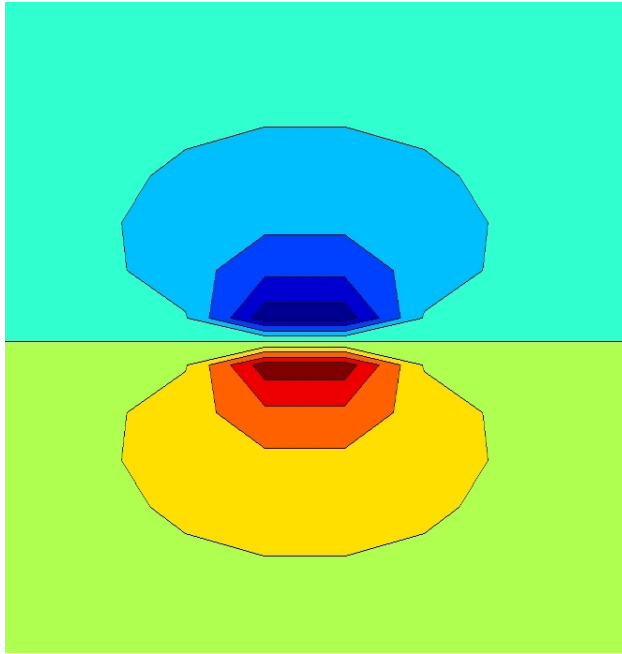


Figure 3.5: Visualization of stress contour (σ_{xz}) around a screw dislocation. the dislocation line is perpendicular to the plane of paper, x to the right and y to the top in the plane of the paper. the stress is always shear.

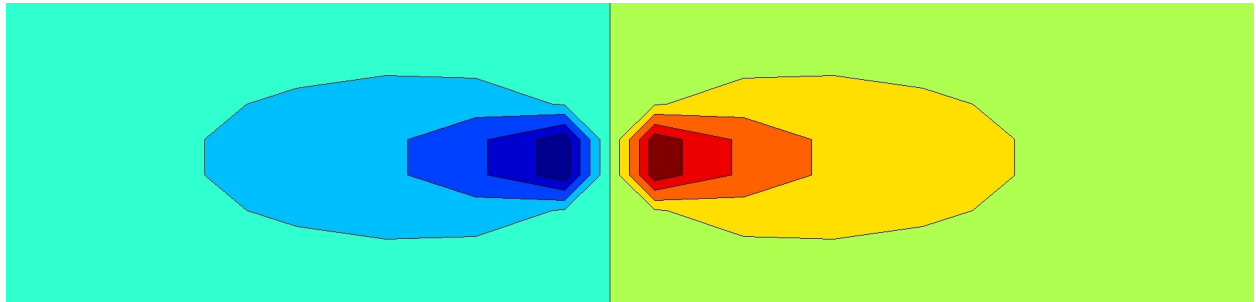


Figure 3.6: Visualization of stress contour (σ_{yz}) around a screw dislocation. the dislocation line is perpendicular to the plane of paper, x to the right and y to the top in the plane of the paper. the stress is always shear.

tion 1 at that point. a Peach-Koehler analysis of dislocation interaction arrives at conclusions that if two parallel edge dislocations are of opposite signs and on the same plane, they cancel each other out to form a perfect lattice; if they are of same signs, they repel each other and the stable distance between them is dictated by the equilibrium between repulsion and applied stress. If two opposite edges are not in the same plane, then the attractive forces would cause them to come together, but instead of total annihilation of dislocations, vacancies might be formed. Annihilation can occur at

higher temperatures when dislocation climb processes are more prevalent. If they are of like sign in two different planes, then they will repel each other, and most likely will remain at 45° to each other and at an equilibrium distance.

Similarly, when two screw dislocations, parallel, and on the same plane interact, then like screws (Right handed or left handed) will repel each other and unlike screws will attract. However, if the screws are orthogonal, then like screws will attract each other.

When edge dislocations on two orthogonal slip planes interact with each other and pass through each other, then each acquires a jog equal to the magnitude and direction of the burger's vector of the other. Thus both jogs are of edge character, and glissile. If jogs are formed on the same slip plane as the initial dislocations, then those jogs are called kinks. However, if they are extended dislocations, i.e, they are composed of two trailing partials, then a Lomer-Cottrell barrier is formed, and it is sessile.

When an edge and a screw dislocation on orthogonal slip planes pass through each other, edge jogs are created on both dislocations. These jogs slow down the motion of dislocations, thus causing strain buildup and hardening. The jog on the edge dislocation is in the direction of the screw dislocation, while the jog on the screw dislocation is in the direction of the burgers vector of the edge. When two screw dislocations on orthogonal planes pass through each other, they create jogs with edge character on both the screws, and these slow down the motion of the dislocations. These jogs can move only by climb or generate a row of vacancies or interstitials (point defects). Climb is non conservative and costs energy, and thus these jogs severely impede the screw dislocation movement.

3.2.2 Some sources of Dislocations

Such dislocation interactions, keep on getting more and more complicated with increase in dislocation density. With more and more non parallel dislocations on many different slip systems undergoing movement, many locks, barriers and jogs, along with vacancies and interstitials are formed which act as pinning points or barriers to dislocation motion, which can lead to build up of

strains. However, to account for these huge build up of plastic strains in crystals, there has to be a mechanism by which dislocations regenerate and multiply and thus lead to increase in dislocation density. Two of the important mechanisms are **Frank-Read source** and **multiple cross slip**.

3.2.2.1 Frank Read Source

If we consider a dislocation line on a slip plane pinned at its ends A and B by some kind of barrier or jog (maybe created as a result of dislocation interactions), as shown in Figure 3.7. if a shear stress τ is applied on this slip plane, then a force begins to act on the dislocation line as a result of that stress. This force is given by:

$$F = \tau \cdot \mathbf{b}x \quad (3.13)$$

This force is perpendicular to the line AB (shown in red in the figure 3.7) and tries to bend this line into a curve, simultaneously increasing the line length. this is opposed by the dislocation line tension which acts along the dislocation line but away from A and B with a magnitude of $G\mathbf{b}^2$ at each end. when the dislocation bends, the vertical component of this line tension acts opposite to the applied stress, and thus,

$$\begin{aligned} F &= \tau \cdot \mathbf{b}x = 2G\mathbf{b}^2 \\ \implies \tau &= \frac{2G\mathbf{b}}{x} \end{aligned} \quad (3.14)$$

Equation 3.14 gives the amount of stress that is at least required to generate a dislocation from a Frank-Read source such as that shown in Figure 3.7. If the stress increases further, then the dislocation line will continue to bend more and more until it reaches an equilibrium position (the indigo colored semicircle in the figure) where all of the line tension is now utilized against the applied stress. If the applied stress still increases, then the dislocation spontaneously expands and spirals (as shown by the blue and then the green curve) around the pinning points A and B. It finally reaches a point where the two segments spiraling about A and B collide with each other. Since they have opposite line sense, they cancel each other out, and a dislocation loop (shown in yellow) is formed which steadily moves away from the center. In its wake, it leaves a new dislocation which follows the same steps as before, under continued stress, and the multiplication continues.

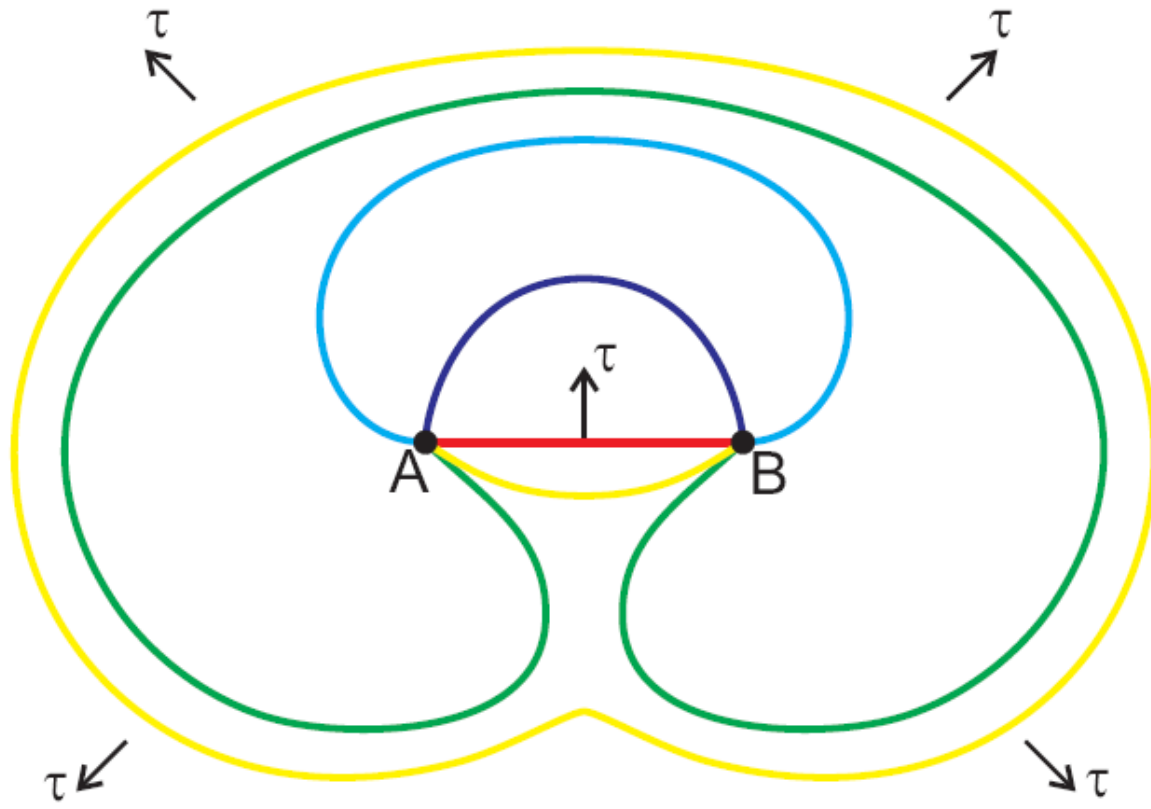


Figure 3.7: Visualization of stages of Dislocation multiplication by the Frank-Read mechanism under shear on a slip plane. A and B are the pinning points, and τ is the applied shear stress.

Source: Jntf - Own work, CC BY-SA 3.0,
<https://commons.wikimedia.org/w/index.php?curid=7501825>

3.2.2.2 Multiple Cross slip

Figure 3.8 shows a schematic of the multiple cross slip process which leads to two edge dislocations AC and BD on the slip plane $(1\bar{1}1)$. Only screw dislocations or screw components of mixed dislocations can cross slip, for to undergo cross slip, the burgers vector needs to be parallel to the dislocation line. Applied stress can be either parallel or perpendicular to \mathbf{b} . The screw component of the mixed dislocation line cross slips first from the (111) slip plane onto the $(1\bar{1}1)$ slip plane, and then once again cross slips back onto the (111) plane. The two segments Ac and BD with edge character now are pinned at their ends. These then start behaving like Frank-Read sources and multiply under applied shear stress on the slip plane $(1\bar{1}1)$.

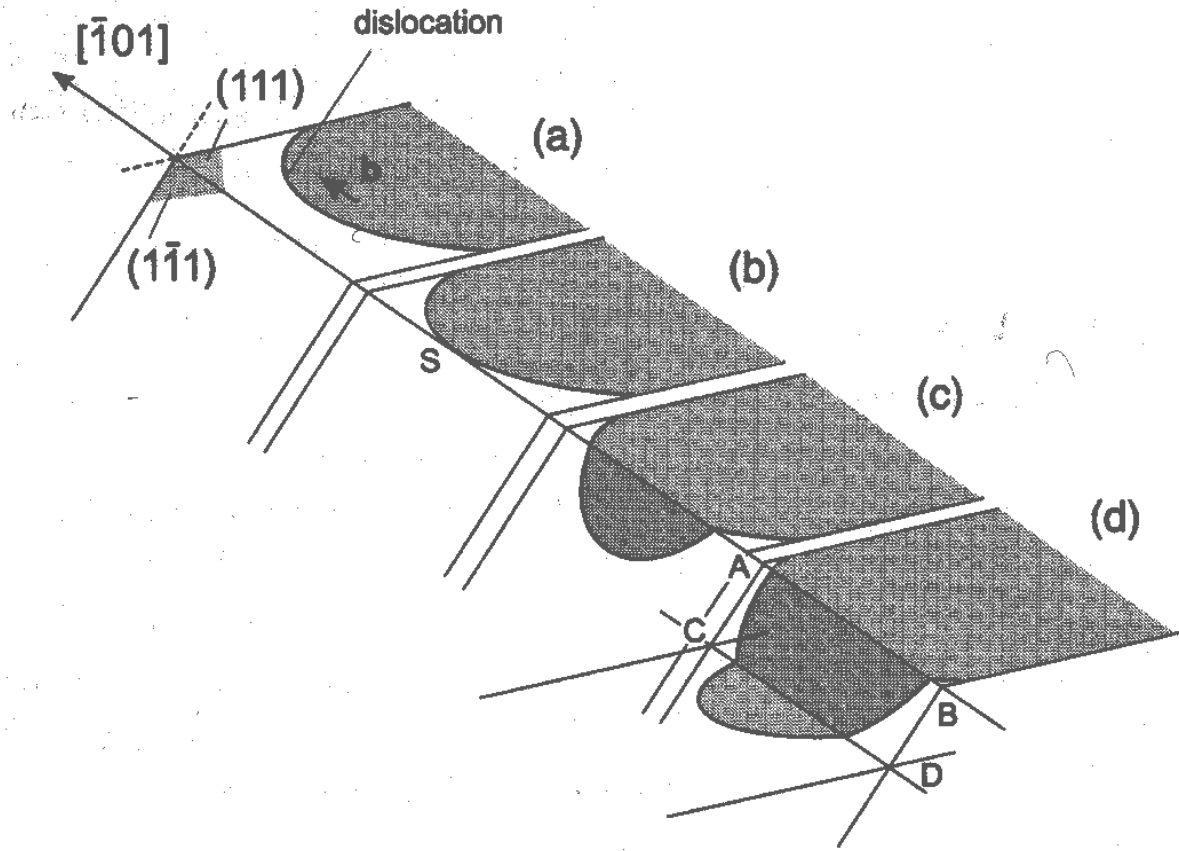


Figure 3.8: Visualization of stages of multiple cross slip of the screw component of a mixed dislocation. The planes $(1\bar{1}1)$ are the family of slip planes

3.2.3 Dislocations near Grain boundaries

Grain Boundaries are two dimensional entities that can be visualized as an array of dislocations which mark the transition of one grain from another. We generally refer to High-Angle Grain Boundaries here, i.e., Grain Boundaries between two grains with more than $5-10^\circ$ misorientation. The Grain boundaries act as sources of dislocations because they have a higher energy than the bulk of the grain, have more randomness than order. This causes them to be preferred sites for vacancy nucleation, segregation of phases, inclusions, etc which can lead to dislocation multiplication and/or generation. Also they already have a high mismatch which can begin extending into the grain's bulk, forming dislocations. However, the most important thing about grain boundaries

is perhaps the way dislocations behave near them, causing grain boundary strengthening. This means that Grain boundaries have much higher strain concentrations than the bulk of the grain. In this body of work, our focus has been to determine if spectral solution strategies of computation gives us grain boundary strain concentrations closer to what we found experimentally, where the CPFEM model could not. In this section we discuss what the cause of higher strain concentrations at grain boundaries is.

Grain Boundaries act as barriers to dislocation motion owing to randomness, mismatch, and a disruption in the long range order. The lattice structure of the grain on the other side is different from the current grain the dislocation is in and it costs energy to change directions and slip planes. Since dislocation motion, or slip is one of the primary causes of plastic deformation, impeding this motion will cause an increase in the yield strength, i.e, cause delay in plastic deformation. One by one, the dislocations start coming to grain boundaries from the bulk of the grain, and begin piling up. Since dislocations of opposite signs cancel each other out, the pile ups will be caused by dislocations of like signs. This creates repulsion between the dislocations near the grain boundaries, which is magnified by the close proximity of the dislocations to each other near the grain boundaries, and thus causes higher strain concentrations than in the bulk. Eventually, this total repulsive force becomes enough for dislocations to diffuse through to the adjacent grain, and continue deformation. Thus, if we have smaller grain sizes, then the amount of pile up is not enough to overcome the threshold and start dislocation diffusion. In other words, smaller grain sizes imply higher number of grain boundaries and hence greater obstruction to dislocation motion, and thus higher yield strength. The relationship of yield stress and grain size is given by the ***Hall-Petch Relationship***:

$$\sigma_y = \sigma_0 + \frac{K_y}{\sqrt{d}} \quad (3.15)$$

where σ_y is the yield stress, σ_0 denotes the resistance to slip, K_y is a material constant known as the *strengthening coefficient* and d is the diameter of the grain (average grain diameter). The

strengthening coefficient is given by:

$$K_y = \sqrt{\frac{8G\mathbf{b}\sigma_c}{\pi(1-\nu)}} \quad (3.16)$$

where σ_c is the critical stress. The above equations are however, derived for cases where the applied stress is tensile and uniaxial, the same type as has been considered in this body of work. Critical stresses are addressed in the next chapter.

CHAPTER 4

STRESSES AND STRAINS IN CRYSTALS

No discussion about polycrystalline aggregates under tension would be complete if we do not discuss about the different stresses and strains that are measured to quantitatively and qualitatively characterize the deformation behavior. It is known from experience that if sufficient external load is applied, all materials can be deformed. However, up until a certain amount of load is applied, solids generally recover their original dimensions. This is called *elastic* behavior. Beyond this certain amount of limiting load, known as the *elastic limit* of the substance, the solid experiences a permanent deformation, slip being one of whose most studied mechanisms. This behavior is termed as *plastic* behavior. We shall delve deeper into this, as well as the stress versus strain graph for materials in the upcoming sections.

4.1 Engineering and Instantaneous stress and strain

Engineering stress or *average stress* is defined as the Force applied to a body, per unit area of cross section. This is just an average value of the stress over the entire body, and assumes uniform distribution of stresses in the cross section. Mathematically, if we consider a cylinder of cross sectional area A , under uniaxial tension, with the force applied being F , then the average stress s is expressed as:

$$s = \frac{F}{A} \quad (4.1)$$

where we have considered a uniform distribution of stress along the entire cross-section. If we do not consider this uniformity, and take into account stress localization at certain areas in the body, and use the instantaneous area of cross section, then the value we get is called *instantaneous* or *true* stress (σ), and it is expressed as:

$$\sigma = \frac{F}{\int dA} \quad (4.2)$$

where A is the instantaneous cross sectional area. The units of stress (both engineering and instantaneous) are usually *pascals* or *mega-* or *giga-* pascals.

Similarly, Engineering strain is defined as the change in dimension over original dimension of the solid. In our one dimensional case of uniaxial tension, average or engineering strain, e , is given by:

$$e = \frac{\Delta L}{L} = \frac{L - L_0}{L_0} \quad (4.3)$$

where ΔL is the Change in length, calculated as $L - L_0$, L being the new length after deformation and L_0 being the initial dimension. Instantaneous strain, ε , however, is defined as the change in the dimension divided by the instantaneous value of the dimension. Mathematically,

$$\varepsilon = \int_{L_0}^{L_f} \frac{dL}{L} = \ln \frac{L_f}{L_0} = \ln(e + 1) \quad (4.4)$$

where L_f is the final length, L_0 is the initial length, and L is the instantaneous length; and e is the engineering strain. This is also known as the *true* strain. Under the true elastic limit, both strains give similar values (owing to the very small stresses involved), however the true strain is more important in plastic deformation, especially in metals. Strain is a dimensionless quantity.

Up until now, we have considered only normal stresses and strains. However, shear stresses and strains can also be defined in similar ways. Engineering shear stress is given by:

$$t = \frac{F}{A} \sin \theta \quad (4.5)$$

where θ is the angle between the applied force F and the normal to the cross-section. Instantaneous shear stress is given by:

$$\tau = \frac{F}{\int dA} \sin \theta \quad (4.6)$$

Similarly, a shear strain can be expressed as:

$$\gamma = \tan \theta \quad (4.7)$$

where θ is the angular displacement of the original dimension.

4.2 Flow curve and Yielding criteria

4.2.1 The Flow Curve

A flow curve depicts plastic flow when a solid is deformed and is generally a stress-strain curve obtained from a simple tension test where a sample is uniaxially loaded. The true stress σ and the true strain ϵ are plotted. A typical flow curve for a ductile solid is shown in Figure 4.1.

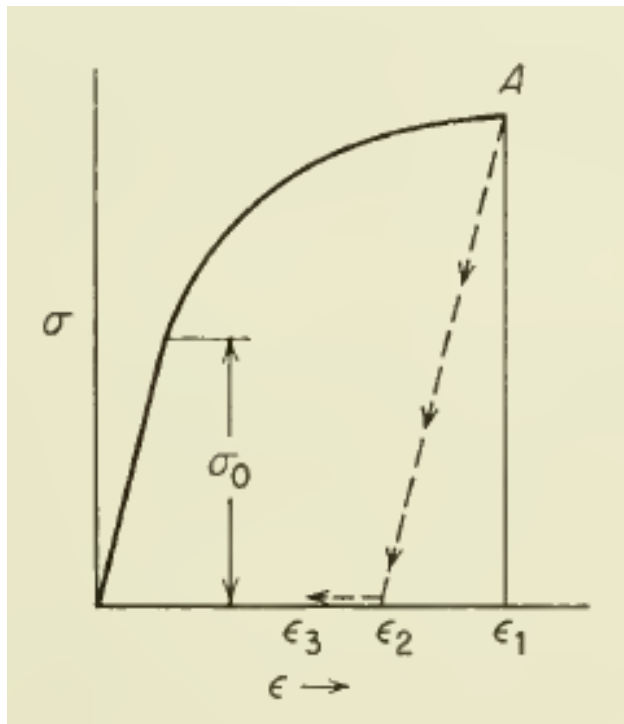


Figure 4.1: True stress vs true strain for a ductile solid. σ_0 is the yield stress, ' $\epsilon_1 - \epsilon_2$ ' is the *recoverable elastic* strain, and ' $\epsilon_2 - \epsilon_3$ ' is the *anelastic* behavior which is mostly neglected in mathematical theories of plasticity. Source: *Mechanical Metallurgy by George.E.Dieter, Chapter-3, Section 3-2*

At the beginning, the material deforms elastically with increasing stress, and the relationship between stress and strain is linear. Thus, in the elastic region, stress is directly proportional to strain. This is called as the *Hooke's Law*. The ratio of σ and ϵ in the elastic region thus gives us

the value of the *Modulus of Elasticity*, E .

$$\begin{aligned}\sigma &\propto \varepsilon \\ \Rightarrow \frac{\sigma}{\varepsilon} &= E\end{aligned}\tag{4.8}$$

If instead of normal stresses, one would apply shear, then the modulus is called as *shear modulus* and is denoted by G . Thus,

$$\frac{\tau}{\gamma} = G\tag{4.9}$$

where τ is the shear stress, and γ is the shear strain.

After σ_0 , the yield stress, has been exceeded, Hooke's law is no longer followed and the material deforms plastically. As is evident from Figure 4.1, stresses higher than yield stress is required to cause similar increases in strain as compared to the elastic region. This is a consequence of *strain hardening*. At point A, when the load is suddenly released, the strain drops almost immediately from ε_1 to ε_2 , by an amount equal to σ/E . This change in strain is called *recoverable elastic strain*. The remaining strain is plastic. But not all plastic strain is permanent. Some relaxation of plastic strain from ε_2 to ε_3 occurs, depending on the temperature, or the material involved, and is known as *anelasticity*. If however, no unloading is done at A, and stress is continuously increased, then soon, necking will occur and ultimately fracture. A power equation of the form

$$\sigma = K\varepsilon^n\tag{4.10}$$

can be used to describe the plastic region until necking begins. K is the stress at $\varepsilon = 1$ and n is the strain hardening coefficient which is basically found from the slope of a log-log plot of equation 4.10.

4.2.2 Yielding criteria

For plastic deformation to happen, the material has to yield. Thus, the stress and strain must go beyond the yield point. Yielding criteria help us in devising ways to predict when a material will yield, and thus, when plastic deformation will begin. In the case of uniaxial tension (or

compression), plastic deformation or plastic flow begins when the applied stress reaches a value of σ_0 or the yield stress. For the general case, yielding must be therefore related to the principal stresses, or some combination of them. When the basis of a stress tensor is changed in such a way that the shear components become zero, the leading diagonal is the only one with non zero values. Those three stresses are the principal stresses σ_1, σ_2 and σ_3 . Mathematically,

$$\begin{aligned}\sigma_1 &= \frac{J_1}{3} + \frac{2}{3} \left(\sqrt{J_1^2 - 3J_2} \right) \cos \varphi \\ \sigma_2 &= \frac{J_1}{3} + \frac{2}{3} \left(\sqrt{J_1^2 - 3J_2} \right) \cos \left(\varphi - \frac{2\pi}{3} \right) \\ \sigma_3 &= \frac{J_1}{3} + \frac{2}{3} \left(\sqrt{J_1^2 - 3J_2} \right) \cos \left(\varphi - \frac{4\pi}{3} \right)\end{aligned}\quad (4.11)$$

where

$$\begin{aligned}\varphi &= \frac{1}{3} \cos^{-1} \left(\frac{2J_1^3 - 9J_1J_2 + 27J_3}{2(J_1^2 - 3J_2)^{3/2}} \right) \\ J_1 &= \sigma_{11} + \sigma_{22} + \sigma_{33} \\ J_2 &= \sigma_{11}\sigma_{22} + \sigma_{22}\sigma_{33} + \sigma_{33}\sigma_{11} - \sigma_{12}^2 - \sigma_{23}^2 - \sigma_{31}^2 \\ J_3 &= \sigma_{11}\sigma_{22}\sigma_{33} - \sigma_{11}\sigma_{23}^2 - \sigma_{22}\sigma_{31}^2 - \sigma_{33}\sigma_{12}^2 + 2\sigma_{12}\sigma_{23}\sigma_{31}\end{aligned}\quad (4.12)$$

where J_1, J_2 and J_3 are known as *stress invariants* because their values are independent of the coordinate system in which stress is expressed, and σ_{ij} are the components of the applied stress tensor. Because of this mathematical complexity, most yielding criteria equations are essentially empirically derived. Two of the most widely used yield criteria are the **Tresca** and the **Von-Mises** yield criteria. The Tresca criterion is also known as the Maximum Shear Stress theory, and it postulates that yielding will occur only when the maximum shear stress experienced by a solid will reach a critical value which is equal to the shear yield stress in any given uniaxial tension test.

Thus, the maximum shear stress is given by

$$\tau_{max} = \frac{\sigma_1 - \sigma_3}{2} \quad (4.13)$$

For the case of uniaxial tension, $\sigma_1 = \sigma_0$, and both σ_2 and σ_3 are zero (uniaxial means there is stress in only one direction). Thereby,

$$\tau_{max} = \frac{\sigma_0}{2} \quad (4.14)$$

where σ_0 is the yield stress of the material under simple uniaxial tension. Thus, from equations 4.13 and 4.14,

$$\sigma_1 - \sigma_3 = \sigma_0 \quad (4.15)$$

Since hydrostatic components do not necessarily cause deformation in in-compressible materials, we consider only the deviator components of applied stress. Thus, equation 4.15 becomes

$$\sigma'_1 - \sigma'_3 = 2k \quad (4.16)$$

where σ'_1 and σ'_3 are the deviator components of the principal stresses, and k is the stress at which, under torsion, yielding occurs, so it is the shear yield stress. However, as discussed by Prager Hodge et al^[3], such simple mathematical relations cannot be satisfactorily applied to many plasticity problems, and the general form of the Tresca criterion is then used:

$$4J_2^3 - 27J_3^2 - 36k^2J_2^2 + 96k^4J_2 - 64k^6 = 0 \quad (4.17)$$

The complexity of this general equation is overcome by another yield criterion, known as the Von Mises yield criterion. This is also known as the Distortion energy criterion. According to this criterion,

$$\sigma_0 = \frac{1}{\sqrt{2}} \left[(\sigma_1 - \sigma_2)^2 + (\sigma_2 - \sigma_3)^2 + (\sigma_3 - \sigma_1)^2 \right]^{\frac{1}{2}} \quad (4.18)$$

Thus, yielding occurs when the R.H.S of equation 4.18 exceeds σ_0 which is the yield stress under uniaxial tension.

4.3 stresses and strains in single-crystals and polycrystals

It is evident that the effects of stresses and strains and how the materials deform, are different for single and polycrystals as the former do not have grain boundaries. This section describes these differences, and the difference in strain hardening as well, in single and poly-crystals.

4.3.1 Plastic Deformation in Single Crystals

Slip by movement of dislocations is the predominant mechanism of deformation. How much does a single crystal slip, depends on the amount of shear produced by the externally applied load, the crystal orientation (because slip occurs on preferred planes and directions) with respect to the loads, and the geometry of the crystal. Slip, or deformation, would begin when the shear stress on the preferred plane in the preferred direction (It is generally the closest packed plane and closest packed direction on that plane, because the less the atoms have to move to move the dislocations, the easier it is for slip to happen), just exceeds a certain threshold value, known as the *critical resolved shear stress*. If we would plot an ordinary stress-strain curve, then the yield stress would be equal to the critical resolved shear stress.

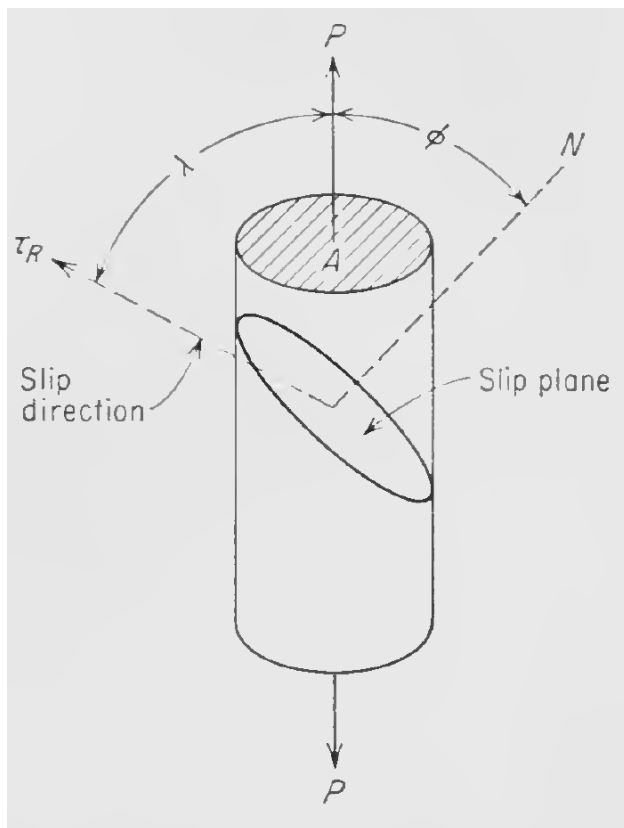


Figure 4.2: Resolved shear stress in a single crystal. Source: *Mechanical Metallurgy* by George E. Dieter, Chapter-4, Section 4-7; E. Schimd, Z. Elektrochem., vol. 37, p. 447, 1931

Let us consider Figure 4.2. The cylinder shown is a single crystal, with cross-sectional area A .

ϕ is the angle between the slip plane normal, and the tensile axis, whereas λ is the angle between the slip direction and the tensile axis. As is evident, the component of stress acting along the slip direction is $P \cos \lambda$ where P is the applied uniaxial tensile load. Similarly, the area of the slip plane shown is given by $A / \cos \phi$. Therefore, the resolved shear stress is given as:

$$\tau_R = \frac{P \cos \phi}{A / (\cos \lambda)} = \frac{P}{A} \cos \phi \cos \lambda. \quad (4.19)$$

where $\cos \phi \cos \lambda$ is known as the *Schmid factor*. As can be seen, this will reach a maximum value for most cases when the schmid factor has a value of 0.5. The resolved shear stress is thus dependent on the orientation of the crystal, its slip planes and slip directions. It is also dependent, obviously, on the dislocation density in the single crystal and other defects present that interact with the dislocations. However, the critical resolved shear stress is the minimum shear required to start or cause slip in a single crystal.

After slip has begun, the stress required to continue the deformation keeps increasing with increase in strain. This phenomenon, wherein more stress is required to cause slip because of prior plastic deformation, is known as *strain hardening*. One of the most widely accepted reasons of why this happens is that with increase in plastic deformation, more and more dislocations are produced (from previously existing ones by many mechanisms, one of them being the Frank-Read mechanism). This causes the dislocations to interact with each other and form sessile jogs that obstruct dislocation motion, or interact with vacancies, or inclusions present that also impede their movement. Many times, Lomer-Cottrell locks are produced which also contribute to a reduced mobility of the dislocations. Many times, the dislocations pile up near obstacles and since these pile ups mostly consist of similar dislocations, they repel each other which gives rise to a *back stress*. This back stress opposes the applied stress. Thus, when one reverses the stress direction, the back stress already developed now acts in the same direction as the applied load and causes the yield stress to decrease. Such a phenomenon is termed as *Bauschinger effect*.

Apart from the back stress, sometimes, at large deformations, a [forest] of dislocations moving on one slip plane, might intersect with another forest of dislocation on another active slip plane!

However, such interactions occur over distances of less than $5 - 10a$ where a is the interatomic distance. They are thus temperature dependent; because thermal fluctuations at finite temperatures can overcome the hardening effect due to dislocation forest interactions. But dislocation pile-up induced back stress and the hardening caused due to that is not temperature dependent and is neither strain rate dependent because they occur over long distances! In work done by Basinski et al^[4], temperature and strain rate dependence can be used to determine which mechanism (the back stress or the dislocation interaction) is more prevalent, or is the main contributor to strain hardening in single crystals. in many single crystals, especially with fcc lattice structure, and if the material has high stacking-fault energy, then rates of strain hardening are expected to be lower as cross slip becomes prevalent.

4.3.2 Plastic Deformation in Polycrystals

Deformation in polycrystalline aggregates is different and more complex than that in single crystals because of the presence of grain boundaries, sub-grain boundaries, preferred orientations, preferential dispersion of second phases, etc. Grain boundaries are arguably the most important of these.

Ordinary high-angle grain boundaries have a rather high surface energy, and thus act as preferred sites for diffusion, phase transformation (nucleation of other phases) or segregation, and precipitate aggregation. However, depending on the temperature range in which the plastic deformation is taking place, the purity of the metal, and the strain rate, grain boundaries can either strengthen the solid or weaken it.

At room temperatures, and up to half the melting point of the ductile material with a relatively high strain rate, grain boundaries significantly increase the strain hardening by acting as barriers to dislocation motion. However, under *creep* conditions, i.e, higher temperatures and slow strain rates, most of the deformation happens mostly at grain boundaries. This localization causes effects such as grain boundary sliding and grain boundary migration which leads to fracture which also takes place at the grain boundaries. The temperature at which this happens, i.e, grain boundaries become weaker than the bulk of the grain, is called ***equicohesive temperature***. But below this

temperature, Grain boundaries will always be stronger than the grain and will always have a higher strain than the bulk because grain boundaries are barriers to slip, and introduce discontinuity in the lattice that the dislocations cannot overcome. This also causes multiple slip systems to activate which causes even further complexities in slip and leads to formation of more barriers to slip.

Dislocation pile ups occur in polycrystalline materials at the grain boundary, and not just at obstacles (as is the case with single crystals). However, due to presence of many slip planes in fcc or bcc metals, dislocation pile ups are significant only at lesser strains, but they are more effective in the case of hcp metals because hcp lattice has only one easy slip plane {0001}.

However, just dislocation pile ups at grain boundaries, misorientation, and slip on multiple planes estimate strain hardening of polycrystals well below the experimental values. To get a better estimate, grain size effects have to be taken into consideration because the yield stress depends on the grain sizes as described by the Hall Petch equation (equation 3.15). Apart from that, presence of low angle grain boundaries, or sub-grain boundaries inside individual grains results in a very significant increase in strength with not too much reduction in ductility. Also, there are processes of solid solution hardening, strengthening due to the presence of second phase particles and hardening due to interaction of dislocations and point defects which result in overall deformation hardening of polycrystalline aggregates and affect plasticity. However, in our work we have considered only a pure, single phased fcc polycrystal. Each of the grains have their own values of critical resolved shear stresses, and thus deform at different stresses. But after deformation has begun, and extensive cold work has been done, the polycrystals develop a preferred texture. Grains rotate under stress, to make their slip planes parallel, and thus grain rotation is one of the effects of polycrystalline plastic deformation!

CHAPTER 5

CONSTITUTIVE LAWS

Constitutive laws are the established laws for elastic and plastic deformations, represented as a set of fundamental equations that define, describe, and parameterize the microstructure, dynamics of elastic and plastic deformation, and establish the constitution of the mathematical model that is solved to obtain the results of the simulations.

5.1 Phenomenological Power Law for FCC crystals

In this case, a *phenomenological power law* constitutive model for an *fcc* structure has been considered, that introduces the plastic flow dynamics into the computation. This makes the algorithm calculate the plastic shear strain rate $\dot{\gamma}^\alpha$ of each of the twelve slip systems $\alpha = \{111\}\langle\bar{1}10\rangle$ for a face centered cubic lattice, as a function of the *second Piola–Kirchhoff stress* \mathbf{S} .

The governing equations in this Phenomenological power law model (in no particular order) for an fcc structure are outlined below:

The deformation gradient \mathbf{F} , when deformation occurs from a reference configuration to a resulting one, can be separated into elastic and plastic components:

$$\mathbf{F} = \mathbf{F}^e \mathbf{F}^p \Rightarrow \mathbf{F}^e = \mathbf{F} \mathbf{F}^{p-1} \quad (5.1)$$

where \mathbf{F}^e is the elastic and \mathbf{F}^p is the plastic component. Also, since we are interested in the plastic part, we can express the elastic component in terms of the plastic component as shown above. the deformation gradients are tensorial quantities.

The elastic Green strain tensor \mathbf{E}^e is expressed as:

$$\mathbf{E}^e = \frac{1}{2}(\mathbf{F}^{eT} \mathbf{F}^e - \mathbf{I}) \quad (5.2)$$

where \mathbf{F}^{eT} is the transpose of the elastic deformation gradient, and \mathbf{I} is the identity matrix.

The Second Piola–Kirchhoff stress tensor $[S]$ is given by:

$$\mathbf{S} = [C]\mathbf{E}^e \quad (5.3)$$

where $[C]$ is the elasticity tensor, an anisotropic elastic stiffness tensor that relates the elastic deformation gradient to the second Piola–Kirchhoff stress.

The rate of change of the plastic part of the deformation gradient is given by:

$$\dot{\mathbf{F}}^p = \mathbf{L}^p \mathbf{F}^p \quad (5.4)$$

where \mathbf{L}^p is the plastic flow velocity gradient given by:

$$\mathbf{L}^p = \sum_{\alpha=1}^N \dot{\gamma}^\alpha P^\alpha \quad (5.5)$$

where α is the slip system, N is the number of slip systems, $\dot{\gamma}^\alpha$ is the shear rate on the slip system α , and P^α is given by:

$$P^\alpha = m^\alpha \otimes n^\alpha \quad (5.6)$$

where m^α is the slip direction and n^α is the slip plane normal for that slip-system.

The shear rate is given by the equation:

$$\dot{\gamma}^\alpha = \dot{\gamma}_0 \left| \frac{\tau^\alpha}{g^\alpha} \right|^{1/n} \operatorname{sgn}(\tau^\alpha) \quad (5.7)$$

where $\dot{\gamma}_0$ is a constitutive constant, the initial shear rate; τ^α is the resolved shear stress for that slip system α , g^α is the resistance against shear and n is the strain rate sensitivity. Sgn is the signum function that gives the sign of a real number.

The resolved shear stress is given by:

$$\tau^\alpha = \mathbf{S} : P^\alpha \quad (5.8)$$

or

$$\tau^\alpha = \mathbf{S} \cdot (m^\alpha \otimes n^\alpha) \quad (5.9)$$

the gradient of shear resistance \dot{g}^α is given as:

$$\dot{g}^\alpha = \sum_{\beta=1}^N h^{\alpha\beta} |\dot{\gamma}^\beta| \quad (5.10)$$

where β is also the slip system index, and N is the number of slip systems.

$h^{\alpha\beta}$ is the hardening matrix that represents the interaction between different slip systems α and β and is given by

$$h^{\alpha\beta} = q^{\alpha\beta} h_0 \left[\operatorname{sgn} \left(1 - \frac{g^\beta}{g_\infty^\beta} \right) \left| 1 - \frac{g^\beta}{g_\infty^\beta} \right|^a \right] \quad (5.11)$$

where $q^{\alpha\beta}$ is the latent hardening matrix, h_0 and a are constitutive constants, g^β is the resistance to shear on the β slip system, and g_∞^β is the saturated shear resistance on the slip system β . the shear resistances asymptotically evolve towards the saturated value.

Thus, this phenomenological power law constitutive model has ten parameters for computation. In the next chapter, we describe the methodology of computation by the Polarisation scheme of the spectral solution method.

CHAPTER 6

THE SPECTRAL METHOD: POLARISATION

Computational methods have become more popular owing to the expenses and time usage associated with experimental procedures to characterize structure-property relationships of microstructured materials. Lebensohn et al^[5] enumerates the many powerful numerical solution methods and tools that have been developed to predict responses of such materials undergoing plastic deformation.

Finite element methods have also been used in crystal plasticity problems extensively to predict more accurate behavior and to obtain locally resolved micromechanical stress/strain fields (Mika and Dawson^[6], 1999, Cailletaud et al^[7] and Clayton and McDowell^[8]). However the size of the finite element or the volume element that represents the microstructure at a particular material point that one can specify in a finite element analysis, is limited by the time taken to numerically solve partial differential equations. The computational cost associated is forbidding. The Spectral method is an alternative to it, and in this body of work, comparisons and contrasts have been drawn between the results obtained by FE simulations and **polarisation**.

Even though the spectral method is fairly new and was originally introduced in 1994 by Moulinec and souquet^[9], it has been used successfully used with polycrystalline materials (Grennerat et al^[10] and Lebensohn et al^[5]). Its superiority over a finite element approach has been demonstrated by Prakash and Lebensohn^[11] and Liu et al^[12]. In this chapter, we talk about the polarisation scheme of spectral solution.

6.1 The kinematics

Let us consider in a real space \mathbf{R}^3 , a hexahedral volume element or microstructural domain \mathbf{B}_0 in which we are interested and on which an external macroscopic deformation gradient $\bar{\mathbf{F}}$ has been

imposed. This domain will change and result in a deformed configuration \mathbf{B} . A field defined by $\chi(x) : x \in \mathbf{B}_0 \rightarrow y \in \mathbf{B}$ maps points x in the reference configuration \mathbf{B}_0 to points y in the deformed configuration \mathbf{B} . This map of deformation can be split into the sum of the applied macroscopic displacement field and a locally fluctuating displacement field $\tilde{\mathbf{w}}$:

$$\chi(x) = \bar{\mathbf{F}}x + \tilde{\mathbf{w}}(x) \quad (6.1)$$

on surfaces ∂B^- and ∂B^+ , a periodicity of $\tilde{\mathbf{w}}^- = \tilde{\mathbf{w}}^+$ is imposed. Similarly, the total deformation gradient \mathbf{F} is the gradient of the deformation mapping $\chi(x)$, that is $\mathbf{F} = \frac{\partial \chi}{\partial x} = \vec{\nabla} \chi = \text{grad} \chi$. It can be decomposed into the macroscopic imposed gradient $\bar{\mathbf{F}}$ and a locally fluctuating gradient $\tilde{\mathbf{F}}$:

$$\mathbf{F} = \bar{\mathbf{F}} + \tilde{\mathbf{F}} \quad (6.2)$$

where

$$\tilde{\mathbf{F}} = \tilde{\mathbf{w}} \otimes \nabla = \vec{\nabla} \tilde{\mathbf{w}} = \text{grad} \tilde{\mathbf{w}} \quad (6.3)$$

6.2 Static Equilibrium

The response of the material is governed by the phenomenological constitutive law (chapter 6). This relates the First Piola Kirchoff stress \mathbf{P} (or the second piola Kirchoff stress because $\mathbf{S} = \mathbf{F}^{-1}\mathbf{P}$), at every point in the material in the initial reference configuration, by means of a density functional W , such that

$$\mathbf{P}(\mathbf{x}) = \frac{\delta W}{\delta \mathbf{F}(\mathbf{x})} = \mathbf{f}(x, \mathbf{F}, \dot{\mathbf{F}}, \xi) \quad (6.4)$$

where ξ is the set of continuously evolving variables and parameters from the constitutive description. \mathbf{P} might also be a function of its neighborhood, but that is not considered in our modeling. The static equilibrium can be formulated by either the *Direct Variational* or the *Mixed Variational* formulation. The polarisation scheme uses the mixed variational formulation as described below: To obtain the equilibrium deformation field, we minimize W over all deformation gradients that satisfy the prescribed macroscopic deformation field and the local periodicity as mentioned in

equations 6.1 to 6.3. One of the other constraints imposed is the compatibility of the deformation gradient field:

$$\min_{\mathbf{F}} [W(\mathbf{F})] \longrightarrow \mathbf{F} = \overrightarrow{\nabla \chi} \quad (6.5)$$

If we introduce a Lagrange multiplier field $\Lambda(\mathbf{x})$ and a penalty term, where a stiffness tensor A is used as the parameter for penalty, then the resulting equation becomes:

$$\mathcal{L}[\mathbf{F}, \chi, \Lambda] = W + \int_{B_0} \mathbf{F}(\mathbf{x}) \Lambda(x) \cdot [\overrightarrow{\nabla \chi(x)} - \mathbf{F}(\mathbf{x})] dx + \frac{1}{2} \int_{B_0} [\overrightarrow{\nabla \chi(x)} - \mathbf{F}(\mathbf{x})] \cdot A [\overrightarrow{\nabla \chi(x)} - \mathbf{F}(\mathbf{x})] dx \quad (6.6)$$

According to Fortin and Glowinski^[13], the saddle point of this equation, or the minimum, is the static equilibrium condition. This results in the following three stationary conditions:

$$\frac{\delta \mathcal{L}}{\delta \mathbf{F}(\mathbf{x})} = \mathbf{P}(\mathbf{x}) - \mathbf{F}(\mathbf{x}) \Lambda(x) + A (\mathbf{F}(\mathbf{x}) - \overrightarrow{\nabla \chi(x)}) = 0 \quad (6.7)$$

$$\frac{\delta \mathcal{L}}{\delta \chi(\mathbf{x})} = \nabla \cdot [\mathbf{F}(\mathbf{x}) \Lambda(x) - A (\mathbf{F}(\mathbf{x}) - \overrightarrow{\nabla \chi(x)})] = 0 \quad (6.8)$$

and

$$\frac{\delta \mathcal{L}}{\delta \Lambda(x)} = \overrightarrow{\nabla \chi(x)} - \mathbf{F}(\mathbf{x}) = 0 \quad (6.9)$$

When a *Fourier transform* is applied to these periodic functions, we get the equivalent equations:

$$\mathbf{P}(\mathbf{k}) - \Lambda_R(\mathbf{k}) + A [\mathbf{F}(\mathbf{k}) - \chi(\mathbf{k}) \otimes i\mathbf{k}] = 0 \quad (6.10)$$

$$\chi(\mathbf{k}) = \mathcal{A}(\mathbf{k})^{-1} (A \mathbf{F}(\mathbf{k}) - \Lambda_R(\mathbf{k})) i\mathbf{k} \quad (6.11)$$

and

$$\chi(\mathbf{k}) \otimes i\mathbf{k} - \mathbf{F}(\mathbf{k}) = 0 \quad (6.12)$$

where $\Lambda_R(\mathbf{x}) = \mathbf{F}(\mathbf{x}) \Lambda(\mathbf{x})$, and $\mathcal{A}(\mathbf{k})$ is an acoustic tensor, defined as

$$\mathcal{A}(\mathbf{k}) \mathbf{a}(\mathbf{k}) = A [\mathbf{a}(\mathbf{k}) \otimes i\mathbf{k}] i\mathbf{k} \quad (6.13)$$

for a vector field $\mathbf{a}(\mathbf{k})$. Using equation 6.11 in 6.10 and 6.12 to eliminate $\chi(\mathbf{k})$ yields the field of the deformation gradient at equilibrium as the solution to:

$$\mathcal{R}_{mixed}[\mathbf{F}(\mathbf{k}), \Lambda(\mathbf{k})] := \left\{ \begin{array}{l} \mathbf{P}(\mathbf{k}) - \Lambda_R(\mathbf{k}) + A\{\mathbf{F}(\mathbf{k}) - \Gamma(\mathbf{k})\{A\mathbf{F}(\mathbf{k}) - \Lambda_R(\mathbf{k})\}\} \\ \mathbf{F}(\mathbf{k}) - \Gamma(\mathbf{k})\{A\mathbf{F}(\mathbf{k}) - \Lambda_R(\mathbf{k})\} \end{array} \right\} = 0. \quad (6.14)$$

where the $\Gamma(\mathbf{k})$ operator is defined such that $\Gamma(\mathbf{k})\mathbf{T}(\mathbf{k}) = [\mathcal{A}(\mathbf{k})^{-1}\mathbf{T}(\mathbf{k})i\mathbf{k}] \otimes i\mathbf{k}$ for a tensor field $\mathbf{T}(\mathbf{k})$.

After the formulation of the constitutive laws, kinematics and static equilibrium conditions, we now take a look at the numerical implementation.

6.3 Numerical Implementation

The framework for the numerical implementation is based on the methodology of finite-strain developed by Eisenlohr et al^[14], where the domain B_0 is discretized into a regular grid of N points ($N = N_x + N_y + N_z$) in three dimensions. The solution is approximated in a discretized fourier space associated with the grid. The stiffness A is obtained as the average of the maximum and minimum value of $\left\| \frac{d\mathbf{P}}{d\mathbf{F}}(\mathbf{x}) \right\|_F$.

There are three schemes for discretization: Basic scheme, Lagrange multiplier field based scheme, and the Polarisation scheme. In our body of work, we have extensively used the polarisation scheme.

6.3.1 polarisation scheme of discretization

In this scheme, \mathcal{R}_{mixed} from equation 6.14 is expressed in terms of the deformation gradient $\mathbf{F}(\mathbf{x})$ and a rescaled polarisation field $\mathbf{F}_\tau(\mathbf{x})$ such that $\mathbf{F}_\tau(\mathbf{x}) = \mathbf{F}_\lambda(\mathbf{x}) + \mathbf{F}(\mathbf{x})$. Thus, using a collocation based approach at the grid points to discretize the mixed variational formulation of the static equilibrium, and transforming the equation 6.14 as mentioned, we arrive at a well scaled system of

equations:

$$\mathcal{R}_\tau[\mathbf{F}(\mathbf{x}), \mathbf{F}_\tau(\mathbf{x})] := A^{-1}\{\mathbf{P}(\mathbf{x}) - \Lambda_R(\mathbf{x})\} + \beta\mathbf{F}(\mathbf{x}) - \mathcal{F}^{-1}[\Gamma(\mathbf{k})\{\beta A\mathbf{F}(\mathbf{k}) - \alpha\Lambda_R(\mathbf{k})\}] \quad if \quad k \neq 0 \quad (6.15)$$

$$\mathcal{R}_\tau[\mathbf{F}(\mathbf{x}), \mathbf{F}_\tau(\mathbf{x})] := A^{-1}\{\mathbf{P}(\mathbf{x}) - \Lambda_R(\mathbf{x})\} + \beta\mathbf{F}(\mathbf{x}) - \mathcal{F}^{-1}[\{\beta\mathbf{F}_{BC}\}] \quad if \quad k = 0 \quad (6.16)$$

and

$$\mathcal{R}_\tau[\mathbf{F}(\mathbf{x}), \mathbf{F}_\tau(\mathbf{x})] := \beta\mathbf{F}(\mathbf{x}) - \mathcal{F}^{-1}[\Gamma(\mathbf{k})\{\beta A\mathbf{F}(\mathbf{k}) - \alpha\Lambda_R(\mathbf{k})\}] \quad if \quad k \neq 0 \quad (6.17)$$

$$\mathcal{R}_\tau[\mathbf{F}(\mathbf{x}), \mathbf{F}_\tau(\mathbf{x})] := \beta\mathbf{F}(\mathbf{x}) - \mathcal{F}^{-1}[\{\beta\mathbf{F}_{BC}\}] \quad if \quad k = 0 \quad (6.18)$$

where $\Lambda_R(\mathbf{x}) = \mathbf{F}(\mathbf{x})A[\mathbf{F}_\tau(\mathbf{x}) - \mathbf{F}(\mathbf{x})]$. The coefficients α and β are the relative weights for the equilibrium and compatibility conditions respectively and they have an effect on the convergence rate of the solution as expounded upon by Moulinec and Silva^[15]. \mathbf{F}_{BC} is the deformation gradient at the boundary conditions. The constitutive evaluation is performed on the compatible deformation gradient \mathbf{F}_c , which is given by:

$$\mathbf{F}_c(\mathbf{x}) = \beta^{-1}\Gamma(\mathbf{x}) \times [\beta A\mathbf{F}(\mathbf{x}) - \alpha\mathbf{F}(\mathbf{x})A\{\mathbf{F}_\tau(\mathbf{x}) - \mathbf{F}(\mathbf{x})\}] \quad (6.19)$$

Since the constitutive evaluation is performed on this compatible deformation field, the convergence speed increases significantly.

6.3.2 Numerical solution strategy

Balay et al^[16] 2013, describes a PETSc library of non-linear solution methods which are employed to solve the system of discretised equations. The residual at an iteration is obtained by evaluating equation 6.15, to 6.18 at the grid points. The convolution operation to obtain the Γ functional, uses fast fourier transforms. In DAMASK, out of all the PETSc library solution methods, the non-linear generalised minimum residual method is the default. In this method, an updated solution $\{\square\}_{n+1}$ is found by linearly combining m previous solutions in a Krylov subspace $\mathcal{K}_n = \text{span}\{\{\square\}_n, \dots, \{\square\}_{n-m+1}\}$ for which the norm of the residual is minimum:

$$\min_{\{\square\}_{n+1} \in \mathcal{K}_n} \left\| \frac{\partial \mathcal{R}}{\partial \{\square\}_n} [\{\square\}_{n+1} - \{\square\}_n] + \mathcal{R}\{\square\} - n \right\|_2 \quad (6.20)$$

This residual is calculated without Jacobians (Oosterlee and Washio^[17]). The updated deformation gradient field is a Linear combination of compatible fields. DAMASK also supports two other numerical solution strategies, namely Non-Linear Richardson and Inexact Newton generalised minimum residual, described in Shanharaj.P et al^[18].

In the next chapter the Procedure that was followed to answer the research question of interest "*whether or not the finite element method underestimates the grain boundary strains as compared to strains at the bulk because of its inherent stiffness and inability to increase grid resolution, and if the spectral solver does a better job at it*" has been described.

CHAPTER 7

PROCEDURE

The Düsseldorf advanced materials simulation kit (F.Roters et al^[19]) is the software that was used to simulate the oligocrystal under uniaxial tension. It was built to simulate crystal plasticity within a finite strain continuum mechanical framework (Eisenlohr et al^[14]). It has both finite element capability (MSC Marc Mentat) and inbuilt spectral solvers. More documentation can be found at <http://www.damask.mpie.de>

The modeling of the Oligocrystal begins with the creation of a geometry file that contains, as the name suggests, the geometry description of the polycrystalline aggregates, viz, the texture data, the grain IDs allocated to each texture, the coordinates where each grain exists, and the spatial arrangement of the aggregates. Any peripheral air layers or rigid plates are also described in here. What the geom commands do is assign the stipulated textures to each material point (pixel), search the neighborhood (globally) for similar textures with a 5°misorientation tolerance, and groups them as one grain; rather, assigns the same grain ID to them.

The next step is the creation of a material configuration file that contains in itself the constitutive laws and its description, to be applied to the air layers, rigid base plates, the actual polycrystalline aggregate, the texture data, the homogenization scheme if any, the output needed from the simulation, and each of those are then allocated to the grains.

The third step is the creation of a numerical configuration file which specifies the tolerances, the error divergences, numerical solving strategies, discretization schemes of the fourier space and all the parameters described in the previous chapter that are needed to solve the equations of the spectral description numerically.

A loadcase file needs to be specified, which contains in itself the deformation gradient, the rate of strain the number of increments, and the number of increments after which the output is written to the output file.

In the next sections, we describe in somewhat detail, the creation of these files for our simulation.

7.1 Setting up the Geometry files in DAMASK environment

The EBSD data file containing the x and y coordinates, the Orientation matrix for the material points and the phase data was obtained from Sandia National Laboratories (SNL), Albuquerque, New Mexico, USA.

The first step was to create an IPF color image seen along the (100), (010) and the (001) directions, to compare them with the actual EBSD images obtained from SNL. Figure 7.1 shows the comparison. It was observed that the images match for all three directional views, and thus the data obtained is correct and comparable.

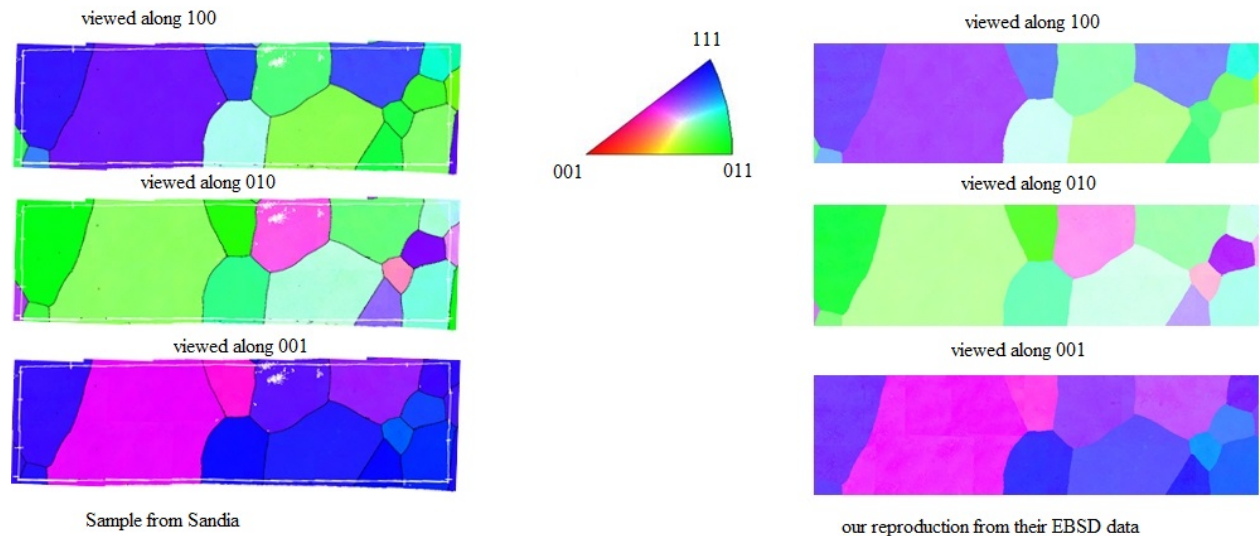


Figure 7.1: Comparison of their IPF color maps, with those produced by our software. The figures on the left are those produced at SNL, experimentally in the EBSD. The ones at the right are produced by the `imageDataRGB` command in DAMASK

The next step, was to create a two-dimensional geometry file (because the EBSD data set contains only two coordinates) by using the '*geom_fromTable*' command in DAMASK (Figure7.2), and extrude it in the z-direction to obtain the 3-dimensional oligocrystal.

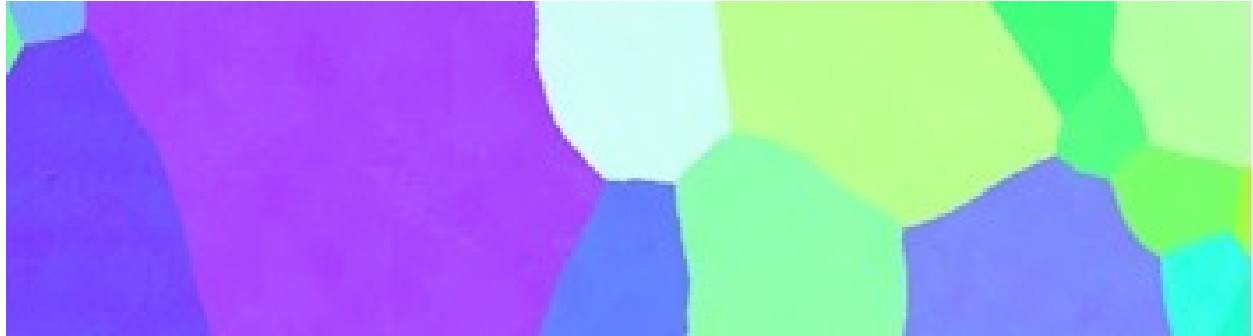


Figure 7.2: The 2 dimensional geometry file (thickness in z direction = 1) which will be extruded. The x axis is towards the right and the y axis is upwards.

The aspect ratios for size and grid resolution (1084x294x168) was kept similar to that in the work done by Lim et al^[1]. It is shown in Figure7.3.

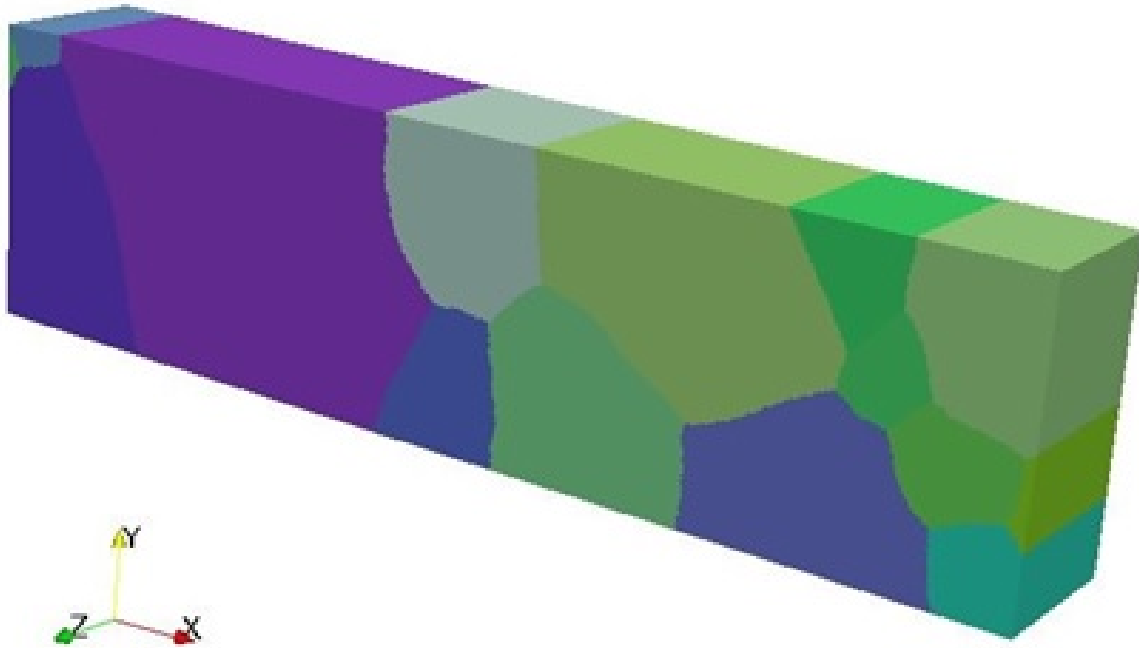


Figure 7.3: The Oligocrystal, made by extruding the 2D structure in the z direction. The aspect ratios have been maintained. Resolution: 1084x294x168. Voxel aspect ratio x:y:z :: 1:1:1

From this, three more geometry descriptions with decreasing resolutions were created, viz., viz 1084x294x21 (voxel aspect ratio: 1:1:8), 542x147x21(Voxel aspect ratio: 1:1:4), and 271x74x10(voxel aspect ratio: 1:1:4). To this end, the command used was *geom_rescale*.

The next step was to attach a rigid baseplate, 10% of the length of the oligocrystal in thickness with microstructure ID 1 to the y-z plane of the 3D oligocrystal. This acts a a periodic boundary condition that no deformation happens in the x-direction which is also the direction of the uniaxial tension. A periodic isotropic air layer was attached laterally (xz and xy planes) around the oligocrystal, 10% of the thickness of the oligocrystal in thickness, and it was assigned a grain ID value of 2. Initially, the air layer was attached first and then the rigid plate, and this resulted in the air layer to become periodically discontinuous and the rigid base-plate to become periodically continuous. This was achieved by using the commands of *geom_translate* and *geom_canvas* (Figure 7.4 and 7.5)

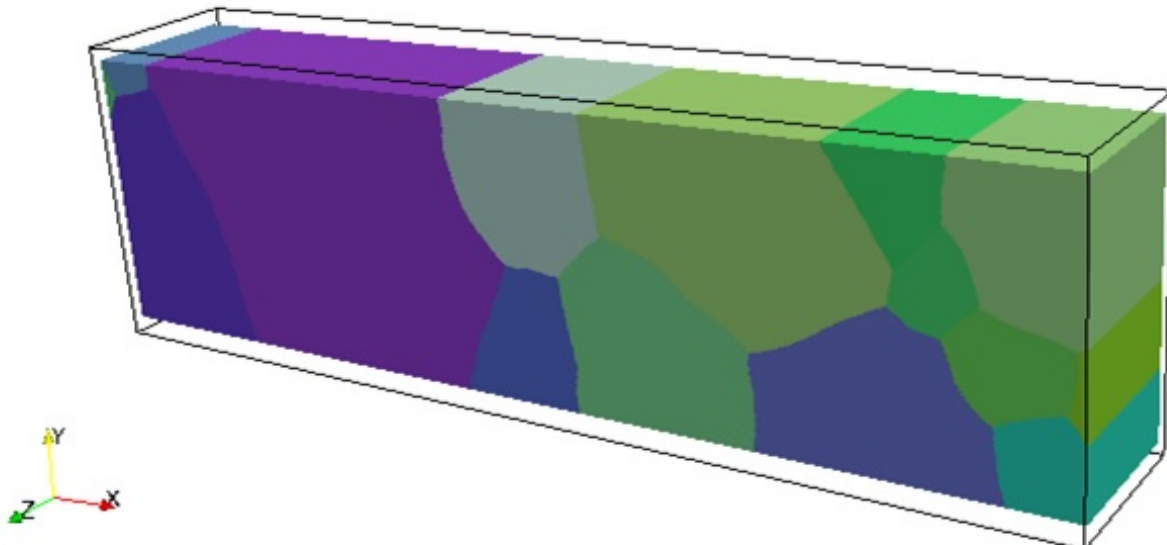


Figure 7.4: The Oligocrystal with the isotropic airlayer around it.

This was later changed in the sense that first we added the baseplate and then the airlayer, thus making the airlayer continuous, while the baseplate became discontinuous. This new geometry when rendered in Paraview, looks like those shown in Figure 7.6 and 7.7

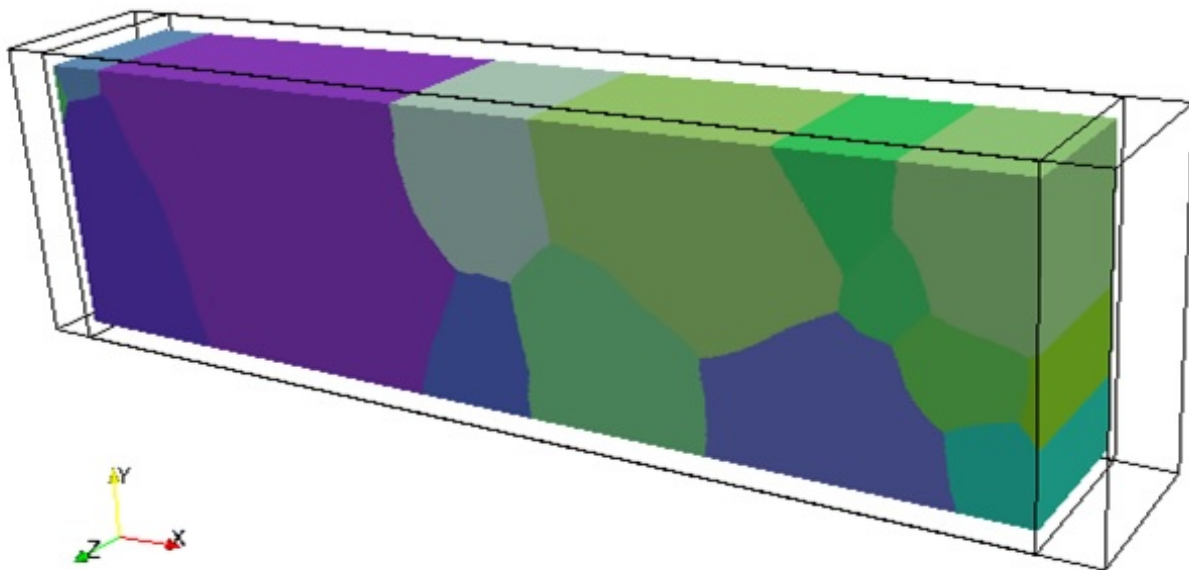


Figure 7.5: The Oligocrystal with the rigid elastic baseplate added at both ends. This makes the baseplate continuous because of the periodic structure and renders the air layer discontinuous

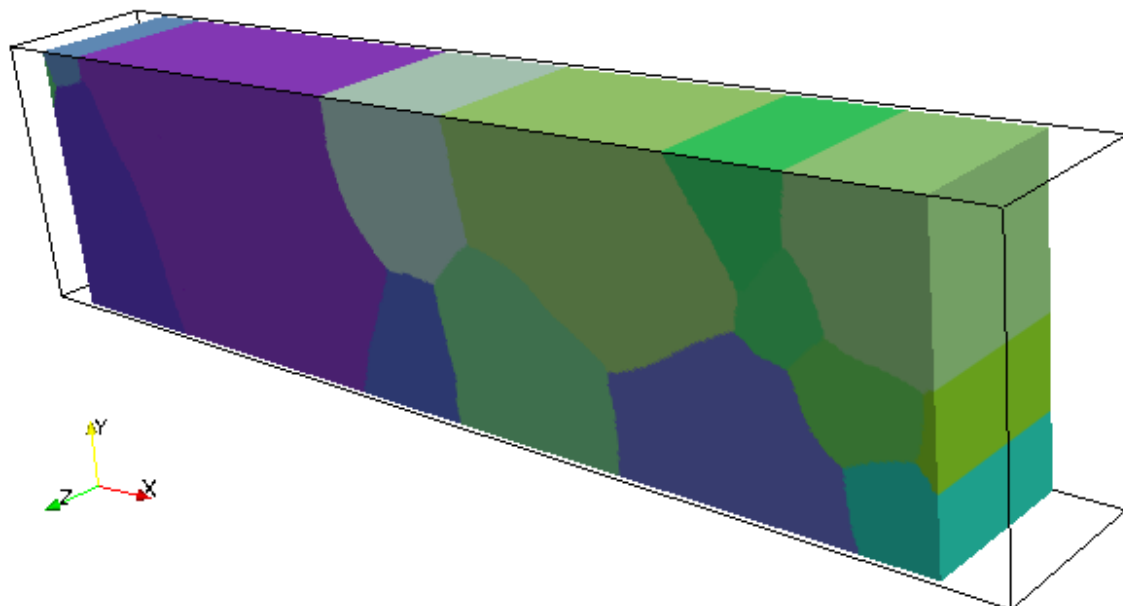


Figure 7.6: The rigid baseplate is added first in this new assignment of boundary conditions

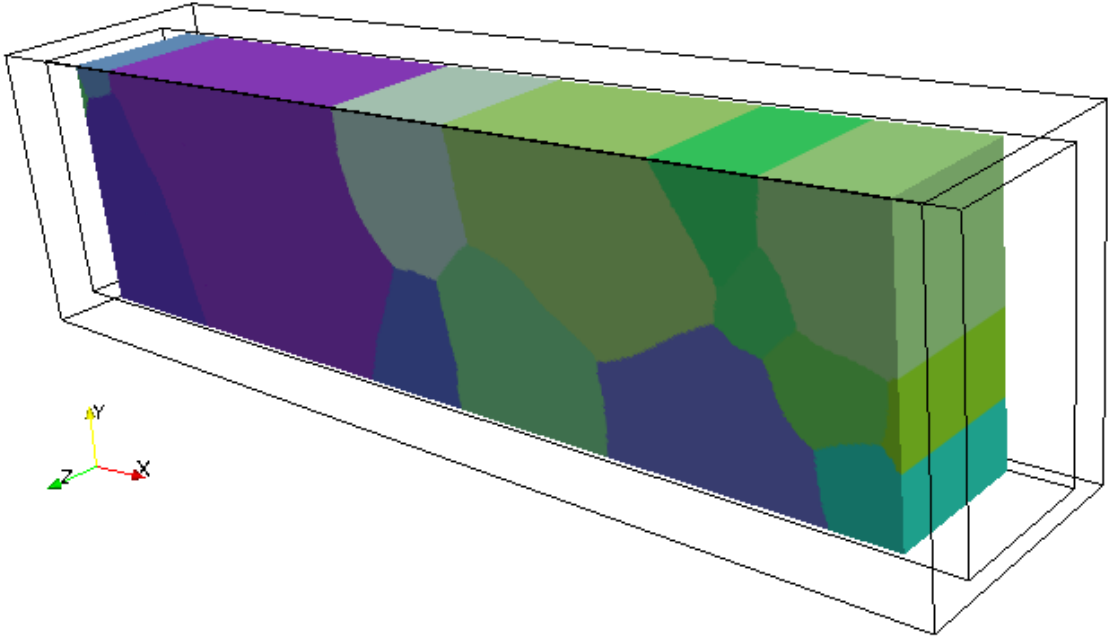


Figure 7.7: The isotropic plastic air layer is added around the baseplate and the Oligocrystal. This makes the baseplate periodically discontinuous, while the airlayer becomes continuous.

All the color assignments were done using the *addIPFcolor* and *imageDataRGB* commands inbuilt in DAMASK. Paraview was used for visualization. The command *geomccheck* produces a file with .vtr extension, that can be rendered in paraview. To this file, we can attach the color data, and basically any scalar values by using the command *vtkAddRectilinearGridData* that we need to visualize in Paraview.

The detailed step by step usage of the various commands is shown in Appendix A.

7.2 Setting up the Material configuration

The material.config file as supported in DAMASK has many sections. The first one is homogenization, to which a value of NONE was assigned. The second is Crystallite, where the outputs we need (deformation gradient f, elastic deformation gradient tensor fe, first piola kirchoff stress p, grain rotation, texture and orientation) were specified, and that each crystallite is a single crystal by

itself but the entire sample is a polycrystal. Then in the phase section three phases were specified: Phenomenological power law fcc aluminum for the oligocrystal, rigid elastic solid for the base-plate and an isotropic air layer. Next sections have the microstructures and textures which assign the orientations to each grain, and also specify which grain has what phase(s) and how much of each phase is present, what crystallite and what grain ID. The material configuration file has been shown in Appendix B.

7.3 Setting up the Numeric Configuration

The built in numerics.config file looks like that shown in the Appendix C. The error tolerance divergence was changed (it was decreased approximately 10 times) and the Spectral solution method was also changed (from a basic method to a polarisation method) as shown in Appendix D.

7.4 Simulation

7.4.1 Simulation by the Spectral Method

The load case file was created and is shown in Appendix E. It specifies that the simulation has to run until 7% strain has been achieved in 70 increments. The frequency with which output would be written out into the output file was also specified as well as a restart capability was added so that the simulation can be resumed from the previous increment if it stopped in between due to unforeseen circumstances. The DAMASK spectral solver was called by the command "*DAMASK_spectral*", inside a .qsub file which submitted our job to the cluster at the high performance computing center at Michigan State University. The.qsub file specifies the walltime needed for the program to run, the number of nodes and number of cores per node needed for parallel computing, the memory required for the job, the environment variables, and the actual command for simulation. An exemplar qsub file is shown in Appendix F

7.4.2 Simulation by Finite element method

MSC Marc Mentat was invoked to set up the finite element model. A command 'mentat_spectralBox' was used to translate the geometry file already made into Mentat. Other parameters were then set up using the functionalities such as boundary conditions, domain decomposition etc provided in Mentat. 8 domains were used to reduce computational time. To make the output give the desired crystallite results, marc_addUserOutput command was used before the fem simulation was allowed to run its course.

7.5 Analysis tools used to obtain and compare results

The *postResults* command was used to extract data from the output file (the output file has an extension .spectralOut in case of spectral solution output, and .t16 in case of FEM output), and the Cauchy stress and a left logarithmic strain was appended to it by using the crystallite outputs for the very last increment. Mises stress and strain was then calculated and appended to the table, and so were the grain rotations. A .vtr file was made for each geometry description, and the Mises and grain-rotation scalars were mapped onto it and rendered in paraview to draw conclusions. Comparisons were done between spatial maps by plotting cumulative frequency plots for the ratio of values at each spatial point. To obtain the strains at the grain boundaries and bulk of the grain, in order to compare the difference with those found by FEM at Sandia, the Euclidean distance of each material point (distance in number of voxels from closest grain boundary) from the nearest grain boundary was added to the output table, and then a separate table where the average stress and strain per grain were listed was created. The strain at each material point was then normalized by dividing them with the average strain per grain. These normalized strains were then plotted along the y-axis with the euclidean distance along the x-axis for each such grain, and for each grid resolution to draw conclusions. The *binXY* command was used to create a probability density map for these two quantities, and then it was plotted in Gri. The actual commands used for processing the results are appended in Appendix G.

Results obtained are described in the next chapter, along with the comparisons made and conclusions drawn from the study. For more detailed explanations of the commands, the software used, and the values that are used in this simulation, please be referred to the official website of DAMASK: <http://damask.mpie.de>

CHAPTER 8

RESULTS AND CONCLUSIONS

In this body of work only the strains inside the grains, and in the overall oligocrystal, and the grain rotations that have occurred as a result of the deformation have been analyzed.

Figure 8.1 shows the results that Sandia National Laboratories obtained from the CPFEM solution, and how it compared with the experimental results. As can be clearly seen upon comparing the images on the left with those on the right, the CPFEM solution underestimated the grain boundary strains when compared with the High Resolution Digital Image Correlation (HRDIC) method of obtaining strain maps experimentally. This method has been elaborated in the work by Lim et al^[1] 2014. The strains near the grain boundaries are of a higher magnitude for the HRDIC case as compared to those in the CPFEM case.

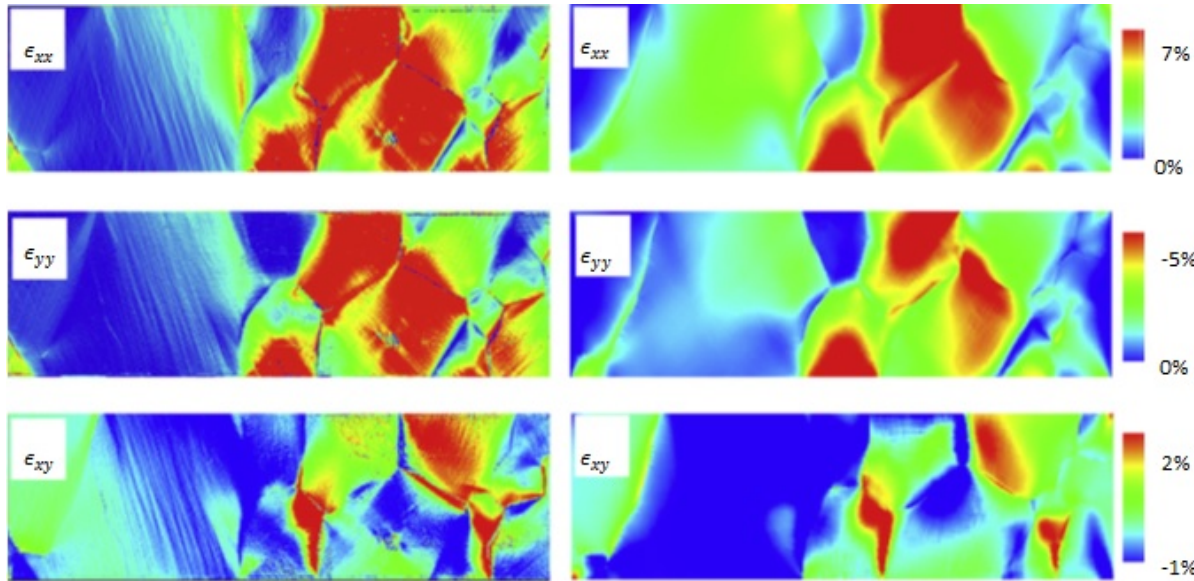


Figure 8.1: The HRDIC versus CPFEM strain maps. The column of images on the left shows the strain map of the oligocrystal obtained by high resolution digital image correlation, while those on the right are obtained by CPFEM. In our work, we have focused only on the strain in the x direction, i.e., ϵ_{xx} . the positive x direction is towards the right, and positive y is upwards.

In our work, we focused on the strains in the x direction only (ϵ_{xx}), and have tried to see if just

by changing the simulation solution method from FEM to spectral solution, if this problem of grain boundary strain underestimation can be overcome. This would also relate to the fact that FEM is a stiffer solution method than spectral solution, and that inherent problem might be the plausible cause for the discrepancies observed.

First,a strain map was generated by spectral solution for the mesh with the lowest resolution, and it has been shown in Figure 8.2. This was rendered in paraview. The boundary conditions for this are shown in figure 7.5.

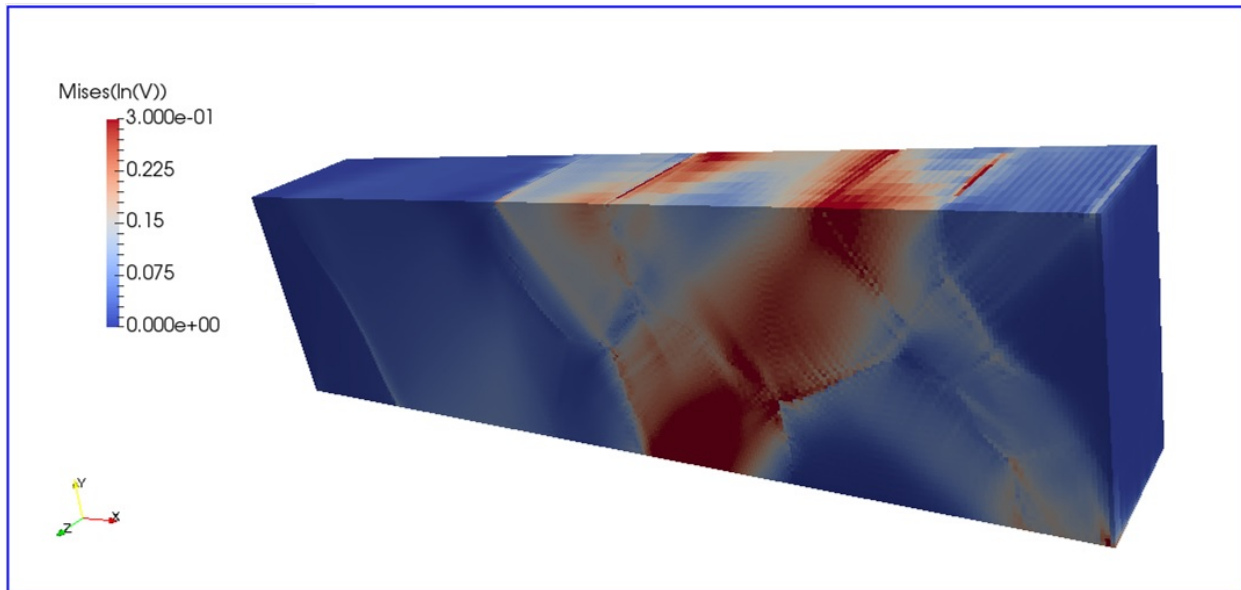


Figure 8.2: The strain map generated in three dimensions by DAMASK.The color scale has been modified so that anything above 0.3 is the same shade of red as 0.3, and anything below 0 is the same shade of blue as 0.

We tried to see if by changing the boundary conditions from that shown in Figure 7.5, to that in Figure 7.7 (i.e., by creating a periodically continuous isotropic air layer and a periodically discontinuous elastic baseplate) what would be the effect on the strains observed. The results are shown in Figure 8.3

This change in boundary conditions did not necessarily have any effect on the results as can be gathered from Figure 8.4.

Next, mesh resolution was increased just in the z direction, i.e, increase the z resolution 2 times

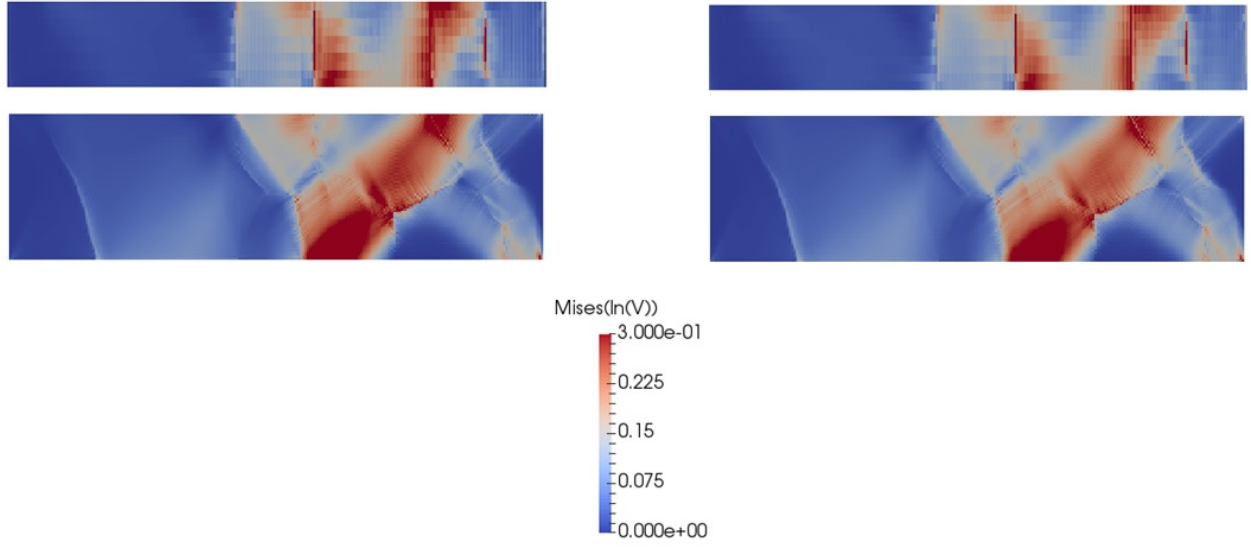


Figure 8.3: The comparison of strain maps upon change of boundary conditions. Left side images show the results that had the older boundary conditions, while those on the right have the newer boundary conditions.

more (271x74x21 mesh resolution with Voxel aspect ratio: 1:1:2) in an attempt to see if more equiaxed voxels will have any effect on the strains calculated. The results are shown in Figure 8.5

The similarity between the two spatial maps is quantitatively shown in Figure 8.6.

If we consider the grain rotations, as obtained from the simulation of the lowest resolution mesh, and the one with a twice larger resolution in the z direction, we find that the grain rotations are greater near the grain boundaries which also gives impetus to the fact that strain accumulations are greatest near the grain boundaries. The results have been shown in Figure 8.7. The initial input orientations (as Quaternions) and final output orientations (as Quaternions) were used to obtain the grain rotation values. The conjugate of the initial orientation was multiplied with the final orientation and lastly converted into angle axis representation using built in DAMASK functions and formulae, in order to obtain the final rotation data.

The similarity between both grain rotation results have been quantitatively represented in Figure 8.8

Even though the grain rotations on the xy plane are pretty encouraging to our cause and are consistent, those in the xz plane show oscillation and a band like structure. A rotated geometry

Ratio of Mises strains calculated with a periodically continuous baseplate to those calculated with a periodically discontinuous baseplate

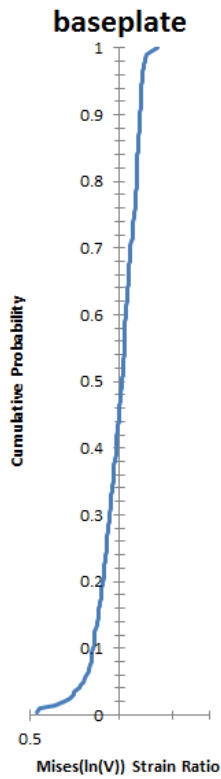


Figure 8.4: The comparison of strain maps upon change of boundary conditions, shown as the cumulative probability of ratios of strains at each material point calculated with the two different periodic boundary conditions.

with the y and z directions interchanged, yielded the following result (Figure 8.9)

Since rotating the geometry file did not provide any appreciable reduction in the banding, and since the non-thickness direction planes do not show banding, then the oscillating nature of spectral solution as a possible candidate for causing the banding can be ruled out.

A hypothesis was made that maybe this is happening because the voxels are tetragonal and not cubic, with the z direction of each voxel 2 to 8 times the dimensions in the x and y direction (for example, the voxel aspect ratio is 1:1:4 for 271x74x10 and 1:1:2 for 271x74x21 mesh resolution). To address this, an unrotated geometry file with mesh resolution 271x74x42 was created, so that the voxels were equiaxed (aspect ratio 1:1:1). Simulations with the spectral method were done on

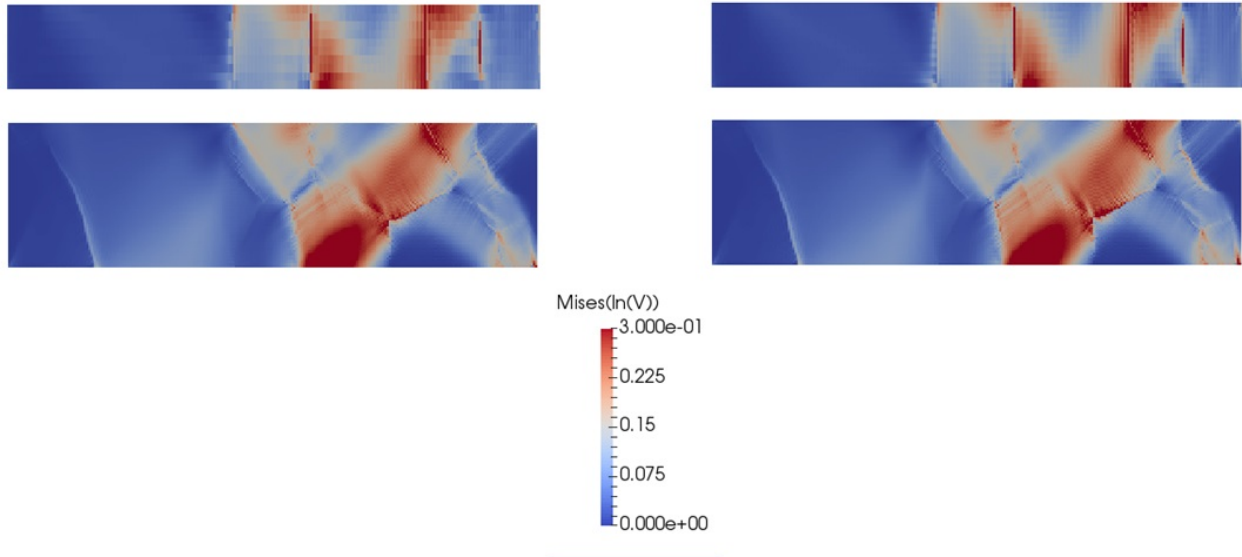


Figure 8.5: The comparison of strain maps upon increasing resolution in the z direction. Left side images show the results that had been obtained with a lower z resolution, while the right shows the results obtained after increasing the z resolution by a factor of 2. As is evident just by visual inspection, the change in increasing the z resolution does not effect any major change, but the gradients become smoother

this new geometry file, and an appreciable decrease in banding was observed (Figure 8.10). Thus, for the spectral solution method to provide proper results without any surprises, it is desirable to have the voxels as close to equiaxed as possible. Owing to the increase in computational cost if the geometry files were all created with equiaxed voxels, the geometry descriptions in this body of work do not have appreciable equiaxedness. Grain rotations of only the xy planes have thus been considered.

After the mystery of the banding was solved, a comparison was made between the grain rotation values calculated by CPFEM with those calculated by spectral solution for a constant mesh resolution of 271x74x10. the voxel aspect ratio for both cases were 1:1:4. no banding can be seen in the CPFEM solution, even with non-equiaxed voxels, whereas the spectral solution shows the banding. Apart from that, most of the grain rotations in the bulk of the grains appear to be similar. However, near the grain boundaries, the spectral solution seems to estimate higher amount of grain rotation than CPFEM, which shows that the Spectral solution method estimates higher strains near grain boundaries as compared to CPFEM because higher strain concentrations imply higher grain

ratio of mises strains calculated at 271x74x21 to those calculated at 271x74x10 mesh resolution

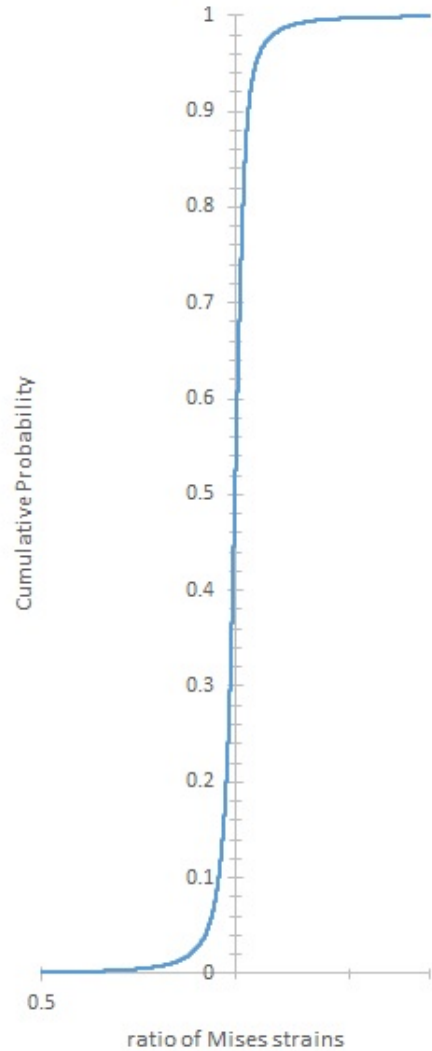


Figure 8.6: The quantitative comparison of strain maps upon change of z resolution. cumulative probability of the ratio of strains calculated at each material point for resolution 271x74x21 to those at 271x74x10 has been shown.

rotations. The results are shown in the Figure 8.11.

A quantitative comparison by calculating the cumulative probability of the ratio of grain rotations calculated by FEM and that calculated by spectral solution method, is shown in the Figure 8.12

The grain rotations were calculated for the different resolutions using spectral solution, to see if

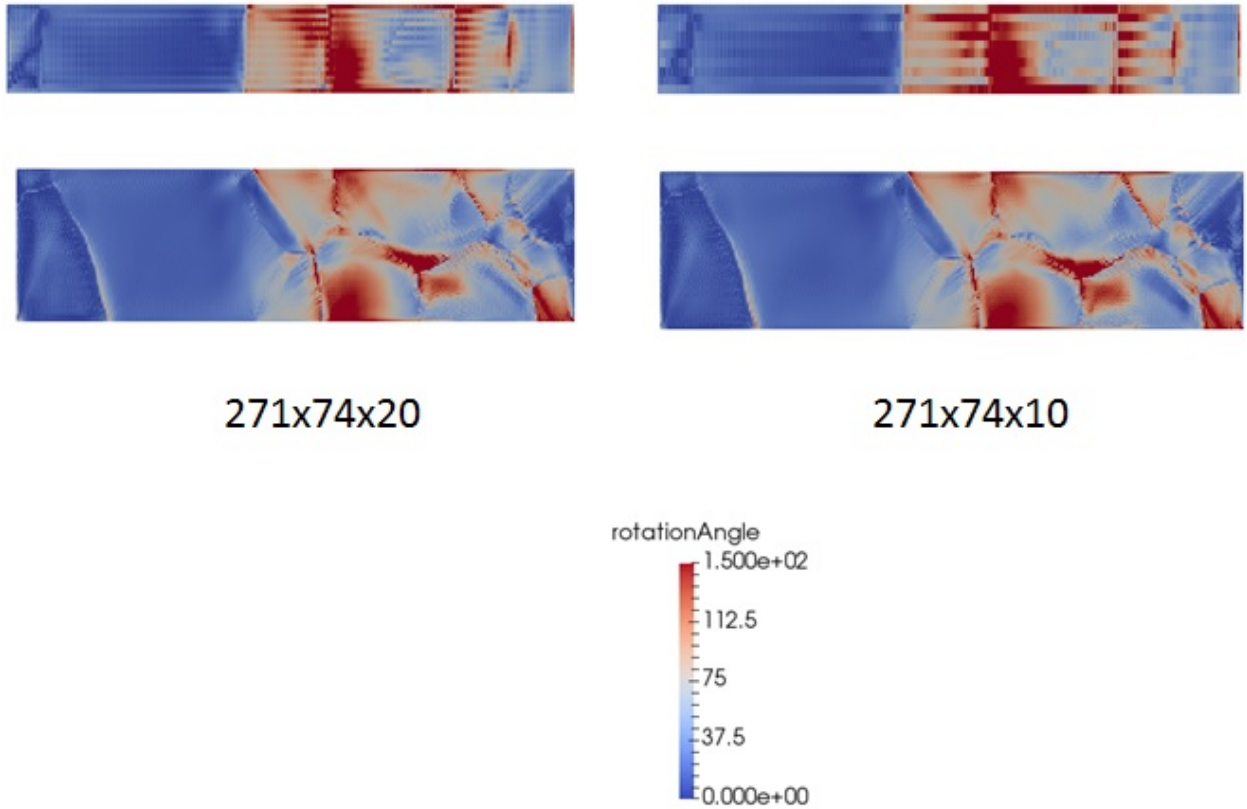


Figure 8.7: The comparison of grain rotations upon increasing resolution in the z direction. Left side images show the results that had been obtained with a higher z resolution. As is evident just by visual inspection, the change in increasing the z resolution does not effect any major change.

a change in resolution effects substantial change on the values calculated. When the grain rotations for different mesh resolutions of 271x74x10, 542x147x21 and 1084x294x21 are shown as spatial maps, they do not show much variation except for a smoother view (Figure 8.13).

The quantitative comparison is done by calculating the ratios of grain rotations at each material point calculated at 542x147x21 and 1084x294x21 mesh resolution to those calculated at 271x74x10 resolution, and then plotting the cumulative probability on the same plot (Figure 8.14).

This shows that the grain rotations calculated by the spectral method have higher values near the grain boundaries, and that is not just the effect of resolutions, because a change in resolution does not effect much of a change in the actual values calculated.

Moving on from grain rotation to strains, the CPFEM and spectral solution spatial maps for strains are shown in Figure 8.15.

Ratio of grain rotations calculated at 271x74x21 to those calculated at 271x74x10 mesh resolution

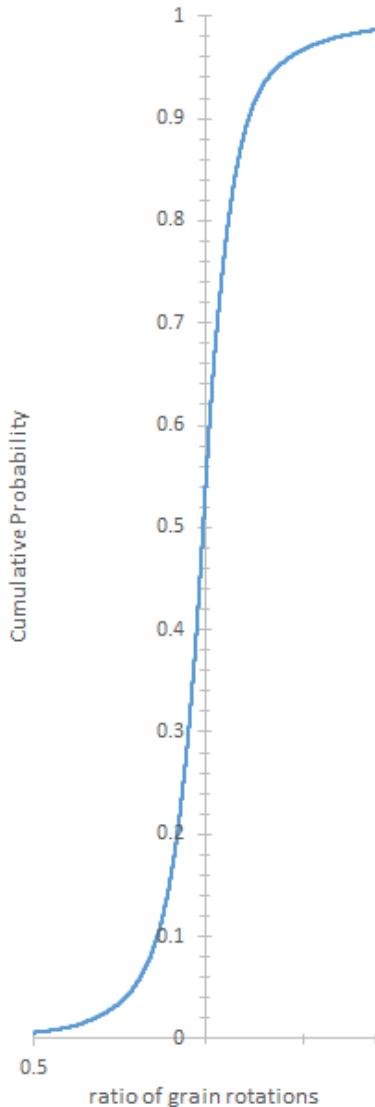


Figure 8.8: The quantitative comparison of grain rotation maps upon change of z resolution. Cumulative probability of the ratios of grain rotations calculated at each material point for the resolution 271x74x21 to those calculated at 271x74x10

The Figure 8.16 shows the quantitative comparison between these spatial maps.

This shows that even though the strains calculated are quite close to each other in both the CPFEM and spectral solution, there is a redistribution of strain. while the CPFEM has slightly higher strains in the bulk and lower strains near the grain boundaries, the spectral solution has slightly lower strains in the bulk and higher strains near the grain boundaries. This becomes even

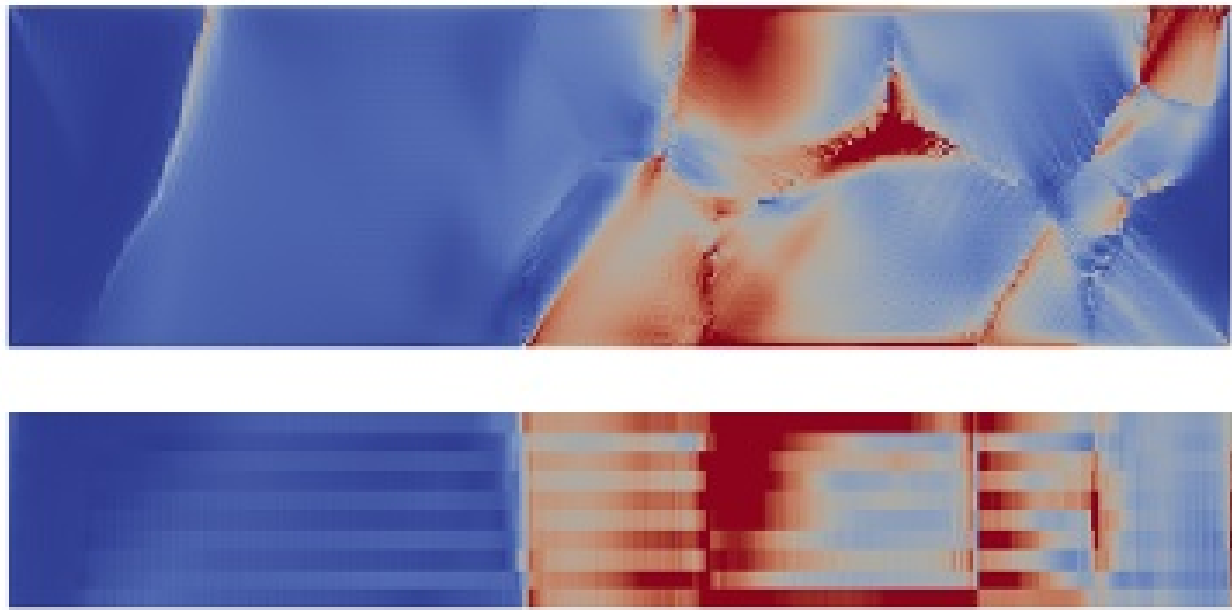


Figure 8.9: The grain rotation spatial map after simulating a rotated geometry. Mesh resolution 271x10x74, voxel aspect ratio 1:4:1. The top face and front face are interchanged from previous simulations because y and z directions are now interchanged due to the rotation. The band-like structure still exists in the thickness direction. The thickness direction was z in the previous ones, but y in the current one.

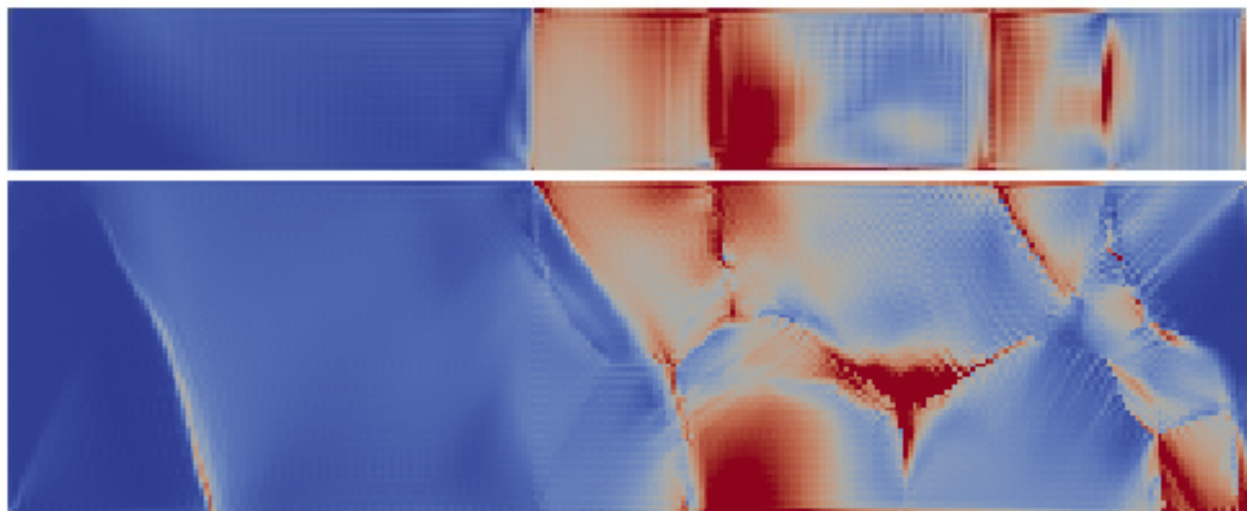


Figure 8.10: The grain rotation spatial map after simulating an unrotated geometry with equiaxed voxels. Mesh resolution 271x74x42, voxel aspect ratio 1:1:1. Little to no banding can be seen in the thickness direction. Thus, an equiaxed voxel is desirable.

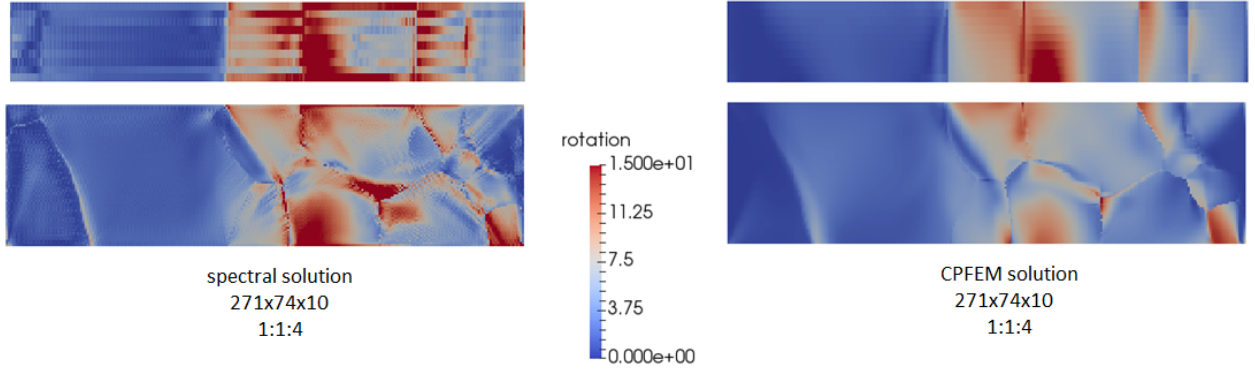


Figure 8.11: The grain rotation spatial maps comparing the CPFEM and spectral solution estimations of grain rotations. Mesh resolution 271x74x10, voxel aspect ratio 1:1:4. Little to no banding can be seen in the CPFEM solution. Spectral solution estimates higher grain rotation than FEM near the grain boundaries, but most of the other places, they estimate similar values of grain rotation as seen in Figure 8.12

more clear when we observe the GRI map which plots the euclidean grain boundary distance with the ratio of spectral solution strains to CPFEM strains (Figure 8.17).

This is a probability density plot, where white is 0 probability and black is 1 probability. Thus, for a black disc, for that euclidean distance, the strain ratios have a probability of 1, i.e, sure to occur, and 0 if it is a white disc. The columns of this map have been normalized, so that the darkest grey (or black) in the column shows where the strains are mostly located at that distance from the grain boundary.

An analysis of this plot clearly shows that at the center of the grain the ssm estimates strains less than fem, and thus the darker color appears below 1, while closer to grain boundaries, the darker colors are above 1. Thus, the spectral solution indeed estimates higher strains near grain boundaries than an FEM.

Upon considering spatial maps for strains calculated at various resolutions by the spectral method, we find no substantial change in the calculated strain values (Figure 8.18) with change in resolution. This fact is corroborated by the quantitative comparison in Figure 8.19.

different GRI maps for euclidean distance from closest grain boundaries versus normalized strains (strain at each material point, divided by the average strain of the grain that point belongs

Ratio of Grain Rotation calculated by FEM to those calculated by spectral method

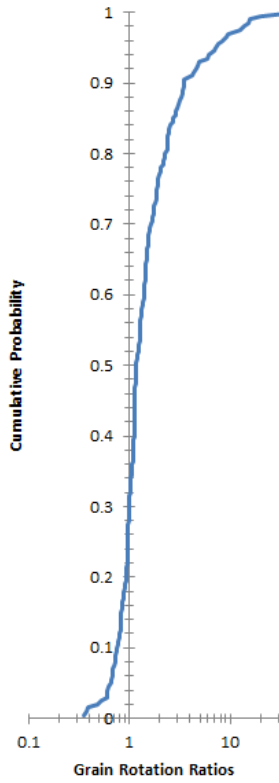


Figure 8.12: The cumulative probability of ratios of grain rotations calculated by FEM to those calculated by spectral solution

to) in the oligocrystals at various resolutions show that strains closer to grain boundaries are higher than the average and as we go closer to the bulk of the grains, it approaches the average strain value. Figure 8.20, Figure 8.21 and Figure 8.22 show these GRI maps. Since the euclidean distance is in terms of number of voxels, it increases integrally with integral increase in resolution of the spectral mesh. However, in Figure 8.23 which shows the same normalized strains in the oligocrystal versus the euclidean grain boundary distance for the case of FEM calculations, the highest probability near the grain boundary is for a normalized strain below 1. Thus, the spectral solution method does indeed estimate higher strains near grain boundaries than the CPFEM. However, it is still unclear whether or not it is closer to experimental data due to a lack of experimental analysis. This can be done in further research, along with assigning a bcc phase to the oligocrystal in place of

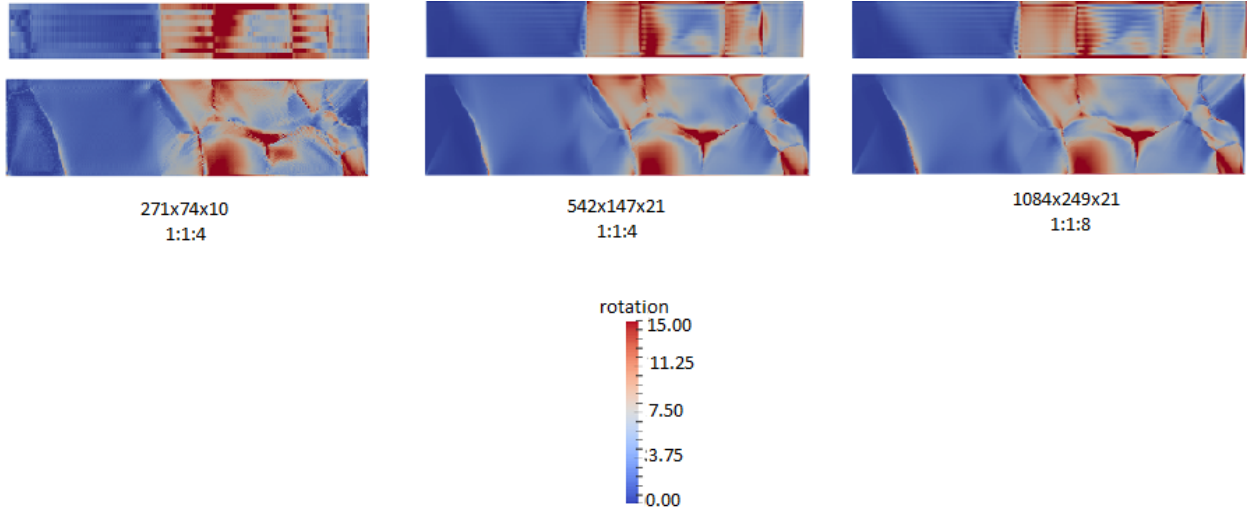


Figure 8.13: The grain rotation spatial maps for different resolutions. the calculations are done by spectral method. There seems to be no effective change except smoothing upon increasing resolution.

fcc, to draw direct comparisons with work done by Lim et al^[1] at SNL.

To conclude, although it is evident that the Spectral solution estimates higher strains near the grain boundaries as compared to the CPFEM, it is not evident which of these is closer to the experimental data. Further research pertaining to direct comparisons to experimental data is warranted. Also, equiaxed voxels are desirable in case of spectral solution whereas the FEM does not have an issue with the aspect ratio of the voxels. It is also clear that even though the overall strain is constant, the main difference between spectral methods and CPFEM lies in the distribution of the strains. In case of CPFEM, lower strains at grain boundaries and higher strains at the bulk is observed whereas for a spectral solution, there is a higher strain estimation near grain boundaries, but lower strains are calculated in the bulk of the grain.

Ratios of grain rotations at different resolutions to those calculated at $271 \times 74 \times 10$ mesh

resolution

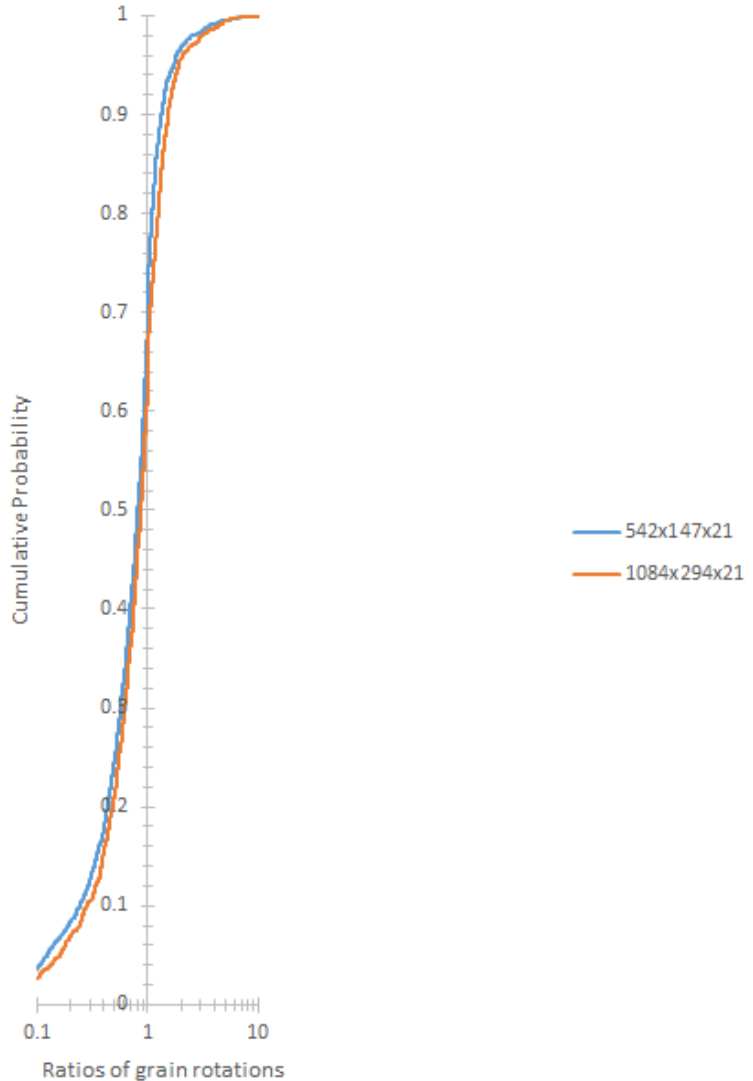


Figure 8.14: Quantitative comparisons of grain rotations at different resolutions. The range of the ratios is from 0.1 to 5.0 which indicates similarity between the spatial maps showing grain rotations.

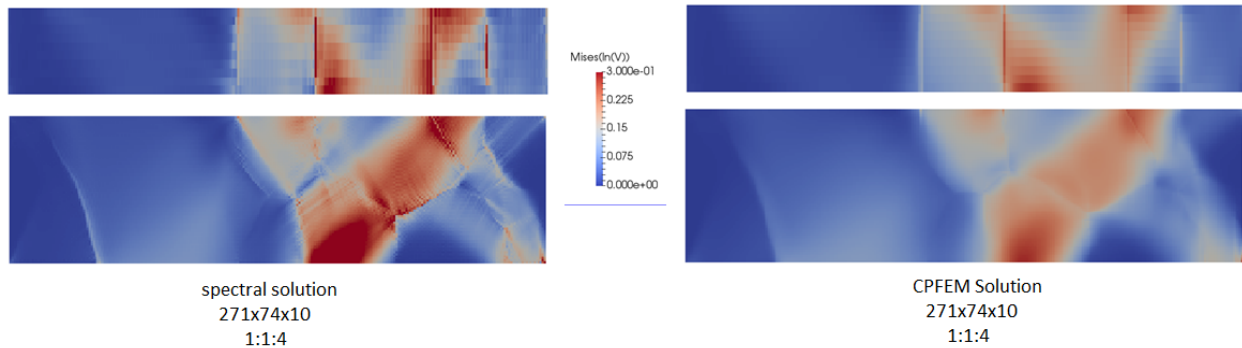


Figure 8.15: Spatial maps for strains calculated by CPFEM and spectral solution. They look similar except for the regions near the grain boundaries

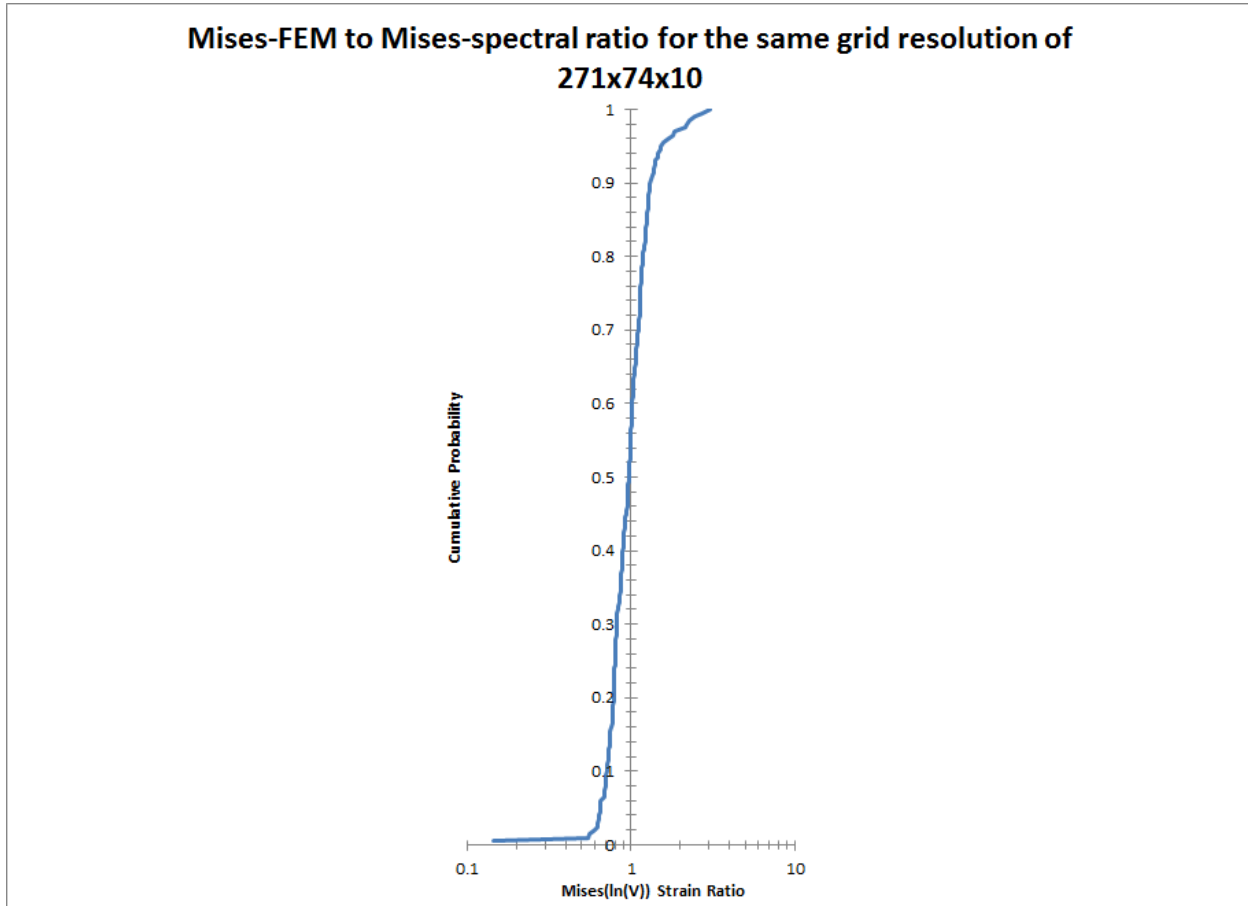


Figure 8.16: Quantitative comparisons of strains calculated by FEM and spectral method. The range of the ratios of strains calculated by FEM to those by spectral method is from 0.1 to 5.0 which indicates similarity between the spatial maps showing the strains.

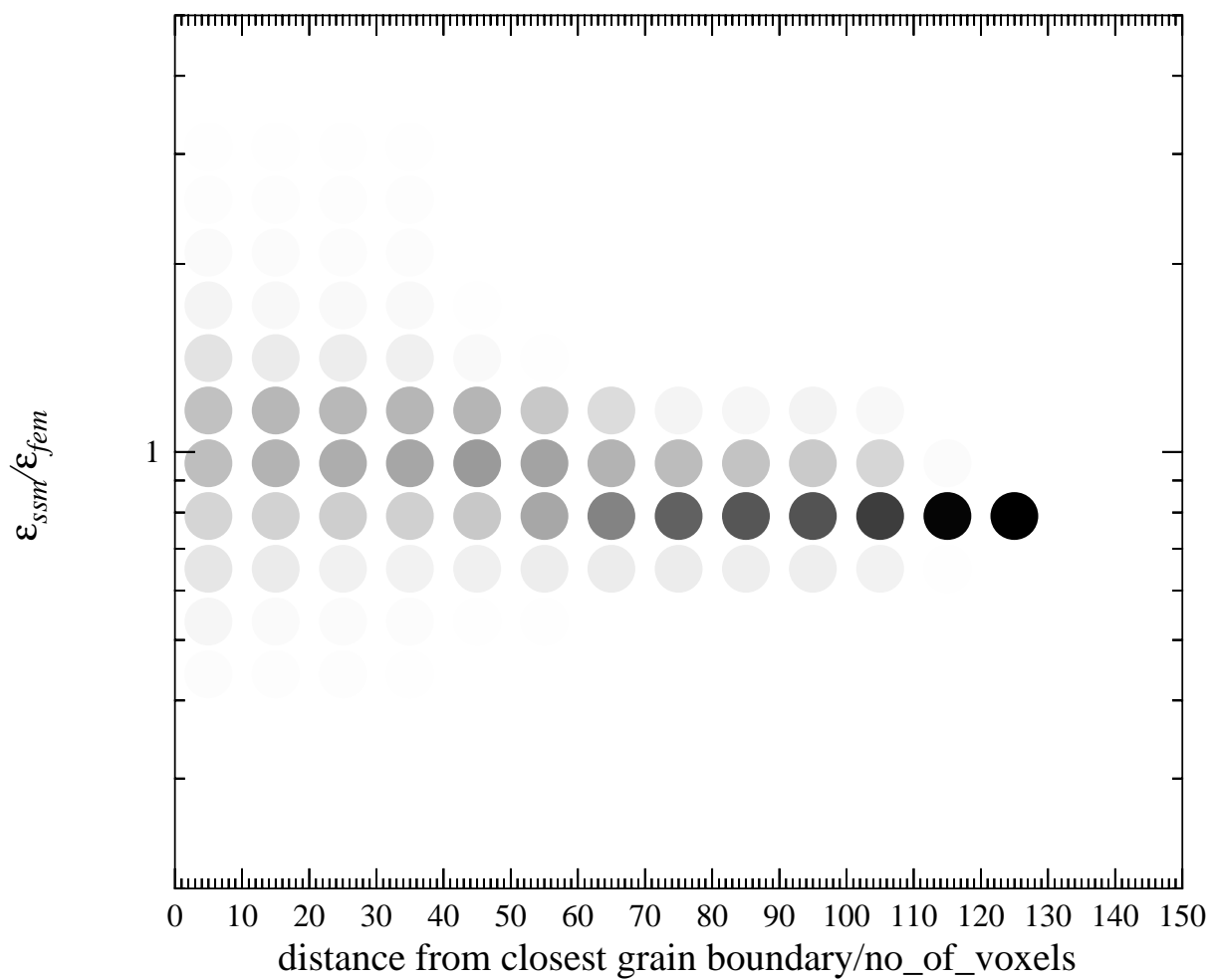


Figure 8.17: Distance from closest grain boundary versus ratio of spectral solution method strains to fem strains.

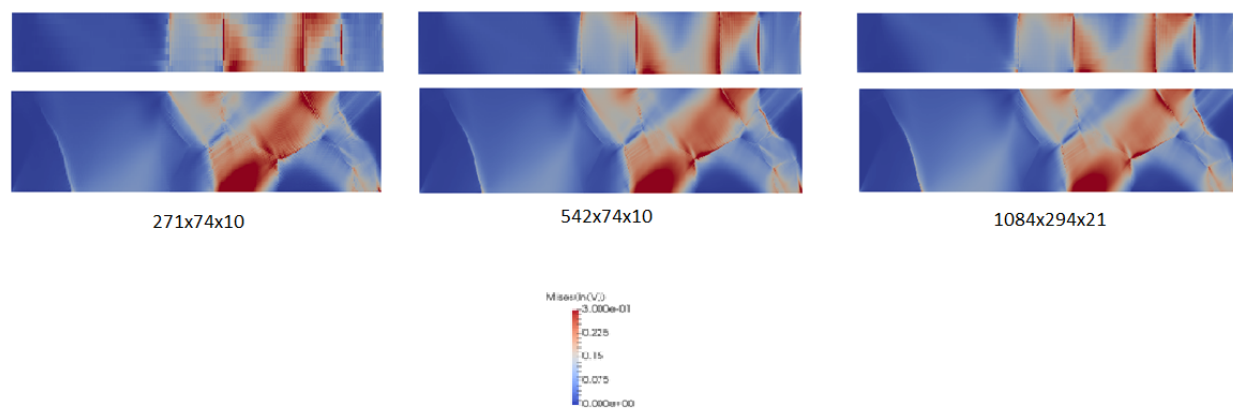


Figure 8.18: Spatial maps of spectrally calculated strains at various resolutions.

Ratio of Mises strains at varying resolutions to those calculated at 271x74x10 mesh resolution

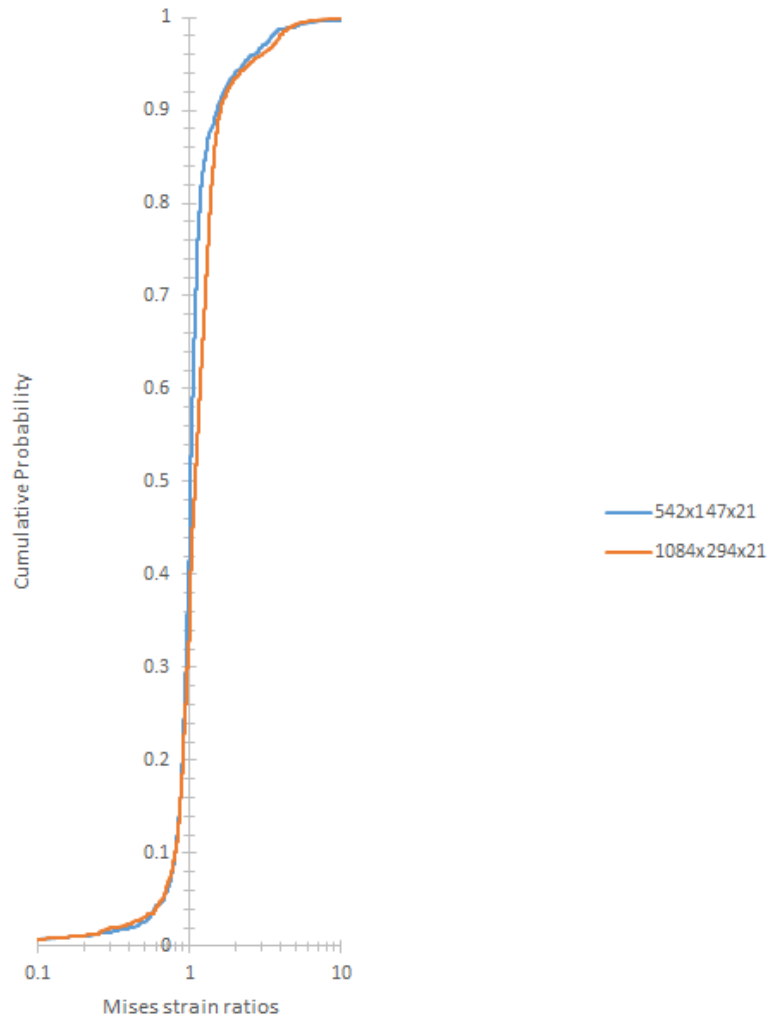


Figure 8.19: Quantitative comparison of strains calculated at various resolutions by the spectral method.

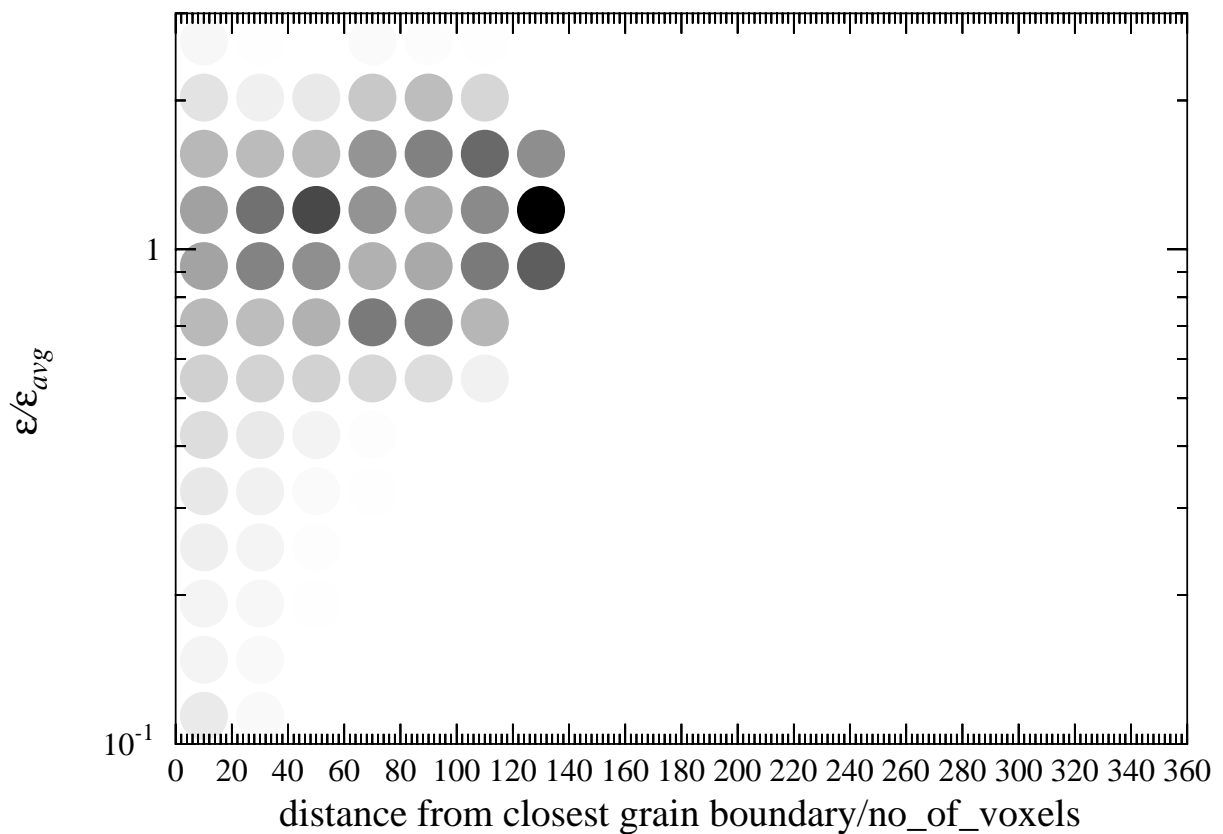


Figure 8.20: Distance from closest grain boundary versus normalized strains calculated spectrally for 271x74x10 resolution.

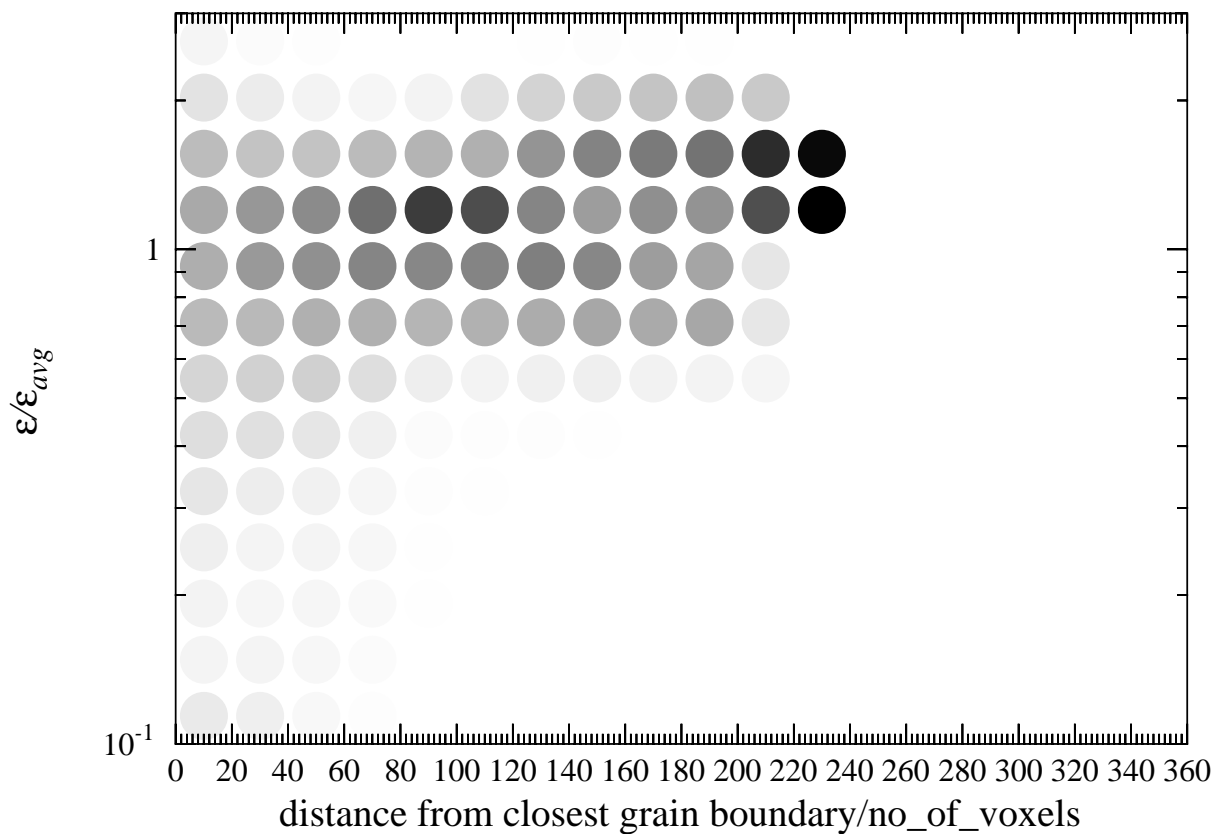


Figure 8.21: Distance from closest grain boundary versus normalized strains calculated spectrally for 542x147x21 resolution.

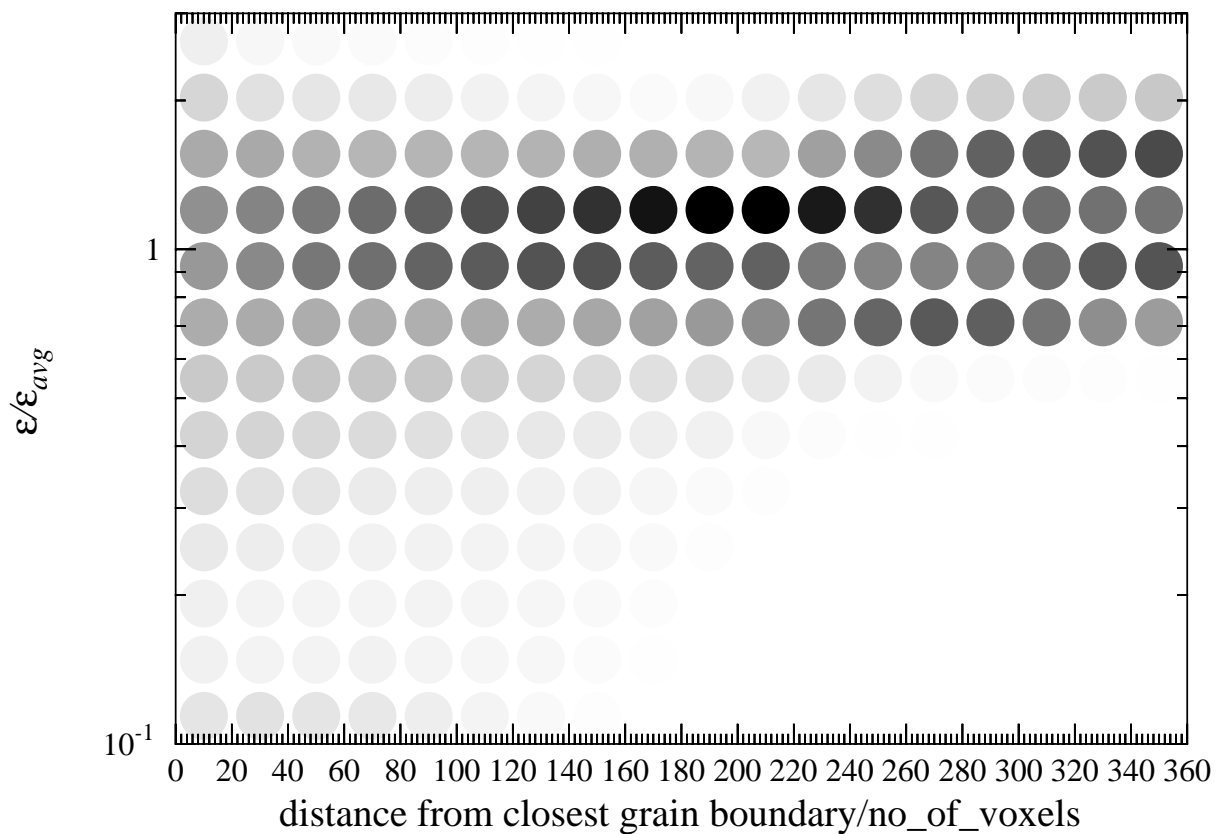


Figure 8.22: Distance from closest grain boundary versus normalized strains calculated spectrally for 1084x294x21 resolution.

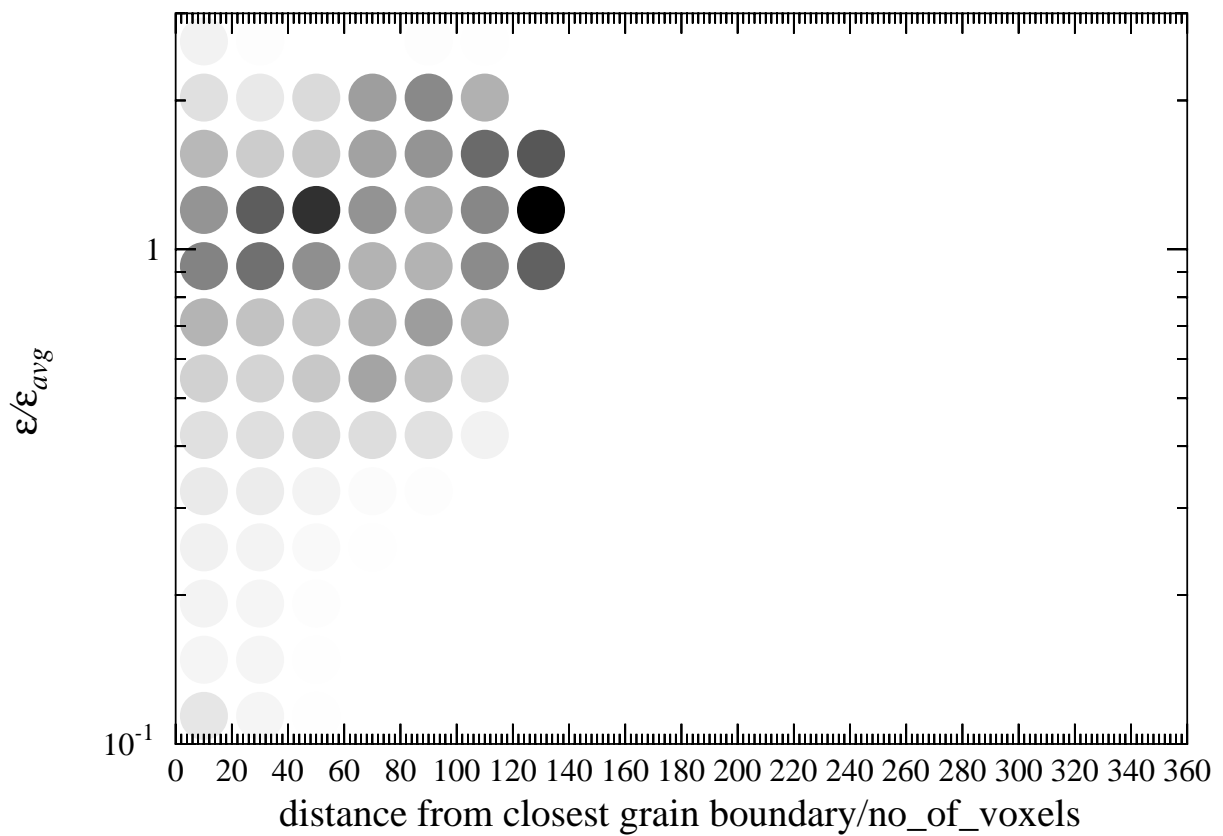


Figure 8.23: Distance from closest grain boundary versus normalized strains calculated by FEM at 271x74x10 resolution.

APPENDICES

APPENDIX A

AUTOMATOR CODE

```
#!/bin/bash

SOURCE="${BASH_SOURCE[0]}"

while [ -h "$SOURCE" ]; do
    DIR=$( cd -P "$( dirname "$SOURCE" )" && pwd )"
    SOURCE=$(readlink "$SOURCE")
    [[ $SOURCE != /* ]] && SOURCE="$DIR/$SOURCE"
done

DIR=$( cd -P "$( dirname "$SOURCE" )" && pwd )"
echo $DIR

theFile=$DIR/.. data/Oligo1_EBSD_Initial_xyG.csv
originalData=${theFile%.*}.txt
tr ',' '\t' < $theFile > $originalData
reLabel -l X,Y,G11,G12,G13,G21,G22,G23,G31,G32,G33 \
-s 1_pos,2_pos,1_a,2_a,3_a,1_b,2_b,3_b,1_c,2_c,3_c \
<$originalData > working_originalData.txt
newFile=$DIR/.. data/5_degrees/working_originalData

>geom_fromTable - coordinates pos -t 5 - degrees - phase \
>Phase -a a -b b -c c ${newFile}.txt
```

```

Nmicro='grep "microstructures" \
${newFile}.geom | awk '{print $2}''`  

showTable -nolabels -info ${newFile}.geom | tail \
-n $((2+6*$Nmicro)) > material.config

$DIR/./code/eulers_fromGeomheader.sh \
${newFile}.geom grainOrientations.txt  

mv ${newFile}.geom 1084x294.geom

geom_rescale -g 0.5x 0.5x 1.0x <1084x294.geom >542x147.geom  

geom_rescale -g 0.5x 0.5x 1.0x <542x147.geom > 271x74.geom  

geom_rescale -g 1084 294 168 -s 1.0x 1.0x 168x \
<1084x294.geom >1084x294x168.geom  

geom_rescale -g 1.0x 1.0x 0.125x -s 1.0x 1.0x 1.0x \
<1084x294x168.geom >1084x294x21.geom  

geom_rescale -g 542 147 21 -s 1.0x 1.0x 168x \
<542x147.geom > 542x147x21.geom  

geom_rescale -g 271 74 10 -s 1.0x 1.0x 168x \
<271x74.geom >271x74x10.geom

geom_toTable -p pos <1084x294x168.geom >1084x294x168.txt  

geom_toTable -p pos <1084x294x21.geom >1084x294x21.txt  

geom_toTable -p pos <542x147x21.geom >542x147x21.txt  

geom_toTable -p pos <271x74x10.geom >271x74x10.txt

addIPFcolor -eulers euler -degrees \

```

```

- pole 1.0 0.0 0.0 grainOrientations.txt
addIPFcolor - eulers euler - degrees \
- pole 0.0 1.0 0.0 grainOrientations.txt
addIPFcolor - eulers euler - degrees \
- pole 0.0 0.0 1.0 grainOrientations.txt

addMapped - map microstructure - label \
IPF_100_cubic - asciitable grainOrientations.txt \
271x74x10.txt 542x147x21.txt 1084x294x21.txt 1084x294x168.txt
addMapped - map microstructure - label \
IPF_010_cubic - asciitable grainOrientations.txt \
271x74x10.txt 542x147x21.txt 1084x294x21.txt 1084x294x168.txt
addMapped - map microstructure - label \
IPF_001_cubic - asciitable grainOrientations.txt \
271 x74x10 .txt 542 x147x21 .txt 1084 x294x21 .txt 1084x294x168 .txt

#addIPFcolor - eulers euler - degrees - pole 1.0 0.0 0.0 \
271 x74x10 .txt 542 x147x21 .txt 1084 x294x21 .txt 1084x294x168 .txt
#addIPFcolor - eulers euler - degrees - pole 0.0 1.0 0.0 \
271 x74x10 .txt 542 x147x21 .txt 1084 x294x21 .txt 1084x294x168 .txt
#addIPFcolor - eulers euler - degrees - pole 0.0 0.0 1.0 \
271 x74x10 .txt 542 x147x21 .txt 1084 x294x21 .txt 1084x294x168 .txt

vtk_rectilinearGrid -m point -p pos \
<1084x294x168 .txt> mesh_1084x294x168 .vtk
vtk_rectilinearGrid -m point -p pos \

```

```

<1084x294x21 .txt> mesh_1084x294x21 .vtk
vtk_rectilinearGrid -m point -p pos \
<542x147x21 .txt > mesh_542x147x21 .vtk
vtk_rectilinearGrid -m point -p pos \
<271 x74x10 .txt> mesh_271x74x10 .vtk

vtk_addRectilineargridData -m point - vtk mesh_1084x294x168 .vtk \
-c IPF_100_cubic <1084x294x168 .txt> mesh_1084x294x168_added100 .vtr
vtk_addRectilineargridData -m point - vtk mesh_1084x294x21 .vtk \
-c IPF_100_cubic <1084x294x21 .txt> mesh_1084x294x21_added100 .vtr
vtk_addRectilineargridData -m point - vtk mesh_542x147x21 .vtk \
-c IPF_100_cubic <542x147x21 .txt> mesh_542x147x21_added100 .vtr
vtk_addRectilineargridData -m point - vtk mesh_271x74x10 .vtk \
-c IPF_100_cubic <271 x74x10 .txt> mesh_271x74x10_added100 .vtr

vtk_addRectilineargridData -m point - vtk mesh_1084x294x168 .vtk \
-c IPF_010_cubic <1084x294x168 .txt> mesh_1084x294x168_added010 .vtr
vtk_addRectilineargridData -m point - vtk mesh_1084x294x21 .vtk \
-c IPF_010_cubic <1084x294x21 .txt> mesh_1084x294x21_added010 .vtr
vtk_addRectilineargridData -m point - vtk mesh_542x147x21 .vtk \
-c IPF_010_cubic <542x147x21 .txt> mesh_542x147x21_added010 .vtr
vtk_addRectilineargridData -m point - vtk mesh_271x74x10 .vtk \
-c IPF_010_cubic <271 x74x10 .txt> mesh_271x74x10_added010 .vtr

vtk_addRectilineargridData -m point - vtk mesh_1084x294x168 .vtk \
-c IPF_001_cubic <1084x294x168 .txt> mesh_1084x294x168_added001 .vtr

```

```

vtk_addRectilineargridData -m point - vtk mesh_1084x294x21.vtk \
-c IPF_001_cubic <1084x294x21.txt>mesh_1084x294x21_added001.vtr
vtk_addRectilineargridData -m point - vtk mesh_542x147x21.vtk \
-c IPF_001_cubic <542x147x21.txt>mesh_542x147x21_added001.vtr
vtk_addRectilineargridData -m point - vtk mesh_271x74x10.vtk \
-c IPF_001_cubic <271x74x10.txt>mesh_271x74x10_added001.vtr

geom_translate -m 2 \
<1084x294x168.geom>1084x294x168_translated.geom
geom_translate -m 2 \
<1084x294x21.geom>1084x294x21_translated.geom
geom_translate -m 2 \
<542x147x21.geom>542x147x21_translated.geom
geom_translate -m 2 \
<271x74x10.geom>271x74x10_translated.geom

geom_canvas -g 1084 324 186 -o 0 -15 -9 - fill 2 \
<1084x294x168_translated.geom>1084x294x168_air.geom
geom_canvas -g 1194 324 186 -o -55 0 0 - fill 1 \
<1084x294x168_air.geom>1084x294x186_air_supported.geom

geom_canvas -g 1084 324 23 -o 0 -15 -1 - fill 2 \
<1084x294x21_translated.geom>1084x294x21_air.geom
geom_canvas -g 1194 324 23 -o -55 0 0 - fill 1 \
<1084x294x21_air.geom>1084x294x21_air_supported.geom

```

```
geom_canvas -g 542 163 23 -o 0 -8 -1 - fill 2 \
<542x147x21_translated.geom > 542x147x21_air.geom

geom_canvas -g 596 163 23 -o -27 0 0 - fill 1 \
<542x147x21_air.geom > 542x147x21_air_supported.geom

geom_canvas -g 271 82 12 -o 0 -4 -1 - fill 2 \
<271x74x10_translated.geom > 271x74x10_air.geom

geom_canvas -g 299 82 12 -o -14 0 0 - fill 1 \
<271x74x10_air.geom > 271x74x10_air_supported.geom

geom_check 1084x294x168_air.geom 1084x294x168_air_supported.geom
geom_check 1084x294x21_air.geom 1084x294x21_air_supported.geom
geom_check 542x147x21_air.geom 542x147x21_air_supported.geom
geom_check 271x74x10_air.geom 271x74x10_air_supported.geom
```

APPENDIX B
MATERIAL CONFIGURATION FILE

<homogenization>

[SX]

type none

<crystallite>

[essential]

(output) orientation
(output) grainrotation
(output) f
(output) fe
(output) p

<phase>

\$Id: Phase_Phenopowerlaw_Aluminum.config \\\n3063 2014-04-02 10:59:14Z MPIE\m.diehl \$ ###\n[Aluminum]

elasticity	hooke
plasticity	phenopowerlaw
(output)	resistance_slip
(output)	shearrate_slip
(output)	resolvedstress_slip
(output)	accumulatedshear_slip
(output)	totalshear
lattice_structure	fcc
Nslip	12 # per family
Ntwin	0 # per family
c11	106.75e9
c12	60.41e9
c44	28.34e9
gdot0_slip	0.001
n_slip	20
tau0_slip	31e6 # per family
tausat_slip	63e6 # per family
a_slip	2.25
gdot0_twin	0.001
n_twin	20
tau0_twin	31e6 # per family
s_pr	0

twin_b	0
twin_c	0
twin_d	0
twin_e	0
h0_slipslip	75e6
h0_sliptwin	0
h0_twinslip	0
h0_twintwin	0
interaction_slipslip	1 1 1.4 1.4 1.4 1.4
interaction_sliptwin	1 1 1 1 1 1 1 1 1 1 1 1 1 1 1 1
interaction_twinslip	1 1 1 1 1 1 1 1 1 1 1 1 1 1 1 1
interaction_twintwin	1 1 1 1 1 1 1 1 1 1 1 1 1 1 1 1
atol_resistance	1

[rigid]

elasticity hooke

plasticity none

lattice_structure isotropic

c11 110.9e10

c12 58.34e10

[air]

elasticity hooke

plasticity isotropic

/dilatation/

```

lattice_structure isotropic
c11           110.9e6
c12           0.0
taylorfactor 3
tau0  0.333e6
gdot0 0.001
n 20
h0 1e6
tausat 0.667e6
w0 2.25
atol_resistance 1

<microstructure>
[baseplate]
crystallite 1
( constituent ) phase 2 texture 1 fraction 1.0
[airlayer]
crystallite 1
( constituent ) phase 3 texture 1 fraction 1.0
[Grain01]
crystallite 1
( constituent ) phase 1 texture 1      fraction 1.0
[Grain02]
crystallite 1
( constituent ) phase 1 texture 2      fraction 1.0

```

```
[ Grain03 ]
crystallite 1
( constituent ) phase 1 texture 3      fraction 1.0
[ Grain04 ]
crystallite 1
( constituent ) phase 1 texture 4      fraction 1.0
[ Grain05 ]
crystallite 1
( constituent ) phase 1 texture 5      fraction 1.0
[ Grain06 ]
crystallite 1
( constituent ) phase 1 texture 6      fraction 1.0
[ Grain07 ]
crystallite 1
( constituent ) phase 1 texture 7      fraction 1.0
[ Grain08 ]
crystallite 1
( constituent ) phase 1 texture 8      fraction 1.0
[ Grain09 ]
crystallite 1
( constituent ) phase 1 texture 9      fraction 1.0
[ Grain10 ]
crystallite 1
( constituent ) phase 1 texture 10     fraction 1.0
[ Grain11 ]
crystallite 1
```

```
(constituent)    phase 1 texture 11      fraction 1.0
[ Grain12 ]
crystallite 1
(constituent)    phase 1 texture 12      fraction 1.0
[ Grain13 ]
crystallite 1
(constituent)    phase 1 texture 13      fraction 1.0
[ Grain14 ]
crystallite 1
(constituent)    phase 1 texture 14      fraction 1.0
[ Grain15 ]
crystallite 1
(constituent)    phase 1 texture 15      fraction 1.0
[ Grain16 ]
crystallite 1
(constituent)    phase 1 texture 16      fraction 1.0
[ Grain17 ]
crystallite 1
(constituent)    phase 1 texture 17      fraction 1.0
[ Grain18 ]
crystallite 1
(constituent)    phase 1 texture 18      fraction 1.0
<texture>
[ Grain01 ]

(gauss) phil 93.2191      Phi 44.9554      phi2 43.3056\
```

```
scatter 0.0      fraction 1.0
```

```
[ Grain02 ]
```

```
(gauss) phil -74.389      Phi 28.602      phi2 44.2014\
```

```
scatter 0.0      fraction 1.0
```

```
[ Grain03 ]
```

```
(gauss) phil -87.5264     Phi 25.9108     phi2 47.6273\
```

```
scatter 0.0      fraction 1.0
```

```
[ Grain04 ]
```

```
(gauss) phil -65.882      Phi 40.6057     phi2 47.5068\
```

```
scatter 0.0      fraction 1.0
```

```
[ Grain05 ]
```

```
(gauss) phil -106.452     Phi 35.1883     phi2 48.8901\
```

```
scatter 0.0      fraction 1.0
```

```
[ Grain06 ]
```

```
(gauss) phil 108.138      Phi 44.982      phi2 44.1021\
```

```
scatter 0.0      fraction 1.0
```

```
[ Grain07 ]
```

```
(gauss) phil -61.7808     Phi 29.7165     phi2 30.0215\
```

```
scatter 0.0      fraction 1.0
```

```
[ Grain08 ]
```

```
(gauss) phil 125.367      Phi 48.5804      phi2 37.1688\
scatter 0.0      fraction 1.0

[ Grain09 ]

(gauss) phil 50.9184      Phi 43.8141      phi2 47.3997\
scatter 0.0      fraction 1.0

[ Grain10 ]

(gauss) phil 45.0427      Phi 47.8092      phi2 48.6582\
scatter 0.0      fraction 1.0

[ Grain11 ]

(gauss) phil 88.9443      Phi 44.4786      phi2 42.6434\
scatter 0.0      fraction 1.0

[ Grain12 ]

(gauss) phil -17.1677     Phi 51.8046      phi2 43.726\
scatter 0.0      fraction 1.0

[ Grain13 ]

(gauss) phil 105.945      Phi 50.722      phi2 55.3715\
scatter 0.0      fraction 1.0

[ Grain14 ]

(gauss) phil -43.5652     Phi 51.5874      phi2 39.964\
```

scatter 0.0 fraction 1.0

[Grain15]

(gauss) phil 113.782 Phi 52.8362 phi2 44.1117 \

scatter 0.0 fraction 1.0

[Grain16]

(gauss) phil -62.2733 Phi 45.8902 phi2 43.0571 \

scatter 0.0 fraction 1.0

[Grain17]

(gauss) phil -82.2969 Phi 47.3403 phi2 47.1105 \

scatter 0.0 fraction 1.0

[Grain18]

(gauss) phil -48.625 Phi 51.2483 phi2 39.8353 \

scatter 0.0 fraction 1.0

APPENDIX C
NUMERICS CONFIGURATIONFILE

```
### $Id$ ###

### numerical parameters ###

relevantStrain           1.0e-7
defgradTolerance          1.0e-7
iJacoStiffness            1
iJacoLpresiduum           1
pert_Fg                   1.0e-7
pert_method                1
integrator                1
integratorStiffness        1
analyticJaco               1
unitlength                 1
usepingpong                1

## crystallite numerical parameters ##

nCryst                      20
subStepMinCryst              1.0e-3
subStepSizeCryst             0.25
stepIncreaseCryst            1.5
nState                       10
nStress                      40
rTol_crystalliteState       1.0e-6
```

```

rTol_crystalliteStress      1.0e-6
aTol_crystalliteStress      1.0e-8
rTol_crystalliteTemperature 1.0e-6

## homogenization numerical parameters ##
nHomog                      20
subStepMinHomog               1.0e-3
subStepSizeHomog                0.25
stepIncreaseHomog                 1.5
nMPstate                      10

## RGC scheme numerical parameters ##
aTol_RGC                      1.0e+4
rTol_RGC                      1.0e-3
aMax_RGC                       1.0e+10
rMax_RGC                       1.0e+2
perturbPenalty_RGC              1.0e-7
maxRelaxation_RGC                1.0e+0

relevantMismatch_RGC            1.0e-5

viscosityPower_RGC              1.0e+0
viscosityModulus_RGC             0.0e+0

refRelaxationRate_RGC           1.0e-3

```

```

maxVolDiscrepancy_RGC      1.0e-5
volDiscrepancyMod_RGC      1.0e+12
discrepancyPower_RGC       5.0

fixed_seed                  0

## spectral parameters ##
err_div_tolAbs              1.0e-3
err_div_tolRel              5.0e-4
err_curl_tolAbs             1.0e-12
err_curl_tolRel             5.0e-4
err_stress_tolAbs           1.0e3
err_stress_tolRel           0.01
fftw_timelimit              -1.0

rotation_tol                 1.0e-12
fftw_plan_mode               FFTW_PATIENT
itmax                         250
itmin                         2
maxCutBack                    3
memory_efficient              1
update_gamma                  0
divergence_correction          2
spectralsolver                basicPETSc
spectralfilter                 none
petsc_options                  -snes_type ngmres

```

-s n e s _ n g m r e s _ a n d e r s o n

regrid Mode	0
p o l a r A l p h a	1 . 0
p o l a r B e t a	1 . 0

APPENDIX D
ALTERATIONS TO NUMERICS CONNFIGURATION FILE

err_div_tolRel 5.0e-3
spectralsolver polarisation

APPENDIX E

LOADCASE FILE

```
F 1.07 0.0 0.0  0.0 0.0 0.0  0.0 0.0 0.0  
t 700 incs 70 restart 10 freq 10
```

F is the deformation gradient tensor.

APPENDIX F
QUEUE SUBMISSION FILE

#!/bin/bash -login

#PBS -l walltime=24:00:00

I estimated 1-days walltime

#PBS -l feature=intel14

#PBS -l nodes=1:ppn=4

#PBS -l mem=5gb

#PBS -N Siddharth_MSE_CMM_75x21x16

```
module load Intel/13.0.1.117\  
MKL/11.1 powertools/1.2\  
CMake/3.1.0 Abaqus/6.11 -2
```

```
export DAMASK_NUM_THREADS=4
```

```
cd /mnt/research/CMM/Projects/Siddharth/  
cd testing/data/5_degrees
```

```
DAMASK_spectral -load tension.load \  
-geom 75x21x16.geom > 75x21x16.out
```

APPENDIX G

POST PROCESSING

To get the ASCII table with output from the .spectralOut file:

```
> postResults -range 0 70 70 -split \
- separation x,y,z -cr fe,f,p,orientation, \
grainrotation -increments \
74x20x10_tension.spectralOut
```

This gives us the results in an easily manipulated ASCII table. The next steps (generic) are outlined below:

```
> addCauchy -f f -p p ASCIIfilename.txt
> addStrainTensors -left -logarithmic -f f \
ASCIIfilename.txt
> addMises -e 'ln(V)' -s Cauchy \
ASCIIfilename.txt
> addCalculation -l rotationAngle -f \
'damask.Quaternion(# grainrotation #).asAngleAxis(degrees=True)[0]' \
ASCIIfilename.txt
> geom_check <correspondingGeometryfile.geom>vtrfile.vtr
> vtk_addRectilinearGridData -vtk vtrfile.vtr -inplace \
-mode cell -s 'rotationAngle','Mises(ln(V))' ASCIIfilename.txt
```

This step gives us a .vtr file that can be rendered in Paraview to view the strain maps and grain rotations

```
geom_unpack -onedimensional \
<correspondingGeometryfile.geom>ID.txt
```

This step gives the geometry file, which is a two dimensional array, in the form of a one dimensional listing of material point texture IDs. We then assign a label to the single column data, let's say 'ID'.

```
> add Table -t a b l e ID . t x t ASCIIfilename . t x t  
> filterTable -c '#ID#>2' -w 'ipinitialcoord',\  
'ID', 'Mises (ln(V))' ID . t x t \  
| addCalculation -l texture -f '#ID#-2' |\  
reLabel -l 'ipinitialcoord' -s pos  
> addEuclideanDistance -t boundary -p pos -i texture ID . t x t  
#adds grain boundary distance
```

the Mises' strains are then normalized by dividing the strains at each material point by the average strain of the grain it belongs to. The normalized strains and the Euclidean distances are then sent into binXY which gives each material point a probability density, and thereafter it is rendered as a nice plot by gri.

APPENDIX H

EULER ANGLES FROM GEOMETRY FILE HEADER

```
#!/usr/bin/env python

import sys
import re

try:
    infilename = sys.argv[1]; outfilename = sys.argv[2]
except:
    print "Usage:", sys.argv[0], "infile outfile"; sys.exit(1)

output = []

with open(infilename, 'r') as infile:
    i = 0
    for line in infile:
        regexp = re.compile('^(gauss )\s+phi1\s+([+-]0123456789]+)\s+Phi\s+([+-]0123456789]+\s+phi2\s+([+-]0123456789]+)')

        m = regexp.match(line)
        if m:
            i += 1
            output.append(''.join([str(i),m.group(1),m.group(2),m.group(3)]))
```

```
with open( outfile , 'w' ) as outfile:  
    outfile . write( '\n' . join([ '1 head' ,  
        'id 1_euler 2_euler 3_euler' ]+output)+ '\n' )
```

BIBLIOGRAPHY

BIBLIOGRAPHY

- Lim, H., Carroll, J. D., Battaile, C. C., Buchheit, T. E., Boyce, B. L., & Weinberger, C. R. (2014). Grain-scale experimental validation of crystal plasticity finite element simulations of tantalum oligocrystals. *International Journal of Plasticity*, 60, 1-18.
- Bahl, S., Suwas, S., & Chatterjee, K. (2014). The importance of crystallographic texture in the use of titanium as an orthopedic biomaterial. *RSC Advances*, 4(72), 38078-38087.
- Hodge, P., and Prager, W. (1948). A Variational Principle for Plastic Materials with Strain Hardening. *Journal of Mathematics and Physics*, 27(1), 1-10.
- Basinski, Z. S. (1959). Thermally activated glide in face-centred cubic metals and its application to the theory of strain hardening. *Philosophical Magazine*, 4(40), 393-432.
- Lebensohn, R. A. (2001). N-site modeling of a 3D viscoplastic polycrystal using fast Fourier transform. *Acta Materialia*, 49(14), 2723-2737.
- Mika, D. P., and Dawson, P. R. (1999). Polycrystal plasticity modeling of intracrystalline boundary textures. *Acta Materialia*, 47(4), 1355-1369.
- Barbe, F., Decker, L., Jeulin, D., & Cailletaud, G. (2001). Intergranular and intragranular behavior of polycrystalline aggregates. Part 1: FE model. *International journal of plasticity*, 17(4), 513-536.
- Clayton, J. D., & McDowell, D. L. (2003). A multiscale multiplicative decomposition for elasto-plasticity of polycrystals. *International Journal of Plasticity*, 19(9), 1401-1444.
- Michel, J.C., Moulinec, H., & Suquet, P. (2001). A computational scheme for linear and non linear composites with arbitrary phase contrast. *International Journal for Numerical Methods in Engineering*, 52(1-2), 139-160
- Suquet, P., Moulinec, H., Castelnau, O., Montagnat, M., Lahellec, N., Grennerat, F., ... & Brenner, R. (2012). Multi-scale modeling of the mechanical behavior of polycrystalline ice under transient creep. *Procedia IUTAM*, 3, 76-90.
- Prakash, A., & Lebensohn, R. A. (2009). Simulation of micro-mechanical behavior of polycrystals: finite elements versus fast Fourier transforms. *Modeling and Simulation in Materials Science and Engineering*, 17(6), 064010.
- Liu, B., Raabe, D., Roters, F., Eisenlohr, P., & Lebensohn, R. A. (2010). Comparison of finite element and fast Fourier transform crystal plasticity solvers for texture prediction. *Modelling and*

Simulation in Materials Science and Engineering, 18(8), 085005.

Fortin, M., & Glowinski, R. (2000). Augmented Lagrangian methods: applications to the numerical solution of boundary-value problems. Elsevier.

Eisenlohr, P., Diehl, M., Lebensohn, R. A., & Roters, F. (2013). A spectral method solution to crystal elasto-viscoplasticity at finite strains. International Journal of Plasticity, 46, 37-53.

Moulinec, H., and Silva, F. (2014). Comparison of three accelerated FFT based schemes for computing the mechanical response of composite materials. International Journal for Numerical Methods in Engineering, 97(13), 960-985.

Balay, S., Abhyankar, S., Adams, M., Brown, J., Brune, P., Buschelman, K., ... & McInnes, L. C. (2014). Petsc users manual revision 3.5. Technical report, Argonne National Laboratory (ANL).

Oosterlee, C. W., & Washio, T. (2000). Krylov subspace acceleration of nonlinear multigrid with application to recirculating flows. SIAM Journal on Scientific Computing, 21(5), 1670-1690.

Shanbhag, P., Eisenlohr, P., Diehl, M., & Roters, F. (2015). Numerically robust spectral methods for crystal plasticity simulations of heterogeneous materials. International Journal of Plasticity, 66, 31-45.

Roters, F., Eisenlohr, P., Kords, C., Tjahjanto, D. D., Diehl, M., & Raabe, D. (2012). DAMASK: the Düsseldorf Advanced MAterial Simulation Kit for studying crystal plasticity using an FE based or a spectral numerical solver. Procedia IUTAM, 3, 3-10.